IMPROVED INVERSE MODELING OF NITROGEN OXIDES EMISSIONS USING SATELLITE MEASUREMENTS OVER CHINA AND EVIDENCE OF VOLATILE ORGANICS EMISSIONS OVER THE TROPICAL PACIFIC

A Dissertation
Presented to
The Academic Faculty

by

Dasa Gu

In Partial Fulfillment
of the Requirements for the Degree
Doctor of Philosophy in the
School of Earth and Atmospheric Sciences

Georgia Institute of Technology
May 2014

IMPROVED INVERSE MODELING OF NITROGEN OXIDES EMISSIONS USING SATELLITE MEASUREMENTS OVER CHINA AND EVIDENCE OF VOLATILE ORGANICS EMISSIONS OVER THE TROPICAL PACIFIC

Approved by:

Dr. Yuhang Wang, Advisor
School of Earth and Atmospheric Sciences
Georgia Institute of Technology

Dr. Michael Bergin
School of Earth and Atmospheric Sciences
Georgia Institute of Technology

Dr. Greg Huey
School of Earth and Atmospheric Sciences
Georgia Institute of Technology

Dr. Armistead G. Russell
School of Civil and Environmental Engineering
Georgia Institute of Technology

Dr. Paul Wine
School of Earth and Atmospheric Sciences
Georgia Institute of Technology

Date Approved: March 24, 2014

To Xiaodan

ACKNOWLEDGEMENTS

I deeply appreciate the tremendous supports that I have received from many individuals during the process of obtaining my Ph.D. I thank my advisor, Dr. Yuhang Wang, for his long-term support and guidance with his scientific enthusiasm. I would like to thank my Ph. D. thesis committee members Drs. Michael Bergin, Greg Huey, Ted Russell, and Paul Wine, for their constructive comments and suggestions for my research during all kinds of occasions throughout the years of my Ph.D. study. Their visions and insights not only helped me better address the scientific problems, but also guided me to learn to think more critically and creatively as a scientist. Thanks go to all the current members and alumni of Yuhang Wang's group, especially Charles Smeltzer, Ja-ho Koo, Yuzhong Zhang, Yufei Zou, Ruixiong Zhang, Hang Qu, Drs. Yongjia Song, Tao Zeng, Chun Zhao and Zhen Liu. Above all, I have been supported by the tremendous love of my family: my wife, Xiaodan Du, my parents, my in-laws.

While writing this Acknowledgement, I have thought about the thousands of days I have spent researching, debugging, plotting, writing, and preparing this thesis. I enjoyed every minute and the knowledge gained. The degree earned will be a sufficient reward for the endeavor.

TABLE OF CONTENTS

LIST OF TABLES

LIST OF FIGURES

Page

LIST OF SYMBOLS AND ABBREVIATIONS

Symbols

A	aerosol surface area density
D_{HO_2}	diffusion coefficient of HO_2
E	a posteriori NO_x emission
E_a	a priori NO_x emission
Ej	a posteriori NO_x emission by joint 2 satellites method
k	reaction rate constant
P(OH)	OH production rate
r_p	particle radius
ΔE	change in emission
$\Delta\Omega$	change in column
Ω_m	model simulated NO_2 column
Ω_{GOME-2}	GOME-2 observed NO_2 column
Ω_{m0930}	model simulated NO_2 column at GOME-2 overpass time
Ω_{m1330}	model simulated NO_2 column at OMI overpass time
Ω_{OMI}	OMI observed NO_2 column
Ω_s	satellite observed NO_2 column
α	bulk ratio
α^*	local derivative ratio
β	local emission-to-column sensitivity
γ	reactive uptake coefficient
τ	lifetime
ω	mean molecular speed

Abbreviations

1-D	one-dimensional
3-D	three-dimensional
AMF	air mass factor
AMS	Aerosol Mass Spectrometer
CH_3CH_2OH	ethanol
CH_3OH	methanol
CH_3OOH	methyl hydrogen peroxide
CO	carbon monoxide
DeNOx	denitration
DI	daily inversion method
DRI	daily retrieval-inversion method
GDP	gross domestic product
GOME	Global Ozone Monitoring Experiment
GOME-2	Global Ozone Monitoring Experiment-2
GFED	Global Fire Emissions Database
H_2O_2	hydrogen peroxide
HO_2	hydroperoxyl
HO_x	odd hydrogen
hPa	one hundred Pascal
NEC	Northeast China
KNMI	Royal Netherlands Meteorological Institute
kW	kilowatt
LPG	liquefied petroleum gas
MI	monthly inversion method

NCEP	National Centers for Environmental Prediction
NCP	North China Plain
NEC	Northeast China
NO	nitrogen monoxide
NO_2	nitrogen dioxide
NO_x	nitrogen oxides
O_3	ozone
OH	hydroxyl radical
OMI	Ozone Monitoring Instrument
PASE	Pacific Atmospheric Sulfur Experiment
PEM	Pacific Exploratory Mission
PRD	Pearl River Delta
REAM	Regional chEmical and trAnsport Model
RO_2	organic peroxides
SCD	slant column density
SCIAMACHY	SCanning Imaging Absorption spectroMeter for Atmospheric CHartographY
SCR	Selective Catalytic Reduction
SNCR	Selective Non-Catalytic Reduction
VCD	vertical column density
VOC	volatile organic compound
WRF	Weather Research Forecasting model
YRD	Yangtze River Delta

SUMMARY

Inverse modeling using satellite observations of NO_2 columns has been extensively used to estimate NO_x emissions in China. Two instruments, GOME-2 and OMI, have provided independent global NO_2 column measurements on a nearly daily frequency in recent years. Anthropogenic NO_x emission estimates by applying previously developed monthly inversion or assimilated daily inversion methods to these two sets of measurements show substantial differences. We improved the assimilated daily inversion method by conducting model simulation, satellite retrieval, and inverse modeling sequentially on a daily basis. The improved procedure was applied to GOME-2 and OMI NO_2 measurements over China in 2011, respectively. The new daily retrieval-inversion method significantly reduced the systematic bias in inverse modeling of NO_x emission between using GOME-2 and OMI measurements, and detected more clear seasonal and weekly variations. OMI instrument observed NO_2 columns over China from 2005 to 2010 were analyzed in order to estimate the top-down anthropogenic NO_x emission trends. The estimated average emission trend is 4.01±1.39% yr^{-1}, which is slower than the trend of 5.8-10.8% yr^{-1} reported for previous years. We find large regional, seasonal, and urban-rural variations in emission trends. The average NO_x emission trend of 3.47±1.07% yr^{-1} in warm season (June-September) is less than the trend of 5.03±1.92% yr^{-1} in cool season (October-May). The regional annual emission trends decrease from 4.76±1.61% yr^{-1} in North China Plain to 3.11±0.98% yr^{-1} in Yangtze River Delta and further down to -4.39±1.81% yr^{-1} in Pearl River Delta. The annual emission trends of the four largest megacities, Shanghai, Beijing, Guangzhou and Shenzhen are -0.76±0.29%, 0.69±0.27%,

-4.46±1.22% and -7.18±2.88% yr^{-1}, considerably lower than the regional averages or surrounding rural regions. These results appear to suggest that a number of factors, including emission control measures of thermal power plants, increased hydro-power usage, vehicle emission regulations, and closure or migration of high-emission industries, have significantly reduced or even reversed the increasing trend of NO_x emissions in more economically developed megacities and southern coastal regions, but their effects are not as significant in other major cities or less economically developed regions.

A 1-D chemical transport model was applied to analyze OH and HO_2 radical observations during the Pacific Atmospheric Sulfur Experiment (PASE) near Christmas Island (Kiritimati, 1.52°N 157.24°W) from Aug. 2 through Sep. 10, 2007. Under normal conditions, the production of OH was dominated by the reaction of $O(^1D)$ and H_2O and the cycling from HO_2 into OH was mainly through the reaction of HO_2+O_3. However, in two of fourteen research flights, significantly higher HO_2/OH ratios in the buffer layer than the other flights were found. Model simulations indicated that fast-reacting oxygenated volatile organic compounds, which can react rapidly with OH and provide additional primary radical sources through photolysis, were necessary to explain the observations. During or right before these two flights, the WRF model simulated two strongest shallow convective events during this experiment, suggesting a transport pathway of ocean organics into the buffer layer. Ocean upwelling driven by atmospheric pressure depression during convection may expedite the release of ocean organics. In addition to changing HO_x, the release of organics from the ocean may help explain the underestimation of marine organic aerosols in previous model studies.

CHAPTER 1

INTRODUCTION

1.1 Overview

Nitrogen oxides (NO_x=NO+NO_2) play a key role in the formation of ozone and secondary aerosols. Hydroxyl radical (OH) is the primary oxidant for most traces gases (e.g., CO, volatile organic compounds (VOCs)) in the atmosphere. NO_x are emitted from both anthropogenic sources (e.g., fossil fuel combustion) and natural sources (e.g., lightning, soil, and biomass burning). The large abundance of NO_x over the China has led to elevated secondary photochemical pollutants and caused severely degraded air quality.

1.1.1 Inverse modeling of NO_x emissions over China

The rapid economic growth in China during the last two decades led to a dramatic increase of energy generation and consumption, which significantly increased nitrogen oxides (NO_x=NO+NO_2) emissions and thereby the tropospheric nitrogen dioxide (NO_2) column densities. The traditional bottom-up inventories of NO_x emissions, estimated from limited information of emission source factors and statistical data over China, could have large uncertainties [e.g., *Ohara et al.*, 2007; *Streets et al.*, 2003]. Top-down constraints by satellite column NO_2 observations, such as Global Ozone Monitoring Experiment (GOME), SCanning Imaging Absorption spectroMeter for Atmospheric CHartographY (SCIAMACHY), Ozone Monitoring Instrument (OMI) and Global Ozone Monitoring Experiment-2 (GOME-2), have been applied to reduce uncertainties in emission estimation [e.g., *Choi et al.*, 2012; *Han et al.*, 2009; *He et al.*, 2007;

Kunhikrishnan et al., 2004; *Kurokawa et al.*, 2009; *Lin et al.*, 2012; *Martin et al.*, 2003; *Richter et al.*, 2005; *Shi et al.*, 2008; *Stavrakou et al.*, 2008; *Zhang et al.*, 2012].

Inverse modeling of NO_x emissions, incorporating model simulations and satellite observations, can help to reduce uncertainties in bottom-up inventory especially in China [*Lin et al.*, 2012; *Mijling and van der A*, 2012; *Zhao and Wang*, 2009]. *Martin et al.* [2003] developed the first monthly inversion method by combining the bottom-up emission inventory with top-down constraints from GOME NO_2 column measurements. The method was extended by *Zhao and Wang* [2009] to carry out the emission inversion iteratively on a daily basis to account in part for the nonlinear effects in chemical feedbacks. One issue that has not been discussed extensively is that the inverse modeling results from different satellites can differ significantly, some of which is attributable to a priori profiles used in retrievals [e.g., *Irie et al.*, 2012; *Lin et al.*, 2010; *Vinken et al.*, 2014].

It is important to note that most inverse modeling methods were based on assumption that there is a linear correlation between NO_x emissions and NO_2 columns. However, some studies suggested that NO_x emission is not proportional to the changes in NO_2 columns due to nonlinear chemical feedbacks with OH when they analyzed the emission trends based on the observed column trends [*Gu et al.*, 2013; *Lu and Streets*, 2012; *Stavrakou et al.*, 2008]. Under low emission condition, the increasing of NO_x emission leads to enhancement in OH production through $NO+HO_2$ reaction, and then tends to decrease NO_x lifetime due to higher NO_2 loss through OH. On the other hand, under high emission condition, the increasing of NO_x emission leads to enhancement in OH loss through NO_2+OH, and then tends to increase NO_x lifetime due to the titration of

OH. One potential problem in previous inverse modeling mothods is that nonlinear chemical feedback in NO_x-OH cycling significantly changes NO_x lifetime and it has distinct behaviors at two different satellite overpass times.

Previous studies reported increasing trends varying from 5.8% to 10.8% yr^{-1} for NO_x emissions over China in the past two decades [e.g., *He et al.*, 2007; *Kurokawa et al.*, 2009; *Stavrakou et al.*, 2008]. NO_x emissions in China are mainly driven by power plants and vehicle emissions [e.g., *Shi et al.*, 2008; *Wang et al.*, 2010; *Zhang et al.*, 2007]. Recent studies found that NO_x reduction devices have been widely installed in power plants [*Li et al.*, 2010] and higher emission standards have been used to regulate motor vehicles in China [*Saikawa et al.*, 2011; *Wu et al.*, 2011]. How these control measures affect the NO_x emission trends in China is not yet clear.

1.1.2 HO_x cycling and volatile organics emissions over the tropical Pacific

The cycling of odd hydrogen ($OH+HO_2$, or HO_x) has been extensively studied because of its key role in tropospheric photochemistry and the HO_2/OH ratio was frequently used as indicator of HO_x cycling to evaluate importance of major production and loss processes of OH and HO_2 [e.g., *Brune et al.*, 1998; *Jaegle et al.*, 2001; *Y Kanaya et al.*, 2007; *Lanzendorf et al.*, 2001a; *Lanzendorf et al.*, 2001b; *Ren et al.*, 2008; *Stevens et al.*, 1997]. The Pacific Atmospheric Sulfur Experiment (PASE) provided an observation dataset to investigate the important chemical cycles of HO_x in tropical troposphere, where a large portion of the oxidizing capacity of the atmosphere resides [e.g., Wang and Jacob, 1998]. This intensive field study took place near Christmas Island over the equatorial Pacific Ocean (1ºS - 4ºN and 153º - 159ºW) from August 8 through September 6, 2007. It is a relatively clean environment to evaluate our understanding of

HO_x chemistry [*Conley et al.*, 2009; *Faloona et al.*, 2009; *Gray et al.*, 2010]. The measured HO_2/OH ratios were generally 50~100 pptv/pptv. However, there were two extreme high HO_2/OH ratios up to 450~550 pptv/pptv in buffer layer during two daytime research flights, RF12 and RF14, which suggested unusual physical and chemical process of HO_x cycling over tropical oceans.

The HO_2/OH ratio is controlled by NO_x, CO, VOCs, O_3, halogen oxides and other trace gases [*Brune et al.*, 1998; *Lanzendorf et al.*, 2001a, 2001b; *Ren et al.*, 2008; *Stevens et al.*, 1997]. After quantitative analysis and model simulations, most factors can be excluded except potential oceanic emission of short-lived reactive VOCs. We hypothesize that fast OH-reacting gases likely in form of unknown oceanic volatile organic compounds are injected into the buffer layer by convection leading to the observed high HO_2/OH ratios.

1.2 Description of data

1.2.1 Satellite NO_2 column measurements

Both GOME-2 and OMI instruments are nadir-viewing spectrometers [e.g., *Boersma et al.*, 2004, 2007, 2011]. The OMI instrument was launched onboard the Aura satellite in July 2004, and it has a spatial resolution of 24 × 13 km^2 at nadir [*Levelt et al.*, 2006]. The GOME-2 instrument was launched onboard the MetOp satellite in June 2006 with ground pixel size of 80 × 40 km^2 [*Irie et al.*, 2012]. The local overpass time across the equator is around 9:30 for GOME-2 and around 13:30 for OMI. We excluded the data in all flagged rows with anomalies for the OMI measurements (http://www.knmi.nl/omi/research/product/rowanomaly-background.php). The Royal Netherlands Meteorological Institute (KNMI) OMI (DOMINO2 v2.0) and GOME-2

(TM4NO2A v2.3) tropospheric NO_2 vertical column density (VCD) products are used for monthly inversion and daily inversion methods in our studies. For daily retrieval-inversion method and column trend analysis, we updated a priori profiles in retrievals from Regional chEmical and trAnsport Model (REAM) in place of the default KNMI profiles simulated by the coarser-resolution global chemical transport model TM4 [*Heckel et al.*, 2011]. In addition, we only use measured NO_2 column data when cloud fraction is < 20% for both instruments.

1.2.2 Flight measurements during PASE

Fourteen research flights (RF1 to RF14) were conducted during PASE, and the details of flight patterns were discussed in *Conley et al.* [2009] and *Faloona et al.* [2009]. Two nighttime flights (RF6 and RF13), and a flight to sample clouds (RF4) were not included in this analysis. OH, HO_2, organic peroxides (RO_2), hydrogen peroxide (H_2O_2), and methyl hydrogen peroxide (CH_3OOH) were measured, providing observational constraints on HO_x chemistry over the equatorial Pacific. O_3, CO and water vapor mixing ratios were also measured. Ozone was measured by using a fast chemiluminescence instrument described by *Ridley et al.* [1992]. Aerosol size and distribution were measured by several different instruments as described by *Clarke et al.* [2004]. The chemical composition of aerosols was measured by the Aerodyne Aerosol Mass Spectrometer (AMS) instrument, and the concentration of organic aerosols is recorded during most flights except RF1, RF9, RF10, RF12 and RF13 [*Bandy et al.*, 2011].

1.3 Methodology

1.3.1 3-D and 1-D REAM model

The 3-D REAM has been applied in a number of tropospheric chemistry and transport studies over East Asia, North America and polar regions [e.g. *Choi et al*., 2005, 2008a, 2008b; *Jing et al.*, 2006; *Liu et al.*, 2010, 2012a, 2012b; *Wang et al.*, 2006, 2007; *Yang et al.*, 2011; *Zeng et al.*, 2003, 2006; *Zhao and Wang*, 2009; *Zhao et al.*, 2009a, 2009b, 2010]. The model has a horizontal resolution of 70×70 or 36×36 km^2 with 21 vertical layers in the troposphere. Transport is driven by WRF assimilated meteorological fields constrained by the NCEP reanalysis products (http://www.esrl.noaa.gov/psd/). The chemistry mechanism in REAM is adopted from the GEOS-CHEM model [*Bey et al.*, 2001] with updates of kinetics data (http://jpldataeval.jpl.nasa.gov/). The anthropogenic NO_x and VOCs emissions are from *Zhang et al.* [2009]. The biomass burning emissions are taken from the Global Fire Emissions Database, Version 2 (GFEDv2.1; available at http://daac.ornl.gov/). The lightning NO_x emission is parameterized as by *Zhao et al.* [2010].

The 1-D model was constructed from the 3-D REAM model [*Gray et al., 2010; Liu et al., 2010, 2012b*]. The vertical diffusion coefficient used in the model was constrained by DMS observations [*Gray et al., 2010*]. Other meteorological fields used in the 1-D model were assimilated using the WRF model constrained by the NCEP reanalysis product, while the sub-grid convection transport followed the KF-eta scheme [*Kain*, 2004]. The WRF model has a horizontal resolution of 10 x 10 km^2 with 45 vertical layers below 10 hPa. For each flight, 1-D meteorological parameters along the entire flight track are used. Averages over the sampling region are used for hours outside the flight periods.

1.3.2 Inverse modeling of NO_x emissions

Martin et al. [2003] developed the first monthly inversion method by scaling the bottom-up emission inventory with top-down constraints from GOME NO_2 column measurements. *Zhao and Wang* [2009] improved the method by carrying out the emission inversion iteratively on a daily basis. One issue that has been gradually discussed is that the inverse modeling results from different satellites can differ significantly. Therefore, *Lin et al.* [2010] tried to combine two satellite measurements together with GEOS-Chem model simulation to minimize the systematic bias between inversion emissions from using different instruments. We improve the daily inversion method by conducting model simulation, satellite retrieval, and inverse modeling sequentially on a daily basis. After each inversion, we update anthropogenic NO_x emissions in the model simulation with the newly obtained a posteriori results. Consequently, the inversion optimized emissions are used to compute the a priori NO_2 profiles for satellite retrievals. As such, the a priori profiles used in satellite retrievals are now coupled to inverse modeling results.

1.4 Scope of this work

The objectives of this study are four-fold: (1) to improve inverse modeling of NO_x emission by coupling the a priori profiles used in satellite retrievals with inverse modeling results; (2) to evaluate the uncertainties from photochemical nonlinearity in inverse modeling processes; (3) to estimate regional and seasonal variations in NO_x emission trends over China; (4) to investigate the impacts of potential volatile oceanic organic emissions on HO_x cycling over tropical Pacific. The 3-D and 1-D REAM model simulations are applied to accomplish these objectives along with multiple satellite measurements as well as aircraft measurements.

In this dissertation, each research objective or project is presented as a separate chapter as follows.

Chapter 2 describes study on **Reconciling the Difference of Inverse Modeling Results using GOME-2 and OMI Measurements**. The daily retrieval-inversion method is developed by conducting model simulation, satellite retrieval, and inverse modeling sequentially on a daily basis. The improved method is applied to GOME-2 and OMI NO_2 measurements for estimation of anthropogenic NO_x emissions over China in 2011. The more consistent inversion results are used to investigate seasonal variations of anthropogenic emissions and weekday-to-weekend emission ratios over China.

Chapter 3 works to **Evaluate the Uncertainties from Photochemical Nonlinearity in Inverse Modeling of NO_x Emissions**. A methodology is introduced for estimating the local sensitivity of NO_2 vertical column to NO_x emission while explicitly accounting for the uncertainty in the chemical nonlinearity. The new methodology is applied to GOME-2 and OMI NO_2 measurements for inverse modeling of anthropogenic NO_x emissions over eastern China in August 2007. The inversion results are then compared with emissions from using previously developed monthly inversion method and joint two satellite inversion methods.

Chapter 4 investigates **Reduction in NO_x Emission Trends over China: Regional and Seasonal Variations**. The top-down anthropogenic NO_x emission trends are estimated by analyzing NO_2 columns from the OMI measurements over China from 2005 to 2010. The estimated emission trends are compared with results from previous studies, while regional, seasonal, and urban-rural variations in emission trends are further investigated.

Chapter 5 presents **Evidence of Volatile Organics Emissions over the Tropical Pacific**. A 1-D chemical transport model is applied to analyze OH and HO_2 radical observations during the Pacific Atmospheric Sulfur Experiment near Christmas Island (Kiritimati, 1.52°N 157.24°W) from August 2 through September 10, 2007. In two of fourteen research flights, significantly higher HO_2/OH ratios in the buffer layer than the other flights are found. Model simulations are utilized to examine the hypothesis that fast OH-reacting gases likely in the form of unknown oceanic volatile organic compounds are injected into the buffer layer by convection leading to the observed high HO_2/OH ratios.

And **Chapter 6: Conclusions and Future Research** presents the summary and main findings of this work and recommendations for future research.

CHAPTER 2

[1]RECONCILING THE DIFFERENCE OF INVERSE MODELING OF NITROGEN OXIDES EMISSIONS USING GOME-2 AND OMI MEASUREMENTS

2.1 Introduction

Nitrogen oxides (NO_x=NO+NO_2) play a key role in the formation of ozone and secondary aerosols. NO_x is emitted from both anthropogenic sources (e.g. fossil fuel combustion and human induced biomass burning) and natural sources (e.g. lightning, wildfires, and soil emissions). One region that has witnessed rapid changes in NO_x emissions in the past two decades is China. These changes have been reported previously in analyses of satellite measured tropospheric nitrogen dioxide (NO_2) columns [e.g., *Ghude et al.*, 2009; *Gu et al.*, 2013; *Ma et al.*, 2006; *Richter et al.*, 2004; *Uno et al.*, 2007; *van der A et al.,* 2006].

The traditional bottom-up inventories of NO_x emissions, estimated from limited information of emission source factors and statistical data over China, could have large uncertainties [e.g., *Ohara et al.*, 2007; *Streets et al.*, 2003]. Top-down constraints by satellite column NO_2 observations, such as Global Ozone Monitoring Experiment (GOME), SCanning Imaging Absorption spectroMeter for Atmospheric CHartographY

[1]This chapter is an extension of "Anthropogenic emissions of NO_x over China: Reconciling the difference of inverse modeling results using GOME-2 and OMI measurements" which is under review at Journal of Geophysical Research-Atmospheres. Authors are D. Gu, Y. Wang, C. Smeltzer, and K. F. Boersma.

(SCIAMACHY), Ozone Monitoring Instrument (OMI) and Global Ozone Monitoring Experiment-2 (GOME-2), have been applied to reduce uncertainties in emission estimation [e.g., *Choi et al.*, 2012; *Han et al.*, 2009; *He et al.*, 2007; *Kunhikrishnan et al.*, 2004; *Kurokawa et al.*, 2009; *Lin et al.*, 2012; *Martin et al.*, 2003; *Richter et al.*, 2005; *Shi et al.*, 2008; *Stavrakou et al.*, 2008; *Zhang et al.*, 2012].

Martin et al. [2003] developed the first monthly inversion (MI) method by combining the bottom-up emission inventory with top-down constraints from GOME NO_2 column measurements. The method was extended by *Zhao and Wang* [2009] to carry out the emission inversion iteratively on a daily basis to account in part for the nonlinear effects in chemical feedbacks. One issue that has not been discussed extensively is that the inverse modeling results from different satellites can differ significantly, some of which is attributable to a priori profiles used in retrievals [e.g., *Irie et al.*, 2012; *Lin et al.*, 2010; *Vinken et al.*, 2014]. We choose to use GOME-2 and OMI measurements in this study because these two instruments have similar temporal coverage that is substantially better than SCIAMACHY. Figure 2.1 compares the inverse modeling results of anthropogenic NO_x emissions between using GOME-2 and OMI measurements. Satellite measurements, a priori emissions, and the regional chemical and transport model used in the comparison will be discussed in the next section. By applying the MI method [*Martin et al.*, 2003] with simulations from the Regional chEmical and trAnsport Model (REAM), we find that the relative difference of NO_x inversion emission estimates between using GOME-2 and OMI measurements is 32±12% over China in 2011. The difference is reduced to 16±6% by using the daily inversion (DI) method [*Zhao and Wang*, 2009], but it remains very large.

The substantial difference of inverse modeling results from the two sets of satellite measurements raises an obvious question of consistency in potential science applications of these emission estimates. While not solving the problem, the iteration in the DI method helps reduce the difference compared to MI method. In this study, we examine if the difference can be further reduced by improving the inverse modeling method. We improve the DI method by updating on a daily basis anthropogenic NO_x emissions in REAM using the inversion results and subsequently the a priori NO_x profiles used in the satellite retrieval. The improved daily retrieval-inversion (DRI) method therefore couples the retrieval profiles to inverse modeling results and ensures the consistency between them. The DRI method is implemented into the REAM model to optimize surface anthropogenic NO_x emission estimates with GOME-2 and OMI measurements over China in 2011. The DRI inversion results are compared to those using the DI method to demonstrate the benefits of the new method. We analyze further the seasonal and weekday-to-weekend variations of anthropogenic NO_x emissions over China using the new DRI inversion products.

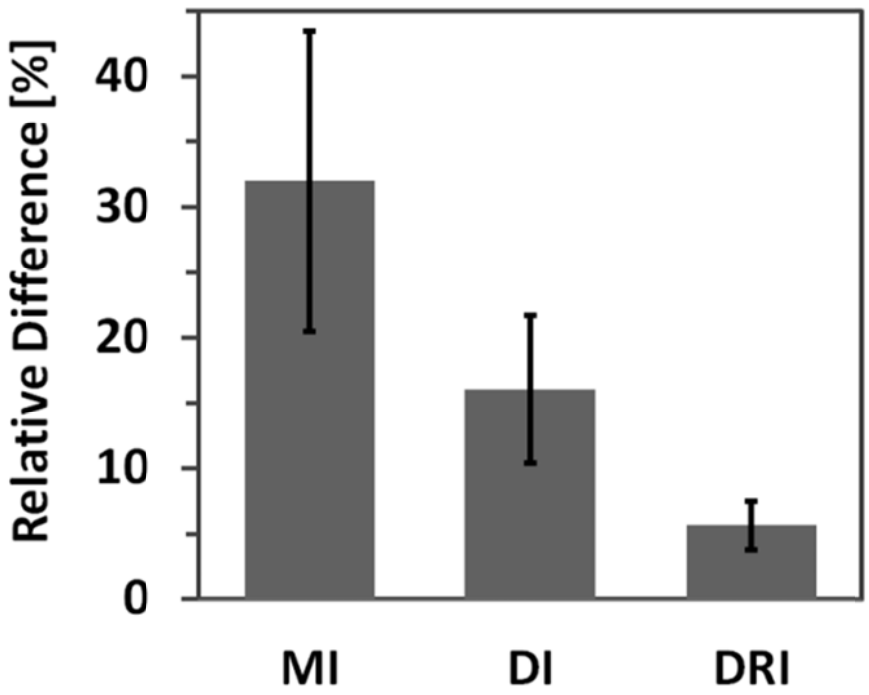

Figure 2.1 Relative difference between GOME-2 and OMI measurement constrained anthropogenic NO_x emission estimates over China using MI [*Martin et al.*, 2003], DI [*Zhao and Wang*, 2009] and improved DRI methods for 2011. The vertical bar shows 1-σ uncertainty.

2.2 Satellite observations and inverse modeling methods

2.2.1 GOME-2 and OMI tropospheric NO_2 columns

Both GOME-2 and OMI instruments are nadir-viewing spectrometers [e.g., *Boersma et al.*, 2004, 2007, 2011]. The OMI instrument was launched onboard the Aura satellite in July 2004, and it has a spatial resolution of 24 × 13 km^2 at nadir [*Levelt et al.*, 2006]. The GOME-2 instrument was launched onboard the MetOp satellite in June 2006 with ground pixel size of 80 × 40 km^2 [*Irie et al.*, 2012]. The local overpass time across the equator is around 9:30 for GOME-2 and around 13:30 for OMI. We excluded the data in all flagged rows with anomalies for the OMI measurements (http://www.knmi.nl/omi/research/product/rowanomaly-background.php). In addition, we only use measured NO_2 column data when cloud fraction is < 20% for both instruments. In MI and DI inversions, we use the Royal Netherlands Meteorological Institute (KNMI) OMI (DOMINO2 v2.0) and GOME-2 (TM4NO2A v2.3) tropospheric NO_2 vertical column density (VCD) products. Comparing these two products, the GOME-2 VCDs are significantly higher than OMI VCDs up to >110% over eastern China in 2011 (Figure A.1 in the Appendix A). Higher GOME-2 VCD values reflect a longer chemical lifetime of NO_x in mid-morning than the OMI observation time of early afternoon [e.g., *Irie et al.*, 2012].

In the DRI method, we re-compute tropospheric NO_2 VCD data using OMI and GOME-2 measurements. In order to maintain consistency in comparison, we use the KNMI algorithm in the retrievals of both OMI and GOME-2 tropospheric NO_2 VCDs [*Boersma et al.*, 2011]. The retrieval procedure includes estimation of NO_2 slant column density (SCD), calculation of tropospheric SCD by subtracting the TM4 assimilated

stratospheric column, and converting the tropospheric SCD into VCD with the tropospheric air mass factor (AMF). The tropospheric AMF calculation depends on a priori tropospheric NO_2 profile, surface albedo, cloud pressure, cloud fraction, and satellite viewing geometry. A more detailed description can be found in *Boersma et al.* [2007]. In the MI and DI methods [*Martin et al.*, 2003; *Zhao and Wang*, 2009], the model simulation of a priori tropospheric profiles is decoupled from inverse modeling. In other words, the emissions used in the model and retrieval are not necessarily consistent with the inverse modeling results. We solve this problem in the DRI method by updating the model emissions and the a priori profiles using inverse modeling results on a daily basis (to be shown in Figure 2.2).

The error in the retrieval of NO_2 tropospheric VCD is determined by those in total SCD, stratospheric SCD, and tropospheric AMF estimation. In this study, we use total and stratospheric SCD errors from KNMI DOMINO2 and TM4NO2A products, and compute the error of tropospheric AMF estimation following the KNMI algorithm. The details of error analysis were described by *Boersma et al.* [2004, 2007, 2011] and *Hains et al.* [2010]. In general, the errors of total and stratospheric SCD estimations are relatively small ($<0.7\times10^{15}$ molec. cm^{-2}) relative to high tropospheric VCDs over eastern China [*Zhao and Wang*, 2009]. The error in tropospheric AMF comes from surface albedo, cloud fraction, cloud pressure, and profile shape. The error from a priori profile can lead to ~10% error in tropospheric VCD retrievals. The total error per retrieval is up to 50% over highly polluted eastern China for both OMI and GOME-2.

2.2.2 REAM model

The 3-D REAM has been applied in a number of tropospheric chemistry and transport studies over East Asia, North America and polar regions [e.g. *Choi et al*., 2005, 2008a, 2008b; *Jing et al.*, 2006; *Liu et al.*, 2010, 2012a, 2012b; *Wang et al.*, 2006, 2007; *Yang et al.*, 2011; *Zeng et al.*, 2003, 2006; *Zhao and Wang*, 2009; *Zhao et al.*, 2009a, 2009b, 2010]. The model has a horizontal resolution of 70 x 70 km^2 with 21 vertical layers in the troposphere. Transport is driven by WRF assimilated meteorological fields constrained by the NCEP reanalysis products (http://www.esrl.noaa.gov/psd/). The chemistry mechanism in REAM is adopted from the GEOS-CHEM model [*Bey et al.*, 2001] with updates of kinetics data (http://jpldataeval.jpl.nasa.gov/). The anthropogenic NO_x and VOCs emissions are from *Zhang et al.* [2009]. The biomass burning emissions are taken from the Global Fire Emissions Database, Version 2 (GFEDv2.1; available at http://daac.ornl.gov/). The lightning NO_x emission is parameterized as by *Zhao et al.* [2010].

2.2.3 Inverse modeling

The MI method for anthropogenic NO_x emissions and uncertainties based on bottom-up and top-down constraints was developed by *Martin et al.* [2003]. We compared the emission estimates by using the updated DI method [*Zhao and Wang*, 2009] with that using the MI method based on KNMI DOMINO2 and TM4NO2A products in Figure 2.1. The improvement from 32% to 16% in the DI method is significant but inadequate, particularly when considering that the difference in the DI method can reach to >32% on a monthly basis (to be shown in Figure 2.4).

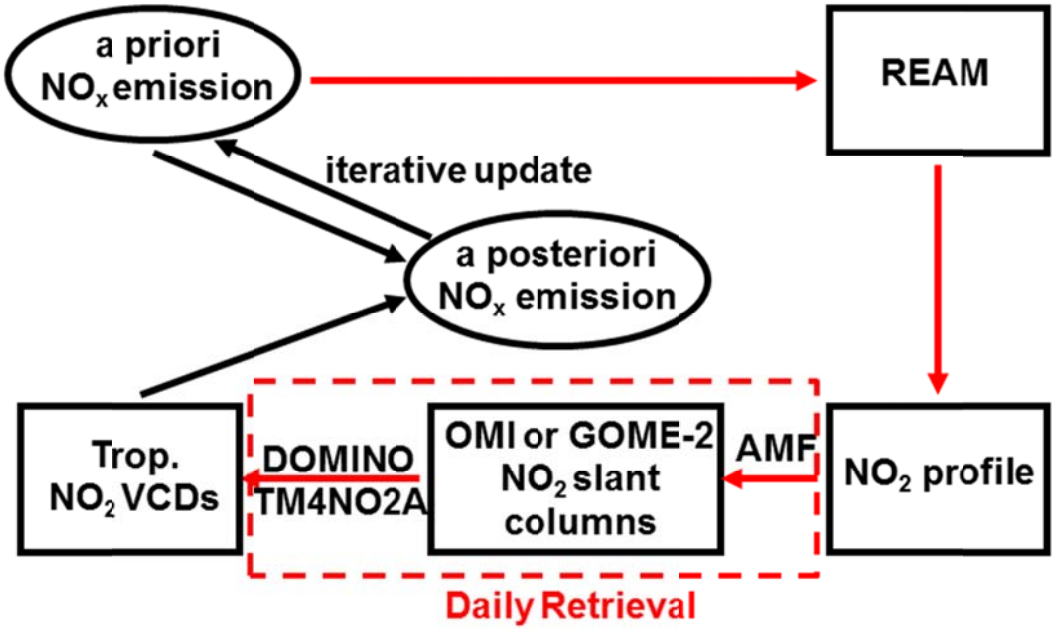

Figure 2.2 Schematic diagrams of the DI (in black arrows) and new DRI (in red arrows) methods. In the DRI method, the daily iterative update includes NO_x emissions, NO_2 profiles, and tropospheric NO_2 VCD retrievals. In the DI method, only NO_x emissions are updated daily. In the DRI method, satellite NO_2 SCD products are used; In the DI method, KNMI DOMINO2 and TM4NO2A tropospheric NO_2 VCD products are used.

In the DI method, only NO_x emission is computed iteratively on a daily basis (Figure 2.2). In this method, which largely follows *Martin et al.* [2003], a top-down emission is estimated by scaling the a priori emission with the ratio of observed and simulated tropospheric NO_2 column. The a posteriori emission is then calculated by error-weighted averaging of the a priori and top-down emissions (the error distributions of the a priori NO_x and the top-down NO_x estimates are assumed to be lognormal). The optimized a posteriori emission and its errors are then used as the a priori in the next day. The whole process iterates daily at the satellite overpass time.

One potential problem in the DI method is that the vertical profiles used in the retrieval are not necessarily consistent with the a posteriori emissions. For example, an increase of emissions will generally increase the vertical gradient of NO_2 profiles and change the AMF values used in the retrieval of tropospheric NO_2 column (section 2.2.1). Furthermore, when we compare the inverse modeling results from two satellite measurements, additional inconsistency can be introduced if the model used to compute NO_2 profiles in AMF calculation is different from the model used in inverse modeling. Figure 2.3 shows REAM simulated monthly mean NO_2 profiles at GOME-2 and OMI overpass times for March, which has the largest monthly mean difference between DI inversion results using KNMI DOMINO2 OMI and TM4NO2A GOME-2 tropospheric NO_2 VCD products for 2011 (to be shown in Figure 2.4). The vertical gradient of NO_2 in the lower troposphere is greater for GOME-2 than OMI since GOME-2 overpass is in mid-morning while OMI overpass is in early afternoon. We did not show in the figure the corresponding profiles from TM4, which are used in the KNMI products, since the TM4 profiles for GOME-2 retrievals were not archived.

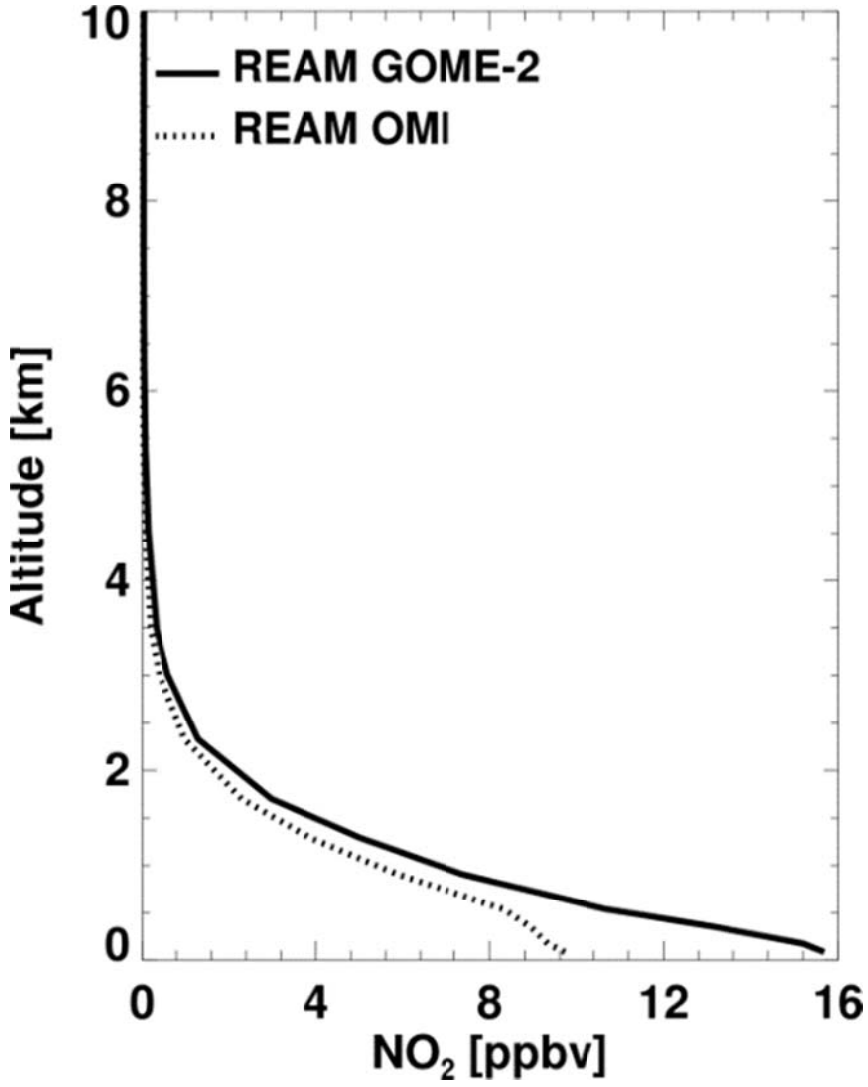

Figure 2.3 Simulated monthly mean NO_2 vertical profiles over Beijing in the DRI method at GOME-2 and OMI overpass times for March 2011.

In the DRI method, we improve NO_x inverse modeling by updating the emissions from the inversion results and subsequently the a priori NO_2 profiles used in the satellite retrieval on a daily basis (Figure 2.2). Tropospheric NO_2 columns are retrieved online daily before inverse modeling. Tropospheric AMFs are first computed with REAM simulated NO_2 profiles and then used in retrieval process to derive tropospheric NO_2 VCD from GOME-2 or OMI NO_2 SCD. The online-computed tropospheric NO_2 VCD is subsequently applied in inverse modeling to estimate the a posteriori emissions and errors. After the inversion, the optimized a posteriori emissions and errors are then used as the a priori in model simulation, satellite retrieval, and inverse modeling in the next day. Therefore we ensure consistency between the posteriori emissions and the NO_2 profiles used in GOME-2 and OMI retrievals.

The uncertainties of the a posteriori emissions are derived from those in a priori and top-down emission estimates. Uncertainties in top-down emission estimates come from those in tropospheric NO_2 VCD retrievals and model simulations. The retrieval error is discussed in section 2.2.1. The uncertainty of model simulation is estimated at 30% and that of the bottom-up inventory is ~60% over China [*Zhao and Wang*, 2009]. The overall uncertainty of the a posteriori emission is typically in the range of 20-40% over polluted eastern China (Figure A.2 in the Appendix A).

2.3 Results and discussion

2.3.1 Comparison between GOME-2 and OMI measurement based inversion results

We showed in Figure 2.1 the yearly relative difference between GOME-2 and OMI measurement based inversion results for NO_x emissions over China using the MI and DI methods, respectively. Although the DI method reduces the annual mean NO_x emission difference between OMI and GOME-2 based inversion results to 16±6% from 32±12% of the MI method, the monthly difference is still quite large, ranging from <10% in December and January to > 30% in March (Figure 2.4). The newly developed DRI method, on the other hand, reduces the difference consistently every month compared to the DI method. The maximum difference in March is reduced to < 12%. The annual mean difference decreases to 5±2%.

Figure A.1 in the Appendix A compares tropospheric NO_2 VCDs between KNMI DOMINO2 OMI and TM4NO2A GOME-2 products and those retrieved by DRI. While the chemical lifetime difference reflected in part in the difference between NO_2 vertical profiles at GOME-2 and OMI observation times (Figure 2.3) and it is expected to yield higher NO_2 VCDs at GOME-2 observation time than OMI, the column difference is clearly much larger between KNMI DOMINO2 OMI and TM4NO2A GOME-2 products than between the corresponding DRI retrievals. A close inspection reveals that the main difference between KNMI and DRI products is in GOME-2 tropospheric VCDs, which the former is much larger. The difference of OMI tropospheric VCDs between KNMI DOMINO2 and DRI retrieved products is much smaller in comparison. Since the TM4 profiles used in KNMI GOME-2 retrievals are not archived, we cannot compare TM4

profiles to those from REAM. We suggest that KNMI makes an effort to archive TM4 profiles used in GOME-2 retrievals, so further analysis can be carried out.

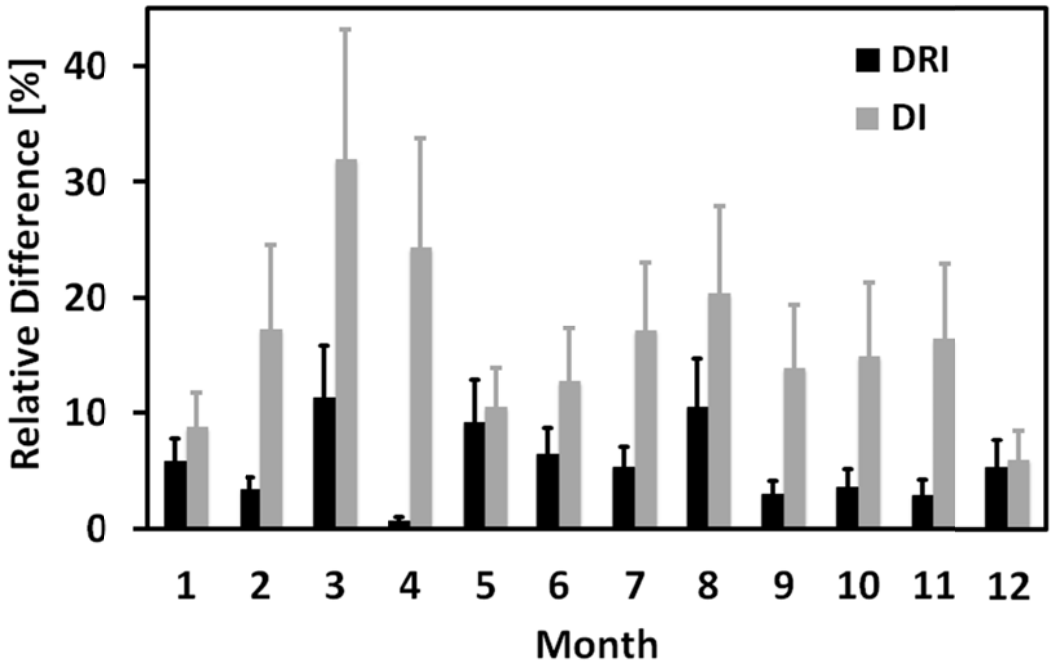

Figure 2.4 Relative differences of monthly average NO_x emission estimates over China between GOME-2 and OMI measurement based inversion results using DRI (black) and DI (grey) methods for 2011. The vertical bars show 1-σ uncertainty.

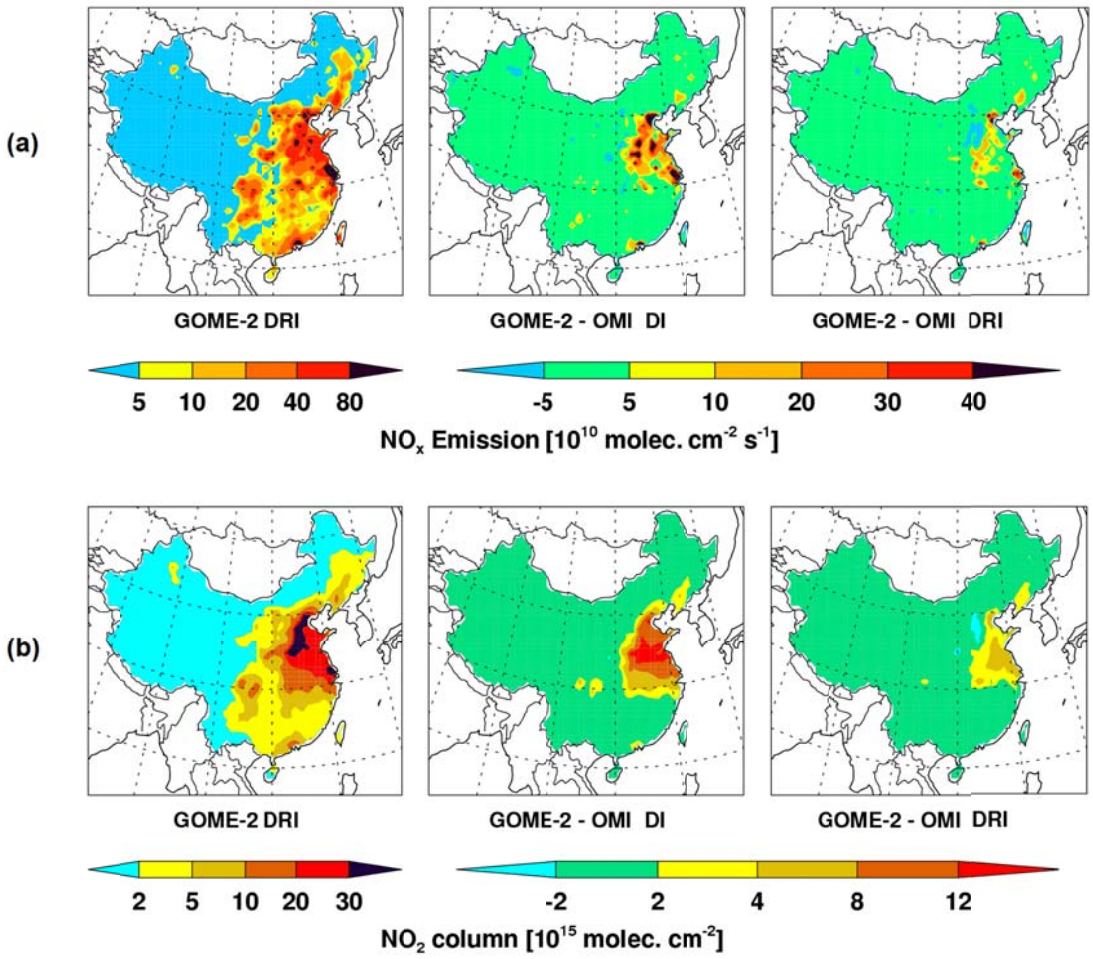

Figure 2.5 (a) Annual mean a posteriori NO_x emission estimates by the DRI method using GOME-2 measurements over China in 2011 (left column), and the differences of annual mean a posteriori NO_x emission estimates by the DI (middle column) and DI (right column) methods between using GOME-2 and OMI measurements over China for 2011. (b) Annual mean simulated daytime tropospheric NO_2 VCDs with using GOME-2 measurements over China in 2011 (left column), and the difference of simulated annual mean daytime tropospheric NO_2 VCDs between GOME-2 and OMI measurement based emission estimates by the DI (middle column) and DRI (right column) methods over China for 2011.

While the aggregated a posteriori emissions in the DRI method are in good agreement between using OMI and GOME-2 measurements, regional differences still exist. Figure 2.5(a) shows the annual mean a posteriori NO_x emissions over China for 2011 by using DRI method with GOME-2 measurements. There are high NO_x emissions in economically developed eastern and southern China. Comparing the a posteriori NO_x emissions from the two satellites, we find much larger differences in a posteriori NO_x emission estimates by using the DI method than the DRI method, especially over polluted eastern China (Figure A.3 in the Appendix A). As shown in the Figure 2.5(a), the a posteriori NO_x emission estimates are consistently higher with GOME-2 than OMI measurements (20-60% over high emission regions) when the DI method is applied. In comparison, the difference are significantly lower (0-20% over high emission regions) when the DRI method is applied. The large positive bias of GOME-2 over OMI based estimates is much reduced.

The average a posteriori anthropogenic NO_x emission over China is 6.9 Tg N/yr with the DRI method and the difference between using GOME-2 and OMI measurements is 0.4 Tg N/yr. In comparison, the OMI and GOME-2 difference between using the DI method with KNMI DOMINO2 and TM4NO2A products is significantly larger at 1.3 Tg N/yr. Considering the uncertainties in satellite measurements, retrieval, and model simulations, these results suggest that the inversion results using the measurements of OMI and GOME-2 are highly consistent when the DRI method is applied in inverse modeling.

In Figure 2.5(b), we compared simulated daytime tropospheric NO_2 VCDs by the DRI and DI methods with GOME-2 and OMI measurements. Simulated tropospheric

NO_2 VCDs are similar to the spatial distribution of satellite retrieved VCDs over China. More importantly, simulated daytime tropospheric NO_2 columns show much smaller differences between OMI and GOME-2 based results by using the DRI than DI method. On average, the simulated column difference decreased from 30% to 7% over eastern China. The high column bias of GOME-2 based results compared to those of OMI is much smaller in the DRI than DI method.

2.3.2 Seasonal variation of anthropogenic NO_x emissions in China

Figure 2.6 shows the monthly mean surface anthropogenic NO_x emission estimates using the DI and DRI methods with GOME-2 and OMI measurements. As shown in the previous figures, the a posteriori emission estimates using the DI method with GOME-2 measurements are noticeably higher than those with OMI measurements. The newly developed DRI method, on the other hand, gives fairly consistent emission estimates with GOME-2 and OMI measurements, well within the a posteriori uncertainties.

The seasonal variation of anthropogenic NO_x emissions has been investigated previously using satellite NO_2 measurements [e.g., *Jaegle et al.*, 2005; *Miyazaki et al.*, 2012]. The DRI emission estimates with GOME-2 and OMI measurements show similar seasonal variations (Figure 2.6). The largest variation is seen in February compared to January and May. The decrease of emissions in February is likely associated with the Chinese New Year holidays. Lower emissions in March to May probably reflect the lower energy consumption associated with transition of heating in winter and cooling in summer. A decrease of emissions to a lesser degree is seen in September and October probably for similar reasons as in spring. A longer term inverse modeling study is

necessary to investigate if the spring and fall decrease pattern persists from year to year. The seasonal pattern of high emissions in winter and low emissions in spring are similar to the bottom-up estimate by *Zhang et al.* [2007] but the emission ratio of 1.4 of December and January to April and May found in this work is higher than that study.

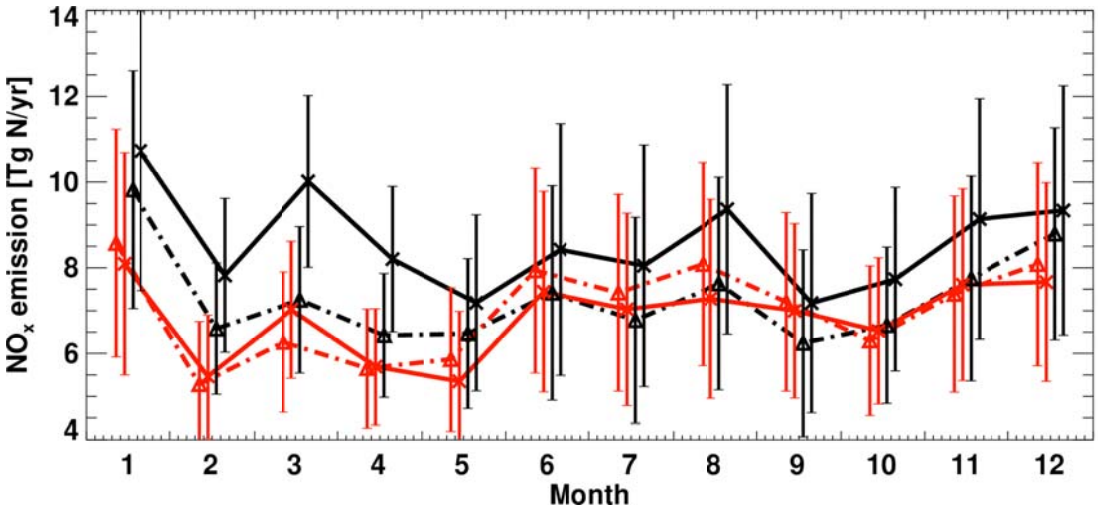

Figure 2.6 Monthly mean anthropogenic NO_x emissions estimates by the DRI (red lines) and DI (black lines) methods with OMI (triangles, dashed lines) and GOME-2 (crosses, solid lines) measurements over China for 2011. The vertical bars show 1-σ uncertainties.

2.3.3 Weekday to weekend emission ratios

A significant weekly cycle of satellite observed NO_2 columns with a minimum value in weekend was found in urban regions in USA, Europe, the Middle East, and Japan [e.g., *Beirle et al.*, 2003; *Boersma et al.*, 2009; *Choi et al.*, 2012; *Kaynak et al.*, 2009]. In contrast, no clear weekend effect was found in cities of China from satellite measurements [*Beirle et al.*, 2003; *Hayn et al.*, 2009]. In our analysis, we find a clearer weekday (Monday-Friday) to weekend (Saturday-Sunday) change signal using the inverse modeling results from the DRI method compared to the DI method. In particular, the weekday to weekend emission ratio tends to be higher over high emission regions. We show the increase of this ratio with anthropogenic NO_x emission in Figure 2.7. The ratio is up to the range of 1.3-1.4, which is similar to a ratio of 1.2-1.5 in urban regions of the U.S. and Europe given in previous studies [*Beirle et al.*, 2003; *Choi et al.*, 2012; *Hayn et al.*, 2009; *Kaynak et al.*, 2009]. For regions with NO_x emissions < 8×10^{11} molec. cm^{-2} s^{-1}, the weekday to weekend emission ratio is close to 1, in agreement with previous analyses.

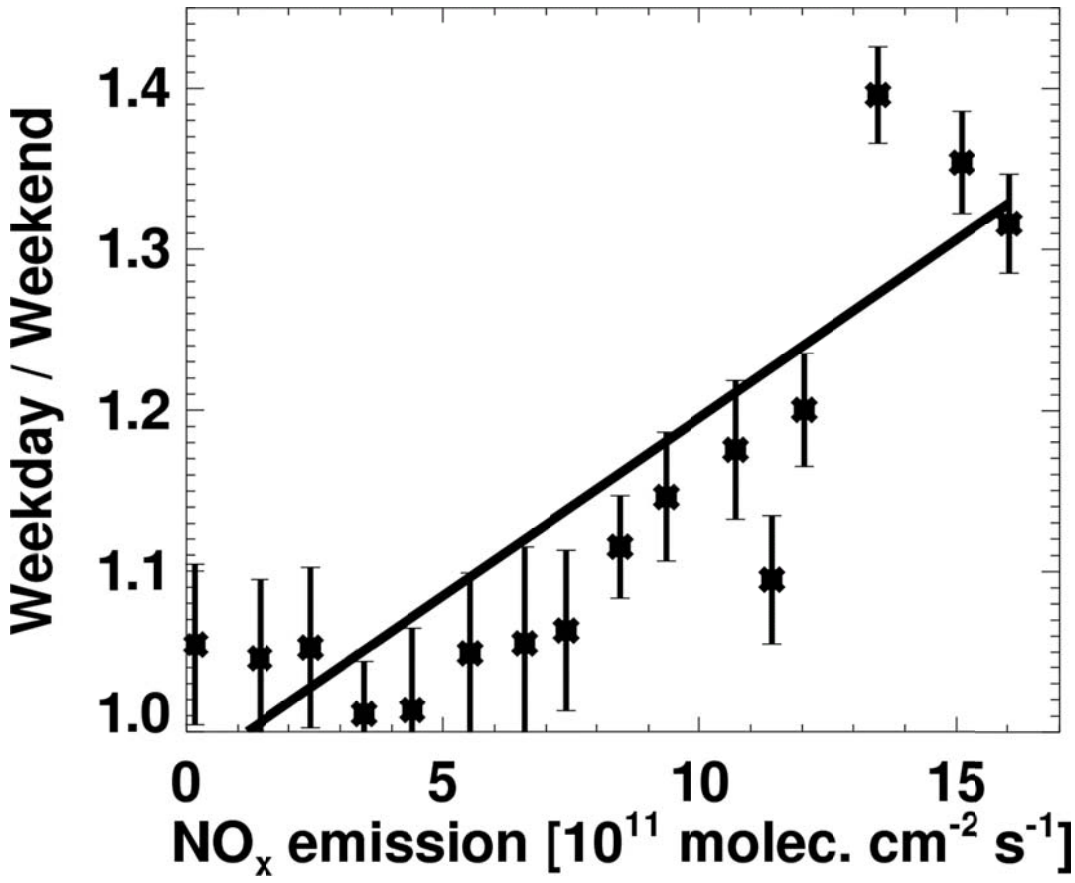

Figure 2.7 Weekday (Monday-Friday) to weekend (Saturday-Sunday) ratio of anthropogenic NO_x emissions as a function of NO_x emission rate over China for 2011. A vertical bar shows the 1-σ uncertainty within each emission bin of 10^{11} molec. cm^{-2} s^{-1}. A least-squares regression is shown by the black line.

2.4 Conclusions

We improve the daily inversion of NO_x emissions by updating the emissions with the inversion results and subsequently the a priori NO_2 profiles used in satellite retrieval on a daily basis. The newly developed DRI method therefore ensures consistency between NO_x emission estimates and the NO_2 profiles used in satellite retrievals in a single modeling framework. We applied the methods to inverse modeling of anthropogenic NO_x emissions over China using GOME-2 and OMI NO_2 column measurements in 2011. The high bias of GOME-2 based emission estimates relative to those based on OMI measurements in the DI method is largely removed in the DRI method. The DRI method significantly reduces the difference of anthropogenic NO_x emission estimates between GOME-2 and OMI data based inversions to 0.3 Tg N/yr from 1.3 Tg N/yr using the DI method. The average emission rate of anthropogenic NO_x is 6.9 Tg/yr over China in 2011. We examine the seasonal and weekly anthropogenic NO_x emission variations in China using the DRI emission estimates. Anthropogenic NO_x emissions are lower in spring and (to a lesser degree) in fall than winter and summer. The emission ratio from December and Januray to April and May is 1.4, while the peak winter and summer month emissions are similar. The weekday to weekend emission ratio tends to increase with NO_x emissions, to the range of 1.3-1.4 in high NO_x emission regions, similar to those previously found in urban regions of the U.S. and Europe. In low and moderate emission regions ($< 8x10^{11}$ molec. cm^{-2} s^{-1}), the weekday to weekend emission ratio is close to 1.

CHAPTER 3

[2]EVALUATE THE UNCERTAINTIES FROM PHOTOCHEMICAL NONLINEARITY IN INVERSE MODELING OF NITROGEN OXIDES EMISSIONS

3.1 Introduction

Nitrogen oxides (NO_x=NO+NO_2) play an important role in tropospheric photochemistry of ozone and secondary aerosol formations. They are emitted from both anthropogenic sources (e.g., fossil fuel combustion) and nature sources (e.g., lightning, soil, and biomass burning). The rapid economic growth in China led to significant increasing of energy consumptions and thereby NO_x emissions during last two decades [*Ghude et al.*, 2009; *Gu et al.*, 2013; *Ma et al.*, 2006; *Mijling et al.*, 2013; *Richter et al.*, 2005; *Stavrakou et al.*, 2008; *van der A et al.*, 2006; *Zhang et al.*, 2007].

The traditional bottom-up emission inventory, which requires detailed information about sources and emission factors, can have large uncertainties in China where the emission information is incomplete [*Streets et al.*, 2003]. In recent years, satellite measurements of nitrogen dioxide (NO_2) from multiple instruments, including Global Ozone Monitoring Experiment (GOME), Scanning Imaging Absorption Spectrometer for Atmospheric Chartography (SCIAMACHY) and Ozone Monitoring

[2]This chapter is an extension of "Evaluate the uncertainties from photochemical nonlinearity in inverse modeling of NO_x emissions" to be submitted. Authors are D. Gu, Y. Wang, R. Yin, C. Smeltzer, and Y. Zhang.

Instrument (OMI), have been widely used to constrain top-down estimation of NO_x emissions as an alternative to the bottom-up emission inventory [*Jaegle et al.*, 2005; *Lamsal et al.*, 2011; *Lin et al.*, 2010; *Stavrakou et al.*, 2008; *Zhang et al.*, 2012].

Inverse modeling of NO_x emissions, incorporating model simulations and satellite observations, can help to reduce uncertainties in bottom-up inventory especially in China [*Lin et al.*, 2012; *Mijling and van der A*, 2012; *Zhao and Wang*, 2009]. *Martin et al.* [2003] developed the first monthly inversion method by scaling the bottom-up emission inventory with top-down constraints from GOME NO_2 column measurements. *Zhao and Wang* [2009] improved the method by carrying out the emission inversion iteratively on a daily basis. One issue that has been gradually discussed is that the inverse modeling results from different satellites can differ significantly. Therefore, *Lin et al.* [2010] tried to combine two satellite measurements together with GEOS-Chem model simulation to minimize the systematic bias between inversion emissions from using different instruments.

It is important to note that most inverse modeling methods were based on assumption that there is a linear correlation between NO_x emissions and NO_2 columns. However, some studies suggested that NO_x emission is not proportional to the changes in NO_2 columns due to nonlinear chemical feedbacks with OH when they analyzed the emission trends based on the observed column trends [*Gu et al.*, 2013; *Lu and Streets*, 2012; *Stavrakou et al.*, 2008]. Under low emission condition, the increasing of NO_x emission leads to enhancement in OH production through $NO+HO_2$ reaction, and then tends to decrease NO_x lifetime due to higher NO_2 loss through OH. On the other hand, under high emission condition, the increasing of NO_x emission leads to enhancement in

OH loss through NO_2+OH, and then tends to increase NO_x lifetime due to the titration of OH. Figure 3.1 compares the model simulated NO_2 column densities with surface emissions at GOME-2 and OMI overpass time over eastern China. The a priori emissions and the Regional chEmical and trAnsport Model (REAM) used in the comparison will be discussed in the next section. The ratios between surface emissions and simulated NO_2 columns gradually decrease with increasing emissions over eastern China, while the ratios are higher at OMI overpass time than those over GOME-2 overpass time.

The substantial nonlinear chemical feedback in changing NO_x emissions and NO_2 columns raises an obvious question of accuracy in potential science applications of these emission estimates. In this study, we examine if the inverse modeling can be further improved by considering the chemical feedbacks. We improve the inversion method by introducing a local derivative ratio to scaling the a priori emission with observed and model simulated columns. The improved method is implemented into the REAM model to optimize surface anthropogenic NO_x emission estimates with GOME-2 and OMI measurements over China in August 2007. The new inversion results are compared to those using the joint two satellites inversion method [*Lin et al.*, 2010] to demonstrate the benefits of the new method.

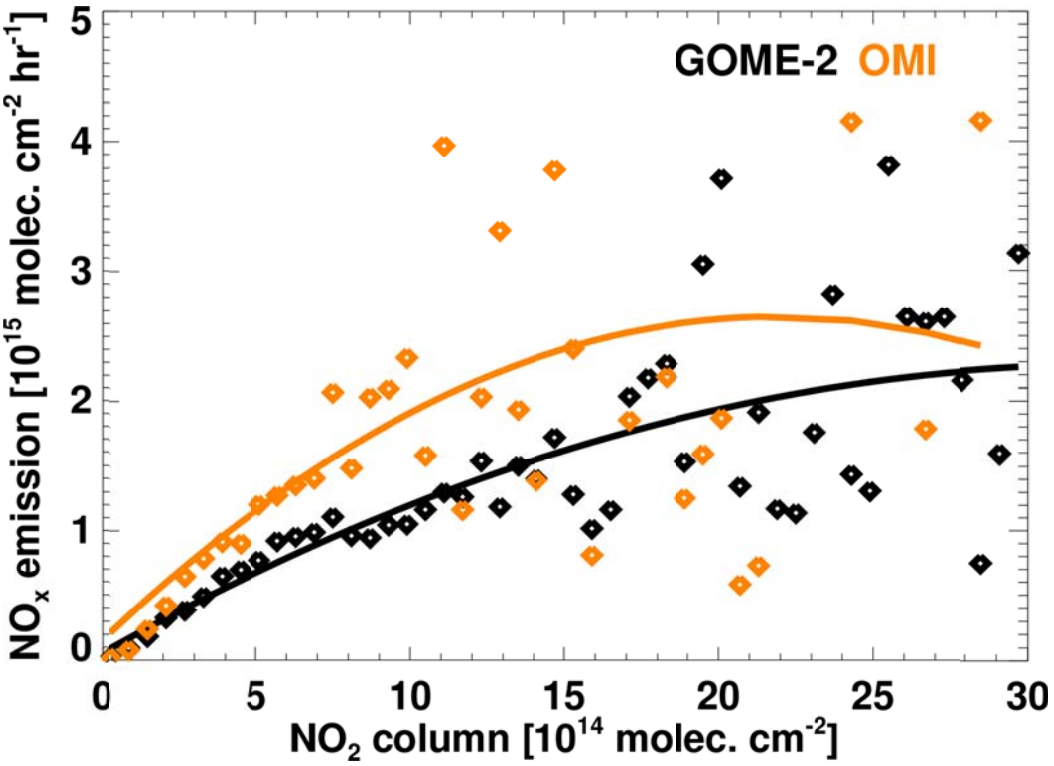

Figure 3.1 NO_x surface emissions versus model simulated NO_2 column densities at GOME-2 and OMI overpass time over eastern China on Aug 2007.

3.2 Satellite data and inverse modeling methods

3.2.1 Satellite data

We use measurements from GOME-2 and OMI instruments in this study. Both instruments are nadir-viewing spectrometers [e.g., *Boersma et al.*, 2004, 2007, 2011]. The OMI instrument was launched onboard the Aura satellite in July 2004, and it has a spatial resolution of 24 × 13 km^2 at nadir [*Levelt et al.*, 2006]. The GOME-2 instrument was launched onboard the MetOp satellite in June 2006 with ground pixel size of 80 × 40 km^2 [*Irie et al.*, 2012]. The local overpass time across the equator is around 9:30 for GOME-2 and around 13:30 for OMI. We excluded the data in all flagged rows with anomalies for the OMI measurements. In addition, we only use measured NO_2 column data when cloud fraction is < 20% for both instruments. In MI and DI inversions, we use the Royal Netherlands Meteorological Institute (KNMI) OMI (DOMINO2 v2.0) and GOME-2 (TM4NO2A v2.3) tropospheric NO_2 vertical column density (VCD) products.

The error in the retrieval of NO_2 tropospheric VCD is determined by those in total SCD, stratospheric SCD, and tropospheric AMF estimation. In this study, we use total and stratospheric SCD errors from KNMI DOMINO2 and TM4NO2A products, and compute the error of tropospheric AMF estimation following the KNMI algorithm. The details of error analysis were described by *Boersma et al.* [2004, 2007, 2011] and *Hains et al.* [2010]. In general, the errors of total and stratospheric SCD estimations are relatively small ($<0.7\times10^{15}$ molec. cm^{-2}) relative to high tropospheric VCDs over eastern China [*Zhao and Wang*, 2009]. The error in tropospheric AMF comes from surface albedo, cloud fraction, cloud pressure, and profile shape. The error from a priori profile

can lead to ~10% error in tropospheric VCD retrievals. The total error per retrieval is up to 50% over highly polluted eastern China for both OMI and GOME-2.

3.2.2 3-D REAM model

The 3-D REAM has been applied in a number of tropospheric chemistry and transport studies over East Asia, North America and polar regions [e.g. *Choi et al*., 2005, 2008a, 2008b; *Jing et al.*, 2006; *Liu et al.*, 2010, 2012a, 2012b; *Wang et al.*, 2006, 2007; *Yang et al.*, 2011; *Zeng et al.*, 2003, 2006; *Zhao and Wang*, 2009; *Zhao et al.*, 2009a, 2009b, 2010]. The model has a horizontal resolution of 36×36 km^2 with 21 vertical layers in the troposphere. Transport is driven by WRF assimilated meteorological fields constrained by the NCEP reanalysis products (http://www.esrl.noaa.gov/psd/). The chemistry mechanism in REAM is adopted from the GEOS-CHEM model [*Bey et al.*, 2001] with updates of kinetics data (http://jpldataeval.jpl.nasa.gov/). The anthropogenic NO_x and VOCs emissions are from *Zhang et al.* [2009]. The biomass burning emissions are taken from the Global Fire Emissions Database, Version 2 (GFEDv2.1; available at http://daac.ornl.gov/). The lightning NO_x emission is parameterized as by *Zhao et al.* [2010].

3.2.3 Inverse modeling methods

In previously developed inversion method, the a posteriori emission is estimated by scaling the a priori emission with ratio between observed and model simulated columns, which can be described as:

$$E = E_a + \alpha \times (\Omega_s - \Omega_m) \quad (1)$$

$$\alpha = E_a / \Omega_m \quad (2)$$

where E is the a posteriori emission, E_a is the a priori emission used in model simulation, Ω_s is satellite observed column, Ω_m is model simulated column and α is the ratio between the a priori emission and simulated column [*Jaegle et al.*, 2005; *Martin et al.*, 2003]. The α ratio in the method is based on the assumption of linear correlation between emissions and columns, which is proper under low emission condition, and will be referred to as 'bulk ratio' in later sections.

As shown in Figure 3.1, one potential problem of using α ratio for inverse modeling is that nonlinear chemical feedback in NO_x-OH cycling significantly changes NO_x lifetime and it has distinct behaviors at two different satellite overpass times. It can not only affect the accuracy of inverse modeling results but also lead to inconsistency between inversion emissions using different satellite measurements. In this study, we introduce a local derivative ratio (α*) as

$$\alpha^* = \Delta E_a / \Delta \Omega_m \qquad (3)$$

where ΔE_a is the change of the a priori emission and $\Delta\Omega_m$ is the change of model simulated column. 3-D REAM model is used to reveal α* over eastern China, and special steps are designed to eliminate the noise of transport on chemical feedback. We firstly add perturbation of emissions (10-15%) to all the grids in the chemistry module in the model. Afterwards in the transport module, to avoid transport of the added perturbation from one grid box to another, the perturbation is only added to a single grid box where the transport is processing. The optimized α* is applied into eq (1) with using both GOME-2 and OMI observations for inversion emission estimation over eastern China in August 2007. The results from using local derivative ratios are also compared with emissions from using bulk ratios in later sections.

The uncertainties of the a posteriori emissions are derived from those in a priori and top-down emission estimates. Uncertainties in top-down emission estimates come from those in tropospheric NO_2 VCD retrievals and model simulations. The retrieval error is discussed in section 2.2.1. The uncertainty of model simulation is estimated at 30% and that of the bottom-up inventory is ~60% over China [*Zhao and Wang*, 2009]. The overall uncertainty of the a posteriori emission is typically in the range of 20-40% over polluted eastern China

3.3 Results and discussion

3.3.1 Comparisons between bulk ratio and local derivative ratio

As shown in Figure 3.1, the ratios between surface emissions and simulated NO_2 columns gradually decrease with increasing emissions over eastern China, which indicates significant nonlinear correlations between two values. We compared the relative difference between α^* and α based on the value of α^* for GOME-2 (left) and OMI (right) inverse modeling over eastern China at August 2007 in Figure 3.2. For both satellites, the values of α^* are smaller (-20~-60%) than the values of α over most high emission regions including east coastal areas and Sichuan Province, while the values of α^* are higher (>20%) than values of α over most low emission rural regions. Comparing the relative difference values for GOME-2 inversion with those for OMI inversion, there are much larger regions with negative values for GOME-2 inversion especially near eat coastal areas, which may reflect the impacts from high emission peak during morning hours.

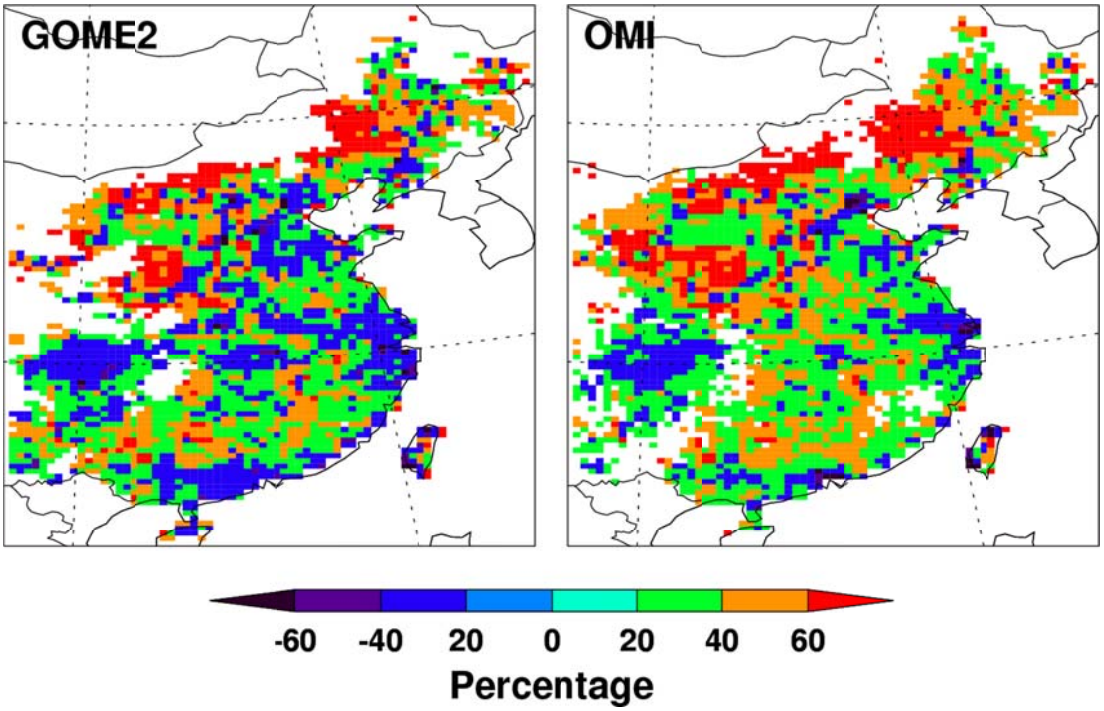

Figure 3.2 Relative difference between α* and α based on the value of α* for GOME-2 (left) and OMI (right) inverse modeling over eastern China for August 2007.

3.3.2 Inverse modeling results

As we mentioned before, one potential problem of using α ratio for inverse modeling is that nonlinear chemical feedback in NO_x-OH cycling significantly changes NO_x lifetime and it has distinct behaviors at two different satellite overpass times, which may cause the significant differences in inversion emissions between using different satellite measurements. To evaluate the inversion results, as shown in Figure 3.3, the relative differences of NO_x inversion emissions between using GOME-2 and OMI measurements by using local derivative ratios are compared with those by using bulk ratios. Over most east coastal regions with high emissions, the inversion results with using GOME-2 measurements are higher (>20%) than results with using OMI measurements, while the results are more consistent between using two satellite measurements by using local derivative ratios than by using bulk ratios.

Furthermore, when we look into the results in three biggest megacities in China, Beijing, Shanghai and Guangzhou, the relative difference of inversion emissions between using GOME-2 and OMI measurements by using bulk ratios are 42.6%, 52.1% and 43.6%, respectively. After using local derivative ratios, the relative difference of emissions between using two satellite measurements are much smaller in three megacities, which are 8.6%, 5.1% and 12.7%, respectively.

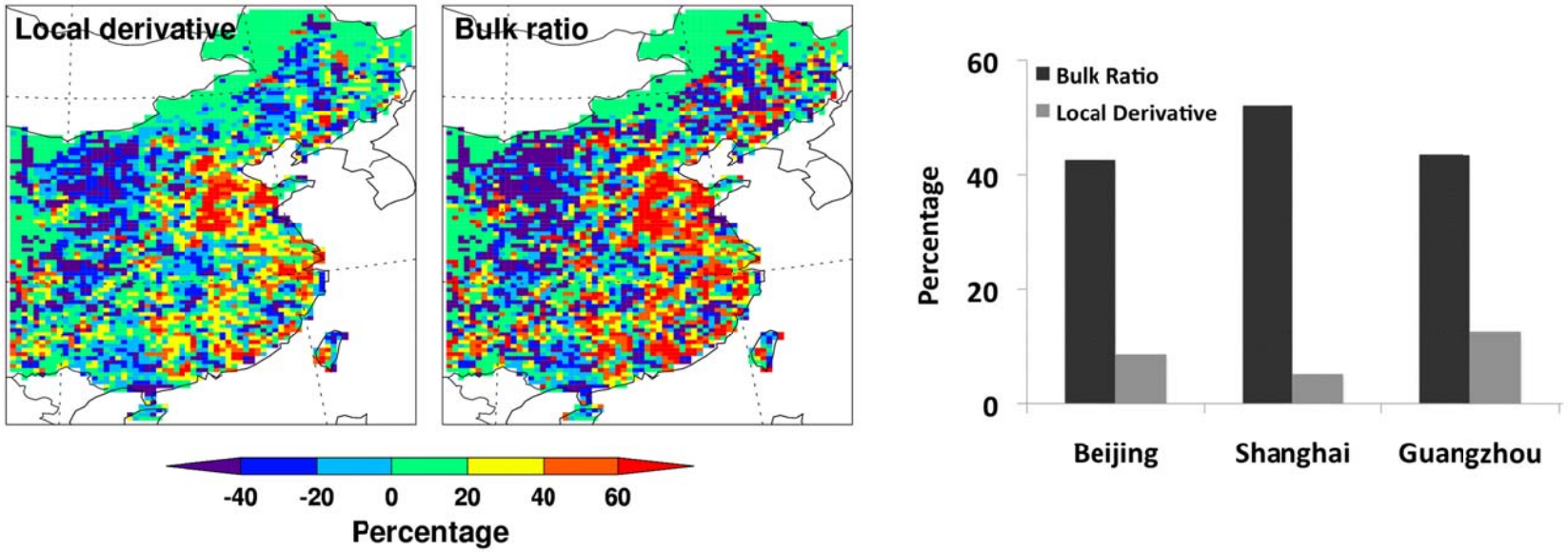

Figure 3.3 Relative differences of NO_x inversion emissions between using GOME-2 and OMI measurements based on their average values by using local derivative and bulk ratios. Regional distributions over east China are in left, and values in three super-megacities are in right.

3.3.3 Inversion results from using joint two satellite methods

In previous studies, in order to reduce the systematic bias of inversion results between different satellites, a joint two satellites method was introduced as

$$\frac{E_j}{E_a} = \frac{\Omega_{OMI} - \Omega_{GOME-2} \cdot \exp(-t/\tau)}{\Omega_{m1330} - \Omega_{m0930} \cdot \exp(-t/\tau)} \quad (4)$$

where E_j is the a posteriori emission, E_a is the a priori emission, Ω_{OMI} is OMI observed NO_2 column, Ω_{GOME-2} is GOME-2 observed NO_2 column, Ω_{m1330} is model simulated NO_2 column at OMI overpass time, Ω_{m0930} is model simulated NO_2 column at GOME-2 overpass time, t is the time gap between two satellite measurements and τ is the lifetime of NO_x [*Lin et al.*, 2010].

In Table 3.1, the inversion emissions by using joint two satellites method are compared with inversion emissions by using local derivative and bulk ratios over eastern China at August 2007. We notice that the results from using joint two satellites method are always smaller than the a priori emissions and all inversion results by using local derivative and bulk ratios with both two satellite measurements. We further look into the variables used in eq (4), and find that the values of $\Omega_{GOME-2}/\Omega_{m0930}$ are always larger the values of $\Omega_{OMI}/\Omega_{m1330}$ over the most high emission east coastal regions (Figure 3.4). This pattern will lead to a consistent smaller E_j than E_a in the equation. In comparison, the results by using local derivative ratios are more consistent between using two satellite measurements.

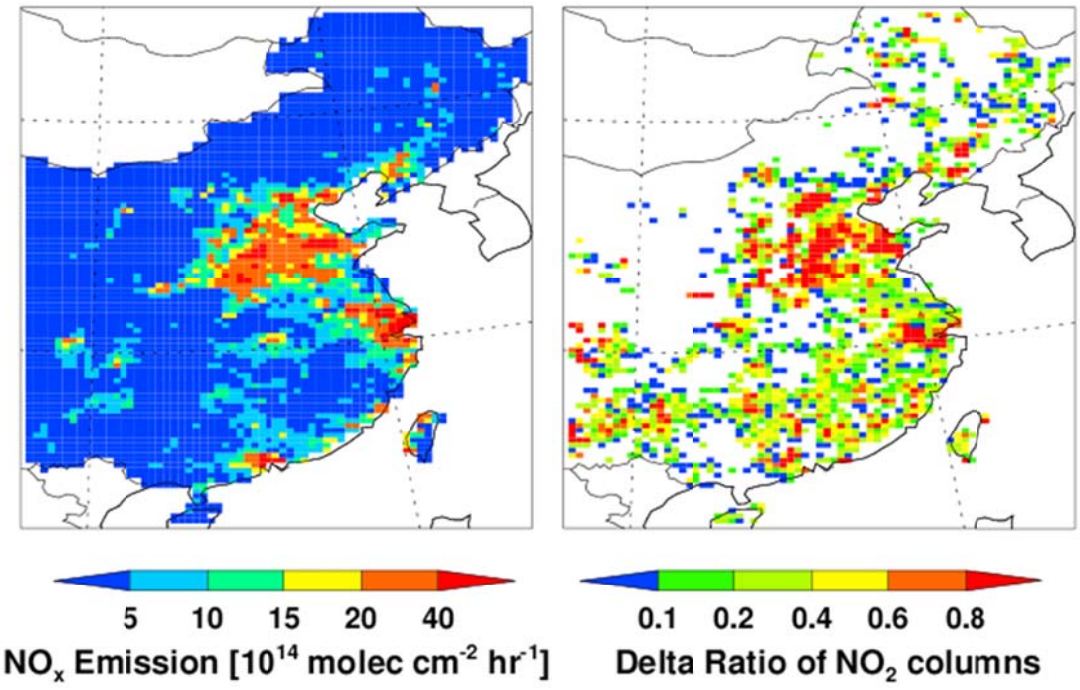

Figure 3.4 NO_x Inversion emission from GOME-2 observations by using local derivative ratio (left), and the values of $(\Omega_{GOME\text{-}2}/\Omega_{m0930})$-$(\Omega_{OMI}/\Omega_{m1330})$ over eastern China (right) for August 2007.

Table 3.1 NO_x inversion emission rates from two satellite inversion method and single satellite inversion method

Method		Emission Rate (10^{15} molec. cm^{-2} hr^{-1})			Total Emission of East China (Tg N yr^{-1})
		Beijing	Shanghai	Guangzhou	
Local derivative ratio	GOME-2	7.78	13.8	4.71	6.18
	OMI	7.14	13.1	4.15	5.82
Bulk ratio	GOME-2	6.86	12.62	8.68	6.13
	OMI	4.45	7.40	5.58	5.50
Joint two satellites method		3.31	7.19	5.32	5.26
a priori emission		9.68	16.9	4.16	5.27

3.4 Conclusions

A methodology is introduced for estimating the local sensitivity of NO_2 vertical column to NO_x emission while explicitly accounting for the uncertainty in the chemical nonlinearity. The new methodology is applied to GOME-2 and OMI NO_2 measurements for inverse modeling of anthropogenic NO_x emissions over eastern China in August 2007.

For both satellites, the local derivative ratios are smaller (-20~-60%) than the bulk ratios over most high emission regions including east coastal areas and Sichuan Province, while the local derivative ratios are higher (>20%) than bulk ratios over most low emission rural regions. Over most east coastal regions with high emissions, the inversion results with using GOME-2 measurements are higher (>20%) than results with using OMI measurements, while the results are more consistent between using two satellite measurements by using local derivative ratios than by using bulk ratios. The inversion emissions by using joint two satellites method are compared with inversion emissions by using local derivative and bulk ratios. Due to the systematic bias, the results from using the joint two satellites method are always smaller than the a priori emissions, which need to be further investigated.

CHAPTER 4

[3]REDUCTION IN NITROGEN OXIDES EMISSION TRENDS OVER CHINA: REGIONAL AND SEASONAL VARIATIONS

4.1 Introduction

The rapid economic growth in China during the last two decades led to a dramatic increase of energy generation and consumption, which significantly increased nitrogen oxides (NO_x=NO+NO_2) emissions and thereby the tropospheric nitrogen dioxide (NO_2) column densities. Previous studies reported increasing trends varying from 5.8% to 10.8% yr^{-1} for NO_x emissions in the past two decades [e.g., *He et al.*, 2007; *Kurokawa et al.*, 2009; *Stavrakou et al.*, 2008]. NO_x emissions in China are mainly driven by power plants and vehicle emissions [*Shi et al.*, 2008; *Wang et al.*, 2010; *Zhang et al.*, 2007]. Recent studies found that NO_x reduction devices have been widely installed in power plants [*Li et al.*, 2010] and higher emission standards have been used to regulate motor vehicles in China [*Saikawa et al.*, 2011; *Wang et al.*, 2010; *Wu et al.*, 2011]. How these control measures affect the NO_x emission trends in China is not yet clear.

The traditional bottom-up inventories of NO_x emissions are estimated using emission source factors and statistical data. They could therefore have large uncertainties in China where the emission information is incomplete [*Streets et al.*, 2003]. Top-down

[1]This chapter is an extension of "Reduction in NO_x emission trends over China: Regional and seasonal variations", published in Environmental Science & Technology in 2013 (Environ. Sci. Technol., 47, 12912−12919). Authors are D. Gu, Y. Wang, C. Smeltzer, and Z. Liu.

inventories, constrained by satellite observations, could help reduce emission uncertainties [*Lamsal et al.*, 2008; *Martin et al.*, 2003]. Measurements by satellite instruments including Global Ozone Monitoring Experiment (GOME), Scanning Imaging Absorption Spectrometer for Atmospheric Chartography (SCIAMACHY) and Ozone Monitoring Instrument (OMI) have been used to estimate the NO_x emissions in China and the long-term trends from last decade [e.g., *Ghude et al.*, 2009; *Han et al.*, 2009; *He et al.*, 2007; *Kunhikrishnan et al.*, 2004; *Kurokawa et al.*, 2009; *Ma et al.*, 2006; *Martin et al.*, 2003; *Richter et al.*, 2005; *Schneider and van der A*, 2012; *Shi et al.*, 2008; *Stavrakou et al.*, 2008; *van der A et al.*, 2006, 2008; *Wang et al.*, 2012; *Zhang et al.*, 2007, 2012]. OMI measurements have also been used to estimate NO_x changes from the 2008 Beijing Olympics Games as well as economic recessions and power plant constructions in China in recent years [*Li et al.*, 2010; *Lin et al.*, 2010; *Witte et al.*, 2009; *Yang et al.*, 2011; *Zhang et al.*, 2009a, 2012].

In this study, we analyzed OMI observations of NO_2 columns over China from 2005 to 2010 and estimated NO_x emission trends using simulations of a 3-D Regional chEmical trAnsport Model (REAM). As we will discuss, the regional and seasonal differences in NO_x emission trends are very large. In particular, the economically developed Pearl River Delta regions, which include Guangzhou, Shenzhen, and Hong Kong, show a clear decreasing trend. Our study focuses on quantifying these emission trends and explores the factors contributing to the reduction of NO_x emission trends compared to pre-2005 periods and the regional, seasonal, and urban-rural variations in the emission trends.

4.2 Methods

The OMI instrument onboard the NASA Aura satellite has a global coverage with a nadir horizontal resolution of 24 × 13 km^2, and passes across the equator at about 13:40 local time [*Levelt et al.*, 2006]. Row anomalies in OMI were found in June 2007 and changed over time. We excluded the data in all flagged rows with anomalies from 2005 to 2010 to obtain a consistent dataset. In addition, we only use NO_2 column data when cloud fraction is < 20% and the column value is greater (by 150%) than the error estimate [*Zhao and Wang*, 2009].

In this study, we calculated tropospheric NO_2 vertical column densities (VCDs) using the KNMI Dutch OMI NO_2 (DOMINO v2.0) retrieval algorithm [*Boersma et al.*, 2011] with a priori profiles from REAM in place of the default KNMI profiles simulated by the coarser-resolution global chemical transport model TM4 [*Heckel et al.*, 2011]. We assume that there is no significant trend in tropospheric NO_2 profiles and used REAM simulated monthly mean tropospheric NO_2 profiles of 2007 as a priori profiles to calculate air mass factors (AMFs) for OMI NO_2 retrievals. As such, the derived emission trends are attributed solely to the observed column NO_2 changes and can be compared to previous column-change based studies [*He et al.*, 2007; *Russell et al.*, 2012; *van der A et al.*, 2008]. The 3-D REAM model has been applied to investigate a number of tropospheric chemistry and transport problems in various locations over the world [e.g. *Choi et al.*, 2005, 2008a, 2008b; *Jing et al.*, 2006; *Liu et al.*, 2010, 2012a, 2012b; *Wang et al.*, 2006, 2007; *Yang et al.*, 2011; *Zeng et al.*, 2003, 2006; *Zhao and Wang*, 2009; *Zhao et al.*, 2009a, 2009b, 2010]. The model used in this study has a horizontal resolution of 70 × 70 km^2 with 21 vertical layers below 10 hPa. The photochemical and dry

deposition modules of REAM were adopted from the GEOS-CHEM model [*Bey et al.*, 2001] with recent updates of kinetics data [*Sander*, 2011]. Meteorological fields were assimilated using the WRF model constrained by the NCEP reanalysis product. The anthropogenic NO_x and VOCs emissions are obtained from the inventory by *Zhang et al*. [2009b]. The biomass burning emissions are taken from the Global Fire Emissions Database, Version 2 (GFEDv2.1; available at http://daac.ornl.gov/). The lightning NO_x emission is parameterized as by *Choi et al*. [2008].

Satellite observations of tropospheric NO_2 columns are closely related with surface NO_x emissions due to the relatively short lifetime of NO_x and higher NO_2/NO_x ratios in the lower troposphere [e.g., *Lamsal et al.*, 2011; *Lu and Streets*, 2012; *Martin et al.*, 2003; *Richter et al.*, 2005]. Some studies assumed a constant proportional relationship between satellite tropospheric NO_2 column and surface emissions in estimating NO_x emission trends [*Kaynak et al.*, 2009; *Martin et al.*, 2003; *Richter et al.*, 2005; *Wang et al.*, 2007; *Zhang et al.*, 2007]. However, the assumption can have large errors due to the nonlinear feedback of NO_x emissions on photochemistry. *Walker et al*. [2010] and *Lamsal et al*. [2011] reduced this error by establishing a variable linear relationship between changes in NO_x emissions (E) and changes in tropospheric NO_2 columns (Ω):

$$\frac{\Delta E}{E} = \beta \times \frac{\Delta \Omega}{\Omega} \quad (1)$$

where ΔE is the change of NO_x emissions and $\Delta\Omega$ is the resulting change in simulated tropospheric NO_2 columns, and β is the local emission-to-column sensitivity. Lu and Streets [2012] showed the nonlinearity in β, the value of which decreased from 2 to 0.7 during 1996-2010 as NO_x emissions and hence NO_2 concentrations over Indian power plants increased. We computed the β values using REAM for a 15% local emission

changes for each grid. Using a smaller (10%) emission perturbation, we obtained essentially the same results. We calculated the mean β values for the year, and warm (June-September) and cool (October-May) seasons, respectively. The change of annual average β as a function of emissions is shown in Figure 4.1. As surface NO_x emission increases, the value of β decreases from 1.5 to 0.7 as the chemical nonlinearity effect becomes more significant. The spatial distribution of β is shown in Figure C.1 in Appendix C. Over high NO_x emission regions of eastern China, the annual mean value of β is in the range of 0.7-0.9, implying that relative anthropogenic emission change is 10-30% lower than NO_2 column change. Our β ratios are lower over eastern China than the global model results by *Lamsal et al.* [2011] (Appendix C).

Applying the β ratios to satellite tropospheric NO_2 column observations, we compute the NO_x emission changes from 2005 to 2010. We then estimate the monotonic trends using the Mann-Kendall method with Sen's slope estimator, which is a non-parametric statistical method and has been applied in long-time trend analysis of NO_x, ozone, and other trace gases [e.g., *Buckley and Mitchell*, 2011; *Carslaw*, 2005; *Cattani et al.*, 2010; *Grant et al.*, 2011; *Shon et al.*, 2011; *Sicard et al.*, 2010, 2011]. By using the Mann-Kendall method, we minimize the impacts of seasonal variations and extreme values in the trend analysis. In this study, only statistically significant trend values (using z-test in the Mann-Kendall method) are reported, and the trend uncertainty is given as the 95^{th} percentile confidence interval.

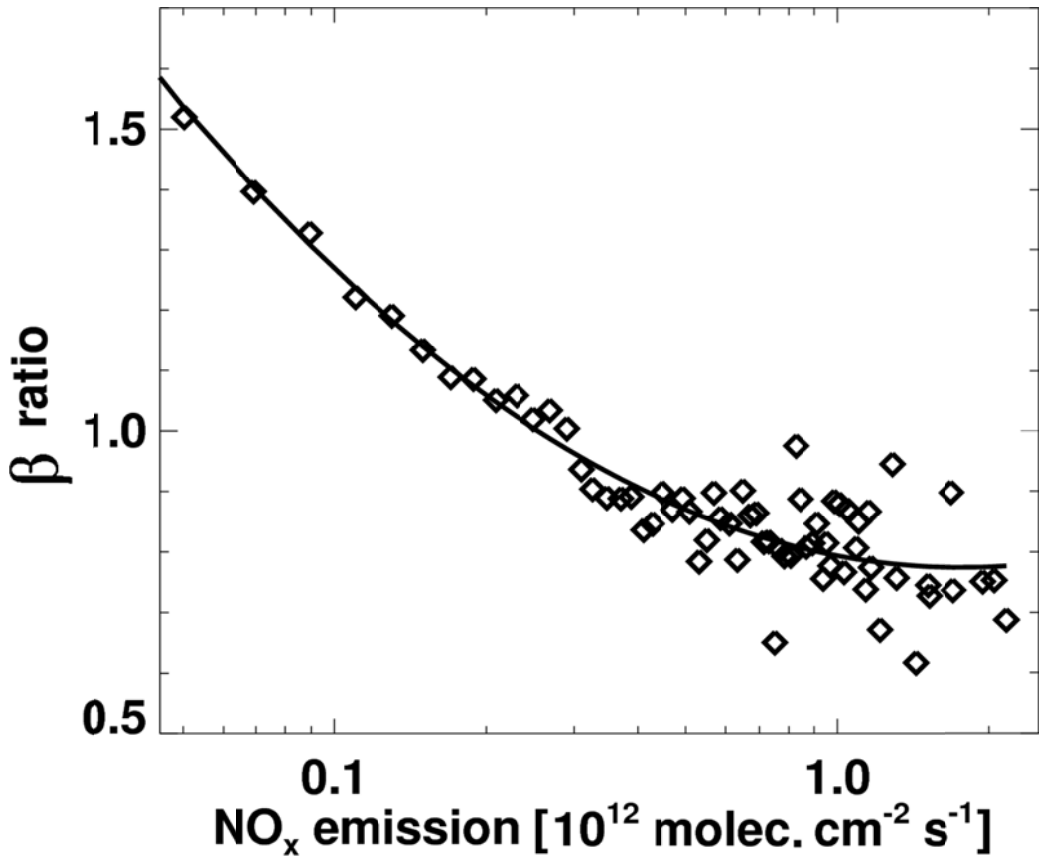

Figure 4.1 Simulated annual average β values as a function of NO_x emission over China in 2007. The data are binned by NO_x emissions with an interval of 2×10^{10} molec cm^{-2} s^{-1}.

Instead of a linearized trend, we compute in this study the compound annual growth rate, which implicitly assumes exponential emission growth [*Kurokawa et al.*, 2009; *Stavrakou et al.*, 2008]. Many previous studies computed a linearized trend over the whole study period, which is normalized to the emission rate in the first year or an average over the study period [e.g., *Ghude et al.*, 2009; *He et al.*, 2007; *Hilboll et al.*, 2012; *Schneider and van der A*, 2012; *Sicard et al.*, 2010; *van der A et al.*, 2006, 2008]. The linearized trend makes it difficult to compare emission rate changes since the normalization year varies among the studies. Furthermore, the implicit assumption of a linearized trend that the per-year (relative) growth rate decreases gradually during the study period cannot be easily justified. A linearized trend normalized to the emission rate in the first year tends to overestimate the growth rate if emission increases and underestimate the reduction rate if emission decreases.

For regional trend analysis, we define 4 regions (Figure C.2 in Appendix C): Northeast China (NEC, 29°-41° N and 108.75°-123.25° E), North China Plain (NCP, 34°-40° N and 113°-120° E), Yangtze River Delta (YRD, 30°-32.5° N and 118°-122° E) and Pearl River Delta (PRD, 22°-23.5° and 112.5°-114° E). Based on correlation analysis of monthly trends, we define June to September as warm season and October to May as cool season in the seasonal analysis.

4.2.1 Impact of economic recession

The Chinese economy went into a recession in late 2008 after the summer Olympic Games and lasted for ~1 year. The total import and export statistics (Figure 4.2) showed continuing growth from 2005 to the middle of 2008, a sudden drop in 2009 coinciding with the recession, and a recovery in 2010. Similarly, the average OMI

tropospheric NO_2 VCDs over China (Figure 4.2) showed corresponding changes. Previous studies found that the economic recession of 2009 had a significant effect on anthropogenic NO_x emissions [*Lin et al.*, 2010; *Schneider and van der A*, 2012]. To properly characterize the trends of NO_x emissions and make comparison with previous studies, we choose to exclude one year data from August 2008 to July 2009 in this work. Including the economic recession period in analysis would result in a decrease of the annual-mean NO_x emission trend over China from 4.01% to 3.87% yr^{-1}.

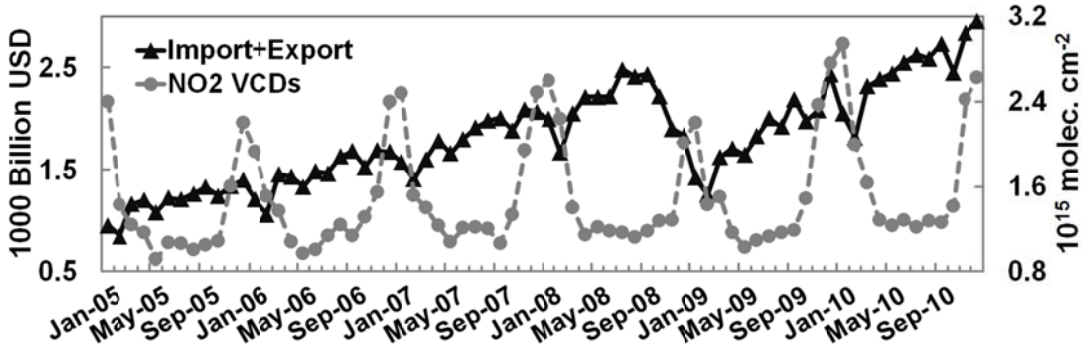

Figure 4.2 Total national import and export in China [*MCC*, 2011], and monthly average tropospheric NO_2 VCDs over China during 2005-2010.

4.3 Results and discussion

4.3.1 Seasonal and spatial variations

Figure 4.2 shows significant seasonal variations in OMI tropospheric NO_2 columns with a maximum in cool season and a minimum in warm season, reflecting in part a shorter photochemical lifetime in warm season. We examine the seasonal variation of NO_x emission trend by month and VCDs (Figure C.3 in Appendix C). While the emission trend is mostly positive generally in a range of 3-5% yr^{-1}, we also find negative emission trend down to -7% yr^{-1} in warm season for high NO_2 VCD regions, indicating potentially significant seasonal variation of NO_x emission trend in high emission regions.

We show in Figure 4.3 the distributions of the annual-mean OMI-derived NO_x emission trends as well as the averages for warm and cool seasons. The most striking spatial feature is the decreasing trend of NO_x emissions over the PRD region. A closer inspection shows another region, in the vicinity of YRD (near Shanghai and nearby Jiangsu and Zhejiang provinces), also has generally lower increasing emission trends or even decreasing trends. In general, NO_x emissions have lower increases over affluent and economically developed coastal regions than less developed and relatively poor inland areas.

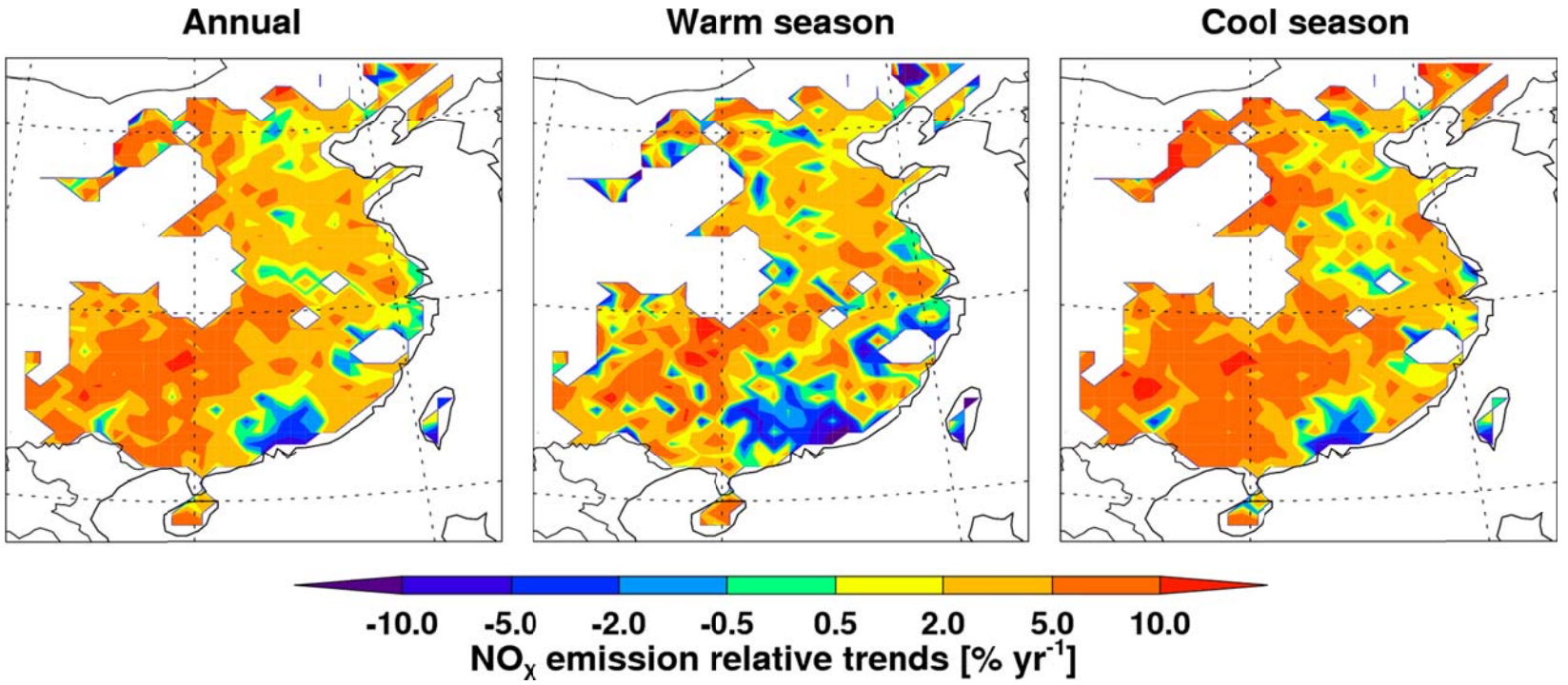

Figure 4.3 Annual and seasonal (warm and cool) relative NO_x emission trends over China during 2005-2010. Warm season is June-September and cool season is October-May.

The spatial distributions of emission trends for warm and cool seasons also follow a similar pattern. However, the average trend of 3.47±1.07% yr^{-1} in warm season is lower than 5.03±1.92% yr^{-1} in cool season. In addition, the warm season distribution shows a much larger negative trend region surrounding PRD than in the cool season. The growth rate of NO_x emissions is in general lower in southern China than northern China, likely reflecting the more extensive consumption of hydropower (e.g. the Three Gorges Dam) generated electricity in the warm season in southern China [*Yu and Qu*, 2013]. We will examine this factor in the next section.

4.3.2 Regional trend variations

We examine here annual trends in different regions to understand the large regional variations (Figure 4.3). Table 4.1 shows that more economically developed and more affluent PRD and YRD regions have lower emission trends than NCP and NEC.

Our estimated national annual compound growth rate of 4.01±1.39% yr^{-1} for NO_x emission is lower than previously estimated NO_x emission trends of 5.8-10.8% yr^{-1} or tropospheric NO_2 column trends of 7.3-29% yr^{-1} during 1996-2006. The previous estimates of emission and NO_2 column trends were summarized in Tables 4.1 and C.1 (Appendix C), respectively. As we discussed previously, a linearized growth rate estimate tends to have a higher increase and lower decrease than a compound growth rate and the difference is about 10% for our study period (Table C.2 in Appendix C). More important is the scaling factor of column to emission trend ratio, β, in the range of 0.7-0.9 over high NO_x emission regions of eastern China, which leads to 10-30% lower relative emission changes than column NO_2 changes (Equation (1), and Tables C.2 and C.3 in Appendix C). After taking into account of methodological difference (20-40%) from previous

studies, the trend of NO_x emissions still appears to have slowed from the rates in 1996-2006. A recent study estimated a bottom-up NO_x emission trend of 5.4% yr^{-1} over China during 2007-2010 [*Zhao et al.*, 2013], which is consistent with our finding. However, we do not have adequate information to compare bottom-up emission trend estimates with the top-down trends in detail. Instead, we focus our discussion on the major factors that could significantly affect NO_x emission trends.

An important policy factor relevant to emission trends during 2005-2010 is the Energy Saving and Emission Reduction Policy. The policy was implemented in the 11th Five-Year Plan (2006-2010) in order to reduce energy consumption per unit of gross domestic product (GDP) by 20% and major pollutant emissions by 10% during the plan period [*Wang and Hao*, 2012]. The Chinese government also put it into the performance evaluation of provincial governors from 2007. Power plants, petroleum industries, iron and steel industries were regulated due to their high-energy consumption and pollutant emissions.

Table 4.1 Comparison of national and regional trends of NO_x emissions over China between this and previous studies.

Period	Region	Annual Trend (% yr^{-1})	Method and References
2005-2010	China	4.01±1.39	OMI - REAM; compound rate; this work
	Northeast China	4.55±1.36	
	North China Plain	4.76±1.61	
	Yangtze River Delta	3.11±0.98	
	Pearl River Delta	-4.39±1.81	
1996-2002	China	5.8	GOME – CMAQ; compound rate; *Kurokawa el al*. [2009].
	North China Plain	7.5	
	Yangtze River Delta	12.3	
1997-2006	China	7.3	GOME & SCIAMACHY - IMAGES CTM; compound rate; *Stavrakou et al*. [2008].
2000-2005	Center East China	10.8	GOME & SCIAMACHY – CMAQ/REAS; linearized rate; *He et al*. [2007].
	Yangtze River Delta	8.2	

An important technology improvement is NO_x emission reduction of thermal power generation. It is required by the Chinese Air Pollutants Emission Standards of Thermal Power Stations (GB13223－2003). During 2006-2010, 76.83 million kilowatt (kW) thermal power generation capacity of small stations was closed, out of a total of 900 million kW total thermal power generation capacity [*SERCC*, 2011; *Zhao et al.*, 2013]. At the end of 2007, nearly 10% of the thermal power generation capacity had applied the Denitration ($DeNO_x$) systems, in which 96% used the Selective Catalytic Reduction (SCR) (nearly 90% reduction efficiency) and 4% used Selective Non-Catalytic Reduction (SNCR) (40% ~ 70% reduction efficiency) [*CAEPI*, 2011; *Liang et al.*, 2011]. It was estimated that 3 million tons of thermal power generated NO_x emissions could be reduced by the end of 2010, which accounts 28% of total thermal power generated NO_x during the period [*CAEPI*, 2008]. The installation of DeNOx systems was initially concentrated in the vicinity of the 4 largest megacities, the impact of which will be discussed in the next section.

These factors alone, however, do not necessarily explain the regional variations in Table 4.1, although power plants in PRD and YRD regions are likely to be preferentially fitted with $DeNO_x$ systems due to stronger enforcements and potentially higher public awareness of environmental issues among the more affluent population [*Huang et al.*, 2012]. One likely important factor is the increasing use of hydro and nuclear power, and it is estimated that hydropower capacity increased by 13% yr^{-1} in China from 2005 to 2010 [*Yu and Qu*, 2013]. The larger increase of hydropower mainly benefits southern China where it is generated [*Lei*, 2005; *McCormack*, 2001].

Among large NO_x emission regions, PRD is the only one showing a significant decreasing trend of NO_x emissions. The specific reasons are not entirely clear. As the most economically developed region in China, PRD is also the first region that made substantial efforts to reduce major pollutant emissions to improve local environments, which appeared to be successful. In addition to using hydro and nuclear power [*Shen et al.*, 1996; *Wu and Siddiqi*, 1995] and implementing more stringent vehicle emission standards in major cities, the rapid closure of energy-inefficient industries and relocation of high-energy consumption industries to inland province could be a major factor [*Ferraro and Brans*, 2012; *Huang and Wei*, 2011; *Tang et al.*, 2010; *Xie*, 2010; *Yang and Yu*, 2010; *Zheng and Qin*, 2009]. Increasing labor costs, the economic recession, and government policies encouraging technology upgrades all appeared to contribute to the observed decreasing emission trend in that region.

4.3.3 Megacity trends and urban-rural difference

The disparity of NO_x emission trends as a function of economic development is more evident for megacities. In Figure 4.4, we show estimated NO_x emission trends for the 4 largest megacities, Shanghai, Beijing, Guangzhou, and Shenzhen, all of which have > 10 million in population and > $100 billion in GDP per year. The annual NO_x relative emission trends of these cities are -0.76±0.29%, 0.69±0.27%, -4.46±1.22% and -7.18±2.88% yr^{-1}, respectively. Guangzhou and Shenzhen, which have negative emission trends, are located in the PRD region. In comparison, we also show in the figure the next 8 major cities ranked by their GDP values in 2009 [*Statistics*, 2010]. The annual relative emission trends of the 4 largest megacities are less than 1% or negative, while the other cities have larger positive trends. Also shown in Figure 4.4 are the emission trends for the

nearby rural regions defined as the surrounding eight grids of a city grid. While the difference between urban and rural regions are relatively small for the other 8 cities, the rural regions surrounding the 4 largest megacities show consistently higher emission trends than the cities, although the rural trends of the 4 largest megacities are still less than the other cities in general.

As mentioned before, $DeNO_x$ systems were gradually applied to thermal power plants in China during 2006-2010, and power plants in the 4 largest megacities were preferentially fitted these systems due to stronger enforcements and higher public awareness [*Yang et al.*, 2009; *Zhang*, 2010]. The use of SCR and SNCR technologies could have significantly reduced NO_x emissions in the 4 largest megacities in past few years, but we expect that the benefit for further emission reduction will taper off where most power plants have these technologies. However, we may begin to see NO_x emission reduction in other cities in future as the use of $DeNO_x$ systems increases in other regions.

Due to rapid economic development, the numbers of on-road vehicles have increased significantly in all Chinese cities. In cities like Shanghai where new vehicle licenses are limited, the number of on-road vehicles did decrease proportionally since residents often bought vehicle licenses from surrounding regions. The fact that the 4 largest megacities showed lower emission trends is likely due to the much stricter vehicle emission standards and more effective enforcement than the other cities [*Saikawa et al.*, 2011; *Wang et al.*, 2010; *Wu et al.*, 2011]. The Euro 3 standard was implemented in 2005, and the Euro 4 standard was implemented in 2008. Guangzhou changed buses and taxi cabs to liquefied petroleum gas (LPG) engines, starting from 2004. By 2007, 80% of buses and all 16000 taxis cabs in Guangzhou were fitted with LPG engines which had

lower NO_x emissions than gasoline engines [*GEPA*, 2008]. The extensive development of metro railways is another reason. The fractions of public transportation by metro railways are 37% in Shanghai, 23% in Beijing, and 15% in Guangzhou by 2009, which are much higher than the other cities [*Statistics*, 2010].

Lastly, the 4 largest megacities are more willing to close small energy-inefficient industries or relocate high energy-consumption industries due to a combination of urban development needs and public environmental concerns. The economic loss from losing these industries can be easily recovered by development of new business in these cities. The Olympics Games in Beijing in 2008, the Asian Game in Guangzhou in 2010, and the World Expo in Shanghai in 2010 likely precipitated the migration of high-emission industries away from these cities.

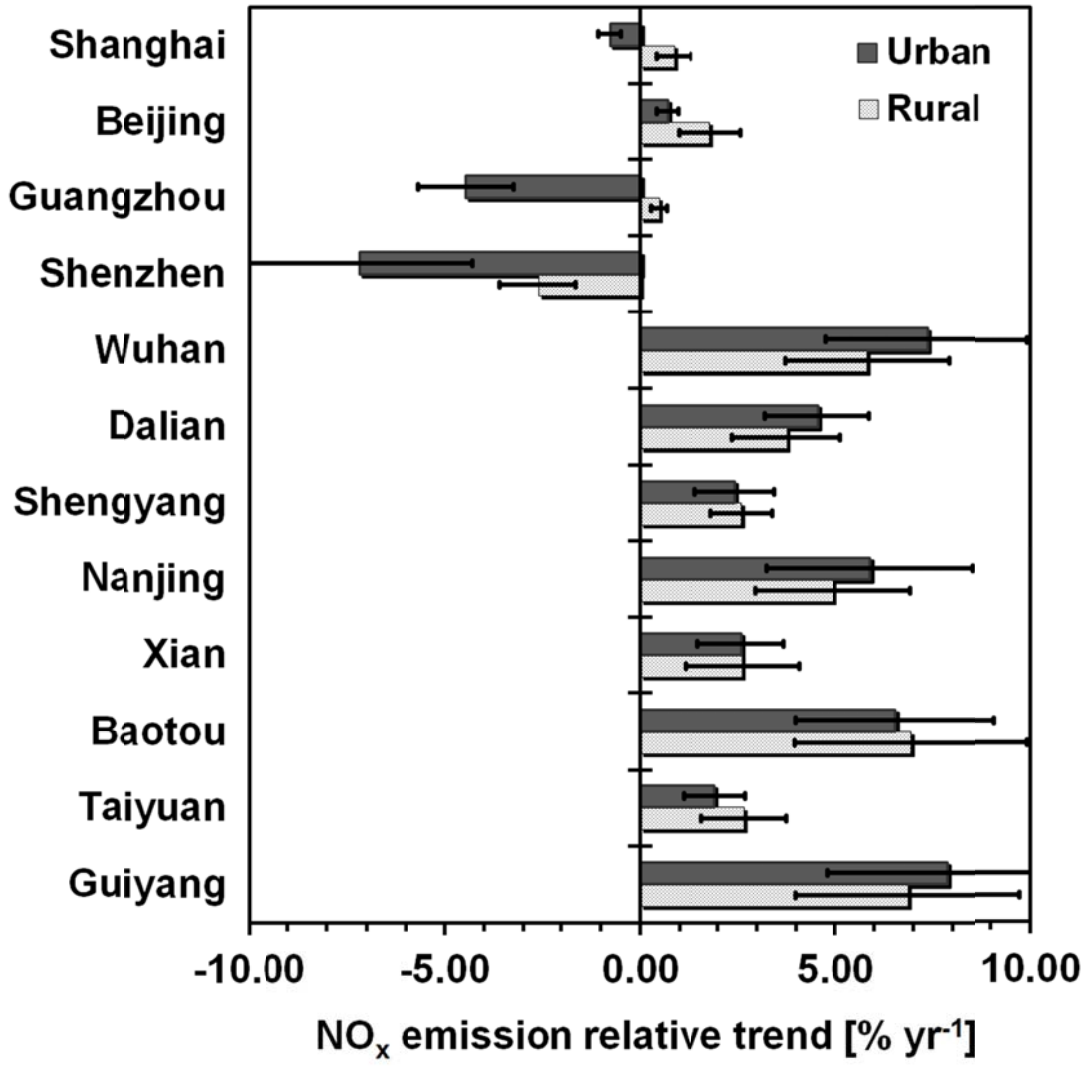

Figure 4.4 Estimated NO_x emission trends for urban and surrounding rural areas of 12 cities ranked by GDP. The error bars show the 95th percentile confidence intervals.

4.3 Implications

We find that using the compound growth rate and accounting for the nonlinear ratio of relative column NO_2 to emission trend are important for estimating NO_x emission trends using satellite column observations. Our estimation of an annual anthropogenic NO_x emission increase of 4.01±1.39% yr^{-1} is significantly lower than previous estimates of 5.8-10.8% yr^{-1} in China over the period of 1996-2006, suggesting a slowdown of NO_x emissions over China in more recent years. The average NO_x emission trend is larger in cool season (5.03±1.92% yr^{-1}) than in warm season (3.47±1.07% yr^{-1}), reflecting in part potentially more extensive usage of hydropower in warm season. The regional difference is even larger. More economically developed and affluent PRD and YRD regions have lower (than NCP) or negative emission trends. The NO_x emission trends of the 4 largest megacities, Shanghai, Beijing, Guangzhou, and Shenzhen are -0.76±0.29%, 0.69±0.27%, -4.46±1.22% and -7.18±2.88% yr^{-1}, considerably lower than the trends of 2-7.8% yr^{-1} of the other 8 major cities. The difference is also apparent when comparing urban emission trends to surrounding regions in these cities. The rural regions surrounding the 4 largest megacities show consistently higher emission trends than the cities, while the difference between urban and rural regions are relatively small for the other 8 major cities.

The lower emission increases (and even decreases) in economically developed regions reflect successful implementation of environmental regulations from direct emission control to industry changes. Looking into the future, it is likely that some of these control measures will be gradually implemented in other megacities and economically developed regions (other than PRD and YRD), which will help reduce emissions growth in those cities and broader regions in China. The implementation of

these measures will likely be slower over rural and less economically developed regions of China, and the rate of emission increase will likely remain high as economy in those regions continues to develop.

CHAPTER 5

[4]EVIDENCE OF VOLATILE ORGANICS EMISSIONS OVER THE TROPICAL PACIFIC

5.1 Introduction

Hydroxyl radical (OH) is the primary oxidant for most traces gases (e.g., CO, volatile organic compounds (VOCs)) in the atmosphere. Oxidation by OH often leads to production of hydroperoxyl (HO_2) radical, which can be recycled back to OH through reactions with NO, O_3, and halogen oxides (e.g., BrO). The cycling of odd hydrogen ($OH+HO_2$, or HO_x) has been extensively studied because of its key role in tropospheric photochemistry and the HO_2/OH ratio was frequently used as indicator of HO_x cycling to evaluate importance of major production and loss processes of OH and HO_2 [e.g., *Brune et al.*, 1998; *Jaegle et al.*, 2001; *Kanaya et al.*, 2007; *Lanzendorf et al.*, 2001a, 2001b; *Ren et al.*, 2008; *Stevens et al.*, 1997].

The Pacific Atmospheric Sulfur Experiment (PASE) provided an observation dataset to investigate the important chemical cycles of HO_x in tropical troposphere, where a large portion of the oxidizing capacity of the atmosphere resides [e.g., *Wang and Jacob*, 1998]. This intensive field study took place near Christmas Island over the equatorial Pacific Ocean (1ºS - 4ºN and 153º - 159ºW) from August 8 through September 6, 2007. It is a relatively clean environment to evaluate our understanding of HO_x chemistry [*Conley*

[4]This chapter is an extension of "Evidence of volatile organics emissions from the ocean over the tropical Pacific" to be submitted in 2014. Authors are D. Gu, Y. Wang, B. Gray, C. Zhao, L. Mauldin, C. Cantrell, B. G. Heikes, A. Higbie, D. W. O'Sullivan, S. Howell, A. Clark, T. Campos, I. Pollack, C. Heizer, and A. Weinheimer.

et al., 2009; *Faloona et al.*, 2009; *Gray et al.*, 2010]. The measured HO_2/OH ratios were generally 50~100 pptv/pptv. However, there were two extreme high HO_2/OH ratios up to 450~550 pptv/pptv in the buffer layer during two daytime research flights, RF12 and RF14 (Figure 5.1), which suggested unusual physical and chemical process of HO_x cycling over tropical oceans.

The HO_2/OH ratio is controlled by NO_x, CO, VOCs, O_3, halogen oxides and other trace gases [*Brune et al.*, 1998; *Lanzendorf et al.*, 2001a, 2001b; *Ren et al.*, 2008; *Stevens et al.*, 1997]. Over the tropical Pacific Ocean, NO_x concentrations are normally very low due to a lack of emission source. Previous studies only measured 2-5 pptv NO_x in the lower troposphere over these regions [*Davis et al.*, 2001; *Wang*, 2000, 2001]. At this level, its effect on HO_x is small [*Gray et al.*, 2010]. CO and O_3 were measured and their concentrations did not vary significantly during the experiment. The large increase of HO_2/OH ratios during RF12 and RF14 therefore may be attributable to two factors: halogen oxides or short-lived reactive VOCs. Previous studies [*Lee et al.*, 2010; *Read et al.*, 2008; *Saiz-Lopez et al.*, 2012] found in the tropical marine troposphere up to 2.8 pptv BrO, which can increase HO_2/OH ratios (e.g., *Saiz-Lopez et al.*, [2008]). Short-lived reactive VOCs may be emitted from the ocean over the tropical Pacific [*Gantt et al.*, 2009; *Matsunaga et al.*, 2002], leading to high glyoxal columns observed by satellites [*Fu et al.*, 2008; *Myriokefalitakis et al.*, 2008; *Vrekoussis et al.*, 2009].

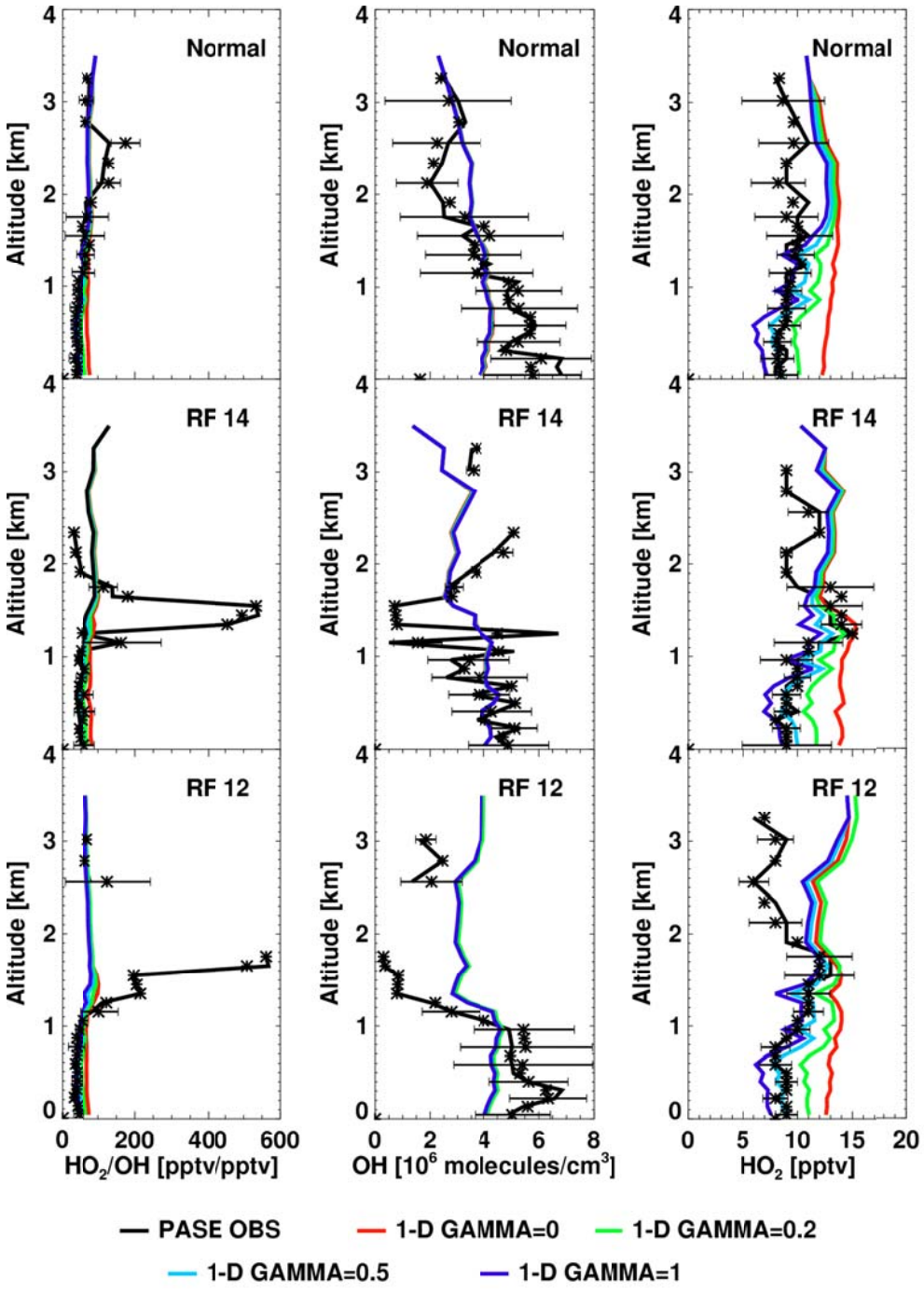

Figure 5.1 Observed and model simulated HO_2/OH, OH and HO_2 with different gamma values during normal flights, RF14 and RF12. Black lines are observation median values, black crosses are observation mean values and standard deviations (±σ) are represented by blanket horizontal lines.

To quantify the effects of these factors on observed high HO_2/OH ratios during RF12 and RF14, we applied a 1-D photochemical transport model to simulate HO_x chemistry and compared to the observations during the PASE experiment. Compared to box model simulations, the 1-D model captures the effects of diffusion and convective transport, and dry and wet deposition on HO_x reservoirs such as H_2O_2 in additional to chemical reactions [*Wang*, 2000, 2001]. While we will discuss the general HO_x chemical cycling as reflected by the PASE observations, we will focus the analysis on the unexpected high HO_2/OH ratios observed in the buffer layer during RF12 and RF14. Based on the WRF simulation, we found that there were two strongest shallow convective events during or just before these two flights. Because the high OH reactivity of VOC species, we hypothesize that fast OH-reacting gases likely in form of unknown oceanic volatile organic compounds are injected into the buffer layer by convection leading to the observed high HO_2/OH ratios.

5.2 Observations and model description

5.2.1 Observations

Fourteen research flights (RF1 to RF14) were conducted during PASE, and the details of flight patterns were discussed in *Conley et al.* [2009] and *Faloona et al.* [2009]. Two nighttime flights (RF6 and RF13), and a flight to sample clouds (RF4) were not included in this analysis. OH, HO_2, organic peroxides (RO_2), hydrogen peroxide (H_2O_2), and methyl hydrogen peroxide (CH_3OOH) were measured (Table 5.1), providing observational constraints on HO_x chemistry over the equatorial Pacific. O_3, CO and water vapor mixing ratios were also measured. Ozone was measured by using a fast chemiluminescence instrument described by *Ridley et al*. [1992]. Aerosol size and

distribution were measured by several different instruments as described by *Clarke et al*. [2004]. The chemical composition of aerosols was measured by the Aerodyne Aerosol Mass Spectrometer (AMS) instrument, and the concentration of organic aerosols is recorded during most flights except RF1, RF9, RF10, RF12 and RF13 [*Bandy et al.*, 2011].

5.2.2 1-D REAM model

REAM is a regional model that has been applied to investigate a number of tropospheric chemistry and transport problems in various locations over the world [e.g., *Choi et al., 2005, 2008a, 2008b; Liu et al., 2012a; Wang et al., 2006; Zhao and Wang, 2009; Zhao et al., 2009a, 2009b; Yang et al., 2011; Gu et al., 2013*]. The photochemical, dry, and wet deposition modules REAM were adopted from the GEOS-CHEM model [*Bey et al.*, 2001] with recent updates of kinetics data [*Sandu and Sander*, 2006]. The 1-D model was constructed from the 3-D REAM model [*Gray et al., 2010; Liu et al., 2010, 2012b*]. The vertical diffusion coefficient used in the model was constrained by DMS observations [*Gray et al., 2010*]. Other meteorological fields used in the 1-D model were assimilated using the WRF model constrained by the NCEP reanalysis product, while the sub-grid convection transport followed the KF-eta scheme [*Kain*, 2004]. The WRF model has a horizontal resolution of 10 x 10 km^2 with 45 vertical layers below 10 hPa. For each flight, 1-D meteorological parameters along the entire flight track are used. Averages over the sampling region are used for hours outside the flight periods.

Table 5.1 Instruments and uncertainties of major measurements during PASE.

Instruments	Species	Detection limit	Accuracy	Reference
SICIMS	OH	2×10^5molecule cm^{-3}	±35%	[*Mauldin et al.*, 2004]
	HO_2, RO_2			
HPLC	H_2O_2	15 pptv	±(15 pptv + 0.1×value)	[*Lee et al.*, 1995; *Osullivan et al.*, 1996]
	CH_3OOH	30 pptv	±(30 pptv + 0.15×value)	
Chemiluminescence	H_2O_2	40 pptv	±(40 pptv + 0.25×value)	[*Cooper et al.*, 2000; *King et al.*, 2007; *Melamed et al.*, 2000]
AMS	Aerosol compositions (Organic, NO_3^-, SO_4^{2-}, NH_4^+)		±50%	[*Shank et al.*, 2012]

The diurnal simulation is run for 30 consecutive days using the same meteorological fields during the flight day to obtain the steady-state 1-D simulations. Sensitivity results indicate running the model for 60 days gives the same results. Daily ozone column data were taken from the OMI measurements. Aircraft sampling encountered cloud on average 2-3% of the time at altitude of 0.75-1.5 km; sunny condition is therefore assumed in the model.

Peroxides, O_3, CO, and water vapor are specified in the model as observed. Observed aerosol size distribution data were used in the model to compute the heterogeneous loss rates. NO_x plays an important role in the HO_x cycle and can impact partitions between OH, HO_2 and peroxy radicals. However, there were no NO_x measurements during PASE. Equatorial Pacific measurements during Pacific Exploratory Mission (PEM) Tropics A and B experiments show NO_x levels at 2-5 pptv in the lower troposphere [*Davis et al.*, 2001; *Wang*, 2000; *Wang et al.*, 2001]. In the tropical lower troposphere, the vertical profile of O_3 provides indirect constraint on NO_x concentrations since the observed O_3 profile shows a rapid decrease from 3 km to surface. In a sensitivity simulation of O_3 vertical profiles, we specified O_3 concentrations at 3 km to the observed value and compared model simulated O_3 profile to the observations. Model simulations show that the simulated O_3 profile matches the observation when NO_x mixing ratio is 5 pptv, and NO_x mixing ratio higher than 10 pptv would lead to an overestimate of O_3 concentrations in the boundary layer (Figure D.1 in the Appendix D). Therefore, we use 5 pptv NO_x as background setup in all further simulations.

There were no VOC measurements during PASE, and we configured the VOCs in the model with observed median values (400 pptv CH_3OH and 20 pptv CH_3CH_2OH) of

PEM Tropics A and B experiments over the equatorial Pacific. For the convective episodes during RF12 and RF14, we specify VOC concentrations by using glyoxal as a proxy for unknown ocean organics. *Sinrench et al*. [2010] measured up to 140 pptv glyoxal over tropic pacific, and we estimate up to 500 pptv glyoxal during the convective episodes which will be discussed in later section.

5.3 Results and discussion

5.3.1 Heterogeneous HO_2 loss

Generally, OH sources can be divided into two groups: (1) reaction of $O(^1D)$ with H_2O followed by photolysis of O_3, photolysis of atmospheric reservoir constituents (e.g. H_2O_2, CH_3OOH) or reactions of O_3 with alkenes; (2) all HO_x cycling reactions converting HO_2 into OH, such as HO_2 reactions with O_3, NO and BrO. OH sinks include reactions of OH with CO, CH_4, O_3, H_2O_2 and most VOCs. For HO_2/OH, a steady state expression can be described as equation:

$$\frac{[HO_2]}{[OH]} = \frac{k_{OH+CO}[CO] + k_{OH+CH_4}[CH_4] + k_{OH+O_3}[O_3] + k_{OH+VOCs}[VOCs]}{k_{HO_2+NO}[NO] + k_{HO_2+O_3}[O_3] + k_{HO_2+BrO}[BrO] + P(OH)_{primary}/[HO_2]} \quad (1)$$

where $P(OH)_{primary}$ is the OH production rate from non HO_2/OH recycling reactions, which is the group (1) OH sources; k variables of HO_2 are reaction rate constants of group (2) OH sources; k variables of OH are reaction rate constants of OH sinks [*Jaegle et al.*, 2001; *Ren et al.*, 2008].

We well simulated the HO_x observations of normal daytime flights by using standard model setups. However, the extreme high HO_2/OH ratios at buffer layer during RF12 and RF14 suggested there were special factors changed the HO_x cycling process

during the two flight periods (Figure 5.1). In order to find out the special factors, we will estimate possible production and loss paths of OH and HO_2.

In previous studies, the conversion reactions of HO_2 to OH easily contributed over half of OH production due to high NO and O_3 levels [*Kanaya et al.*, 2007; *Mao et al.*, 2009]. During PASE, OH production was controlled by photolysis reactions due to special characteristics of the remote tropical Pacific Ocean (e.g., strong radiation, high humidity, low NO_x level). According our model simulation results, because of the high humidity and strong radiation over the tropical Pacific during summer, the production of OH is dominated by the reaction of $O(^1D)$ with H_2O, which contributes 39.7% to total OH production and over 50% of OH production under boundary layer. The photolysis of H_2O_2 and CH_3OOH contribute 26.4% and 8.6% to total OH production, respectively, while reactions of HO_2 with O_3 and NO contribute 19.3% and 2.2%, respectively (Figure D.2 in Appendix D).

Table 5.2 shows the calculated value of major OH production terms based on model simulations. In all selected flights, $P(OH)_{primary}/[HO_2]$ and $k_{HO_2+O_3}[O_3]$ are two largest OH production terms. The $k_{HO_2+NO}[NO]$ is much smaller than $P(OH)_{primary}/[HO_2]$ and $k_{HO_2+O_3}[O_3]$ in the normal flights when we set 5 pptv NO_x level in the model. In RF12 and RF14, in order to get larger HO_2/OH ratio, there only can be smaller amount of NO_x exits, which makes HO_2/OH not as sensitive to NO mixing ratios during this field experiment.

Similar calculation also shows that the PASE environment can only tolerate up to 5 pptv BrO during the normal flights. This 5 pptv BrO assumption is already higher than *Dorf et al.* [2008] and *Read et al.* [2008] measured up to 2.5 pptv BrO in the tropical

troposphere. In RF12 and RF14, in order to get larger HO_2/OH ratio therefore, there is no possibility for any amount of BrO exits. This examination excludes the impact of potential BrO on high HO_2/OH episodes during PASE. While increasing BrO level does not significantly impact HO_2, it will increase OH in the boundary and could help our OH model simulation near the surface. However, existence of 5 pptv BrO can not explain the high HO_2/OH episode since model simulated OH has already been overestimated in the buffer layer during RF12 and RF14.

Table 5.2 HO_2 loss reactivity and primary OH production of HO_2/OH simulations during normal flights in PASE

HO_2/OH (pptv/pptv)	50~100
$P(OH)_{primary}/[HO_2]$ (10^{-3} s^{-1})	1.5 ~ 2.5
$k_{HO_2+O_3}[O_3]$ (10^{-3} s^{-1})	0.8 ~ 1.3
$k_{HO_2+NO}[NO]$ (10^{-3} s^{-1})	0.32 (2 pptv NO)
$k_{HO_2+BrO}[BrO]$ (10^{-3} s^{-1})	$<$ 2.2 ($<$ 5 pptv BrO)

The heterogeneous loss of HO_2 on aerosols and cloud droplets is an important potential sink of HO_x in the troposphere, and has been described by some laboratory researches and model simulations [*Mao et al., 2013; Kanno et al.*, 2006; *Morita et al.*, 2004; *Olson et al.*, 2004; *Thornton and Abbatt*, 2005; *Thornton et al.*, 2008]. Generally, the loss rate of a gas-species on an aerosol can be described into several steps: diffusion of gas-phase species to aerosol surface; mass transfer of species into aerosol bulk; reactions on the aerosol surface; diffusion of species throughout the aerosol bulk [*Thornton et al.*, 2008]. Because the processes are impacted by various factors (e.g. aerosol composition, temperature, pH, O_3 abundance), there are significant uncertainties in heterogeneous loss of HO_2. Normally, a reaction probability of the heterogeneous uptake γ can be defined, and the heterogeneous loss rate of HO_2 can be expressed as

$$\frac{d[HO_2]}{dt} = -\left(\frac{r_p}{D_{HO_2}} + \frac{4}{\gamma\omega}\right)^{-1} A[HO_2] \quad (2)$$

where r_p is particle radius (cm), D_{HO_2} is diffusion coefficient of HO_2 (cm^2), ω is mean molecular speed of HO_2 (cm s^{-1}) and A is aerosol surface area density (cm^2 per cm^3 air). There is no consistent conclusion on γ value within most studies. We examined γ values with 0, 0.2, 0.5 and 1 to test the impact of HO_2 heterogeneous loss on OH and HO_2 during PASE in Figure 5.1. The value changes of γ do not have significant impact on OH and HO_2/OH.

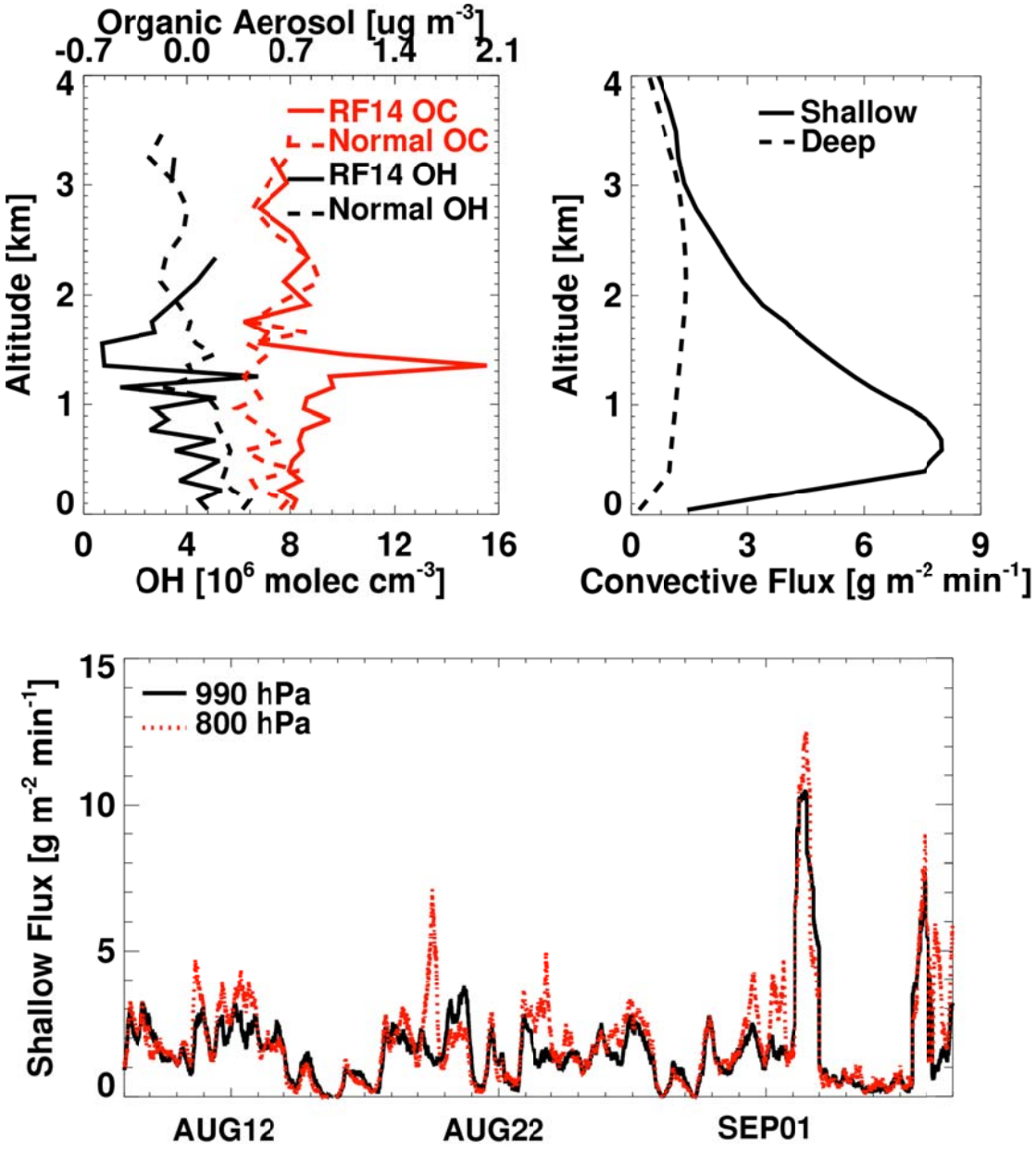

Figure 5.2 Observed OH and organic aerosol during RF14 and normal flights (up-left); the vertical profile of convective flux during PASE (up-right) and the temporal variation of shallow convective flux at 800 hpa and 990 hpa during PASE (bottom).

5.3.2 Potential VOCs emission

Model simulations have rejected the possibility of NO_x and BrO reactions on high HO_2/OH events, and we are going to examine all OH loss terms especially the potential VOCs reaction term. From Figure D.2, two of the most important sinks of OH are reactions of OH with CO and CH_4, which contribute 47.1% and 31.2% of OH loss, respectively. Reactions of OH with H_2O_2, VOCs, O_3 and HO_2, on the other hand, contribute 7.8%, 6.7%, 4.7% and 2.4%, respectively. However, for RF12 and RF14, we underestimated the OH loss terms in the high HO_2/OH events. Because CO, CH_4, and O_3 were constrained by observations and the simulated value of H_2O_2 and HO_2 have been evaluated by observations, the only uncertainty of the OH loss reactions is the concentrations of VOCs.

There is no direct VOCs measurement during PASE. However, Figure 5.2 shows that the mixing ratio of organic aerosol during RF14 was six times larger than normal flights at the buffer layer exactly where the unknown OH loss episode happened (there was no organic aerosol measurement during RF12). Gas phase OH radical reactions with VOCs (e.g., glyoxal, isoprene, monoterpenes) have been identified as important marine sources involved in secondary organic aerosol formation [*Arnold et al.*, 2009; *Bonsang et al.*, 1992; *Gantt et al.*, 2009; *Sinreich et al.*, 2010; *Yassaa et al.*, 2008]. *Sinrench et al*. [2010] measured up to 140 pptv glyoxal over the tropical Pacific. Many studies show that oceanic isoprene can be produced by both phytoplankton and seaweed in marine environments [*Arnold et al.*, 2009; *Broadgate et al.*, 2004; *Moore and Wang*, 2006; *Shaw et al.*, 2003], however the measurement did not detect high isoprene during PEM-TB over similar region. Many studies have reported various VOCs sources over Pacific Oceans

[*Jacob et al.*, 2003; *Marandino et al.*, 2006; *Singh et al.*, 2004]. Organic aerosols can be injected in to air when breaking waves on the ocean surface produce bubbles [*Keene et al.*, 2007]. *Ito and Kawamiya* [2010] and *Lapina et al.* [2011] suggested that organic aerosol source is underestimated in the marine environment. Previous studies suggest marine isoprene SOA may contribute over 50% of sub-micron organic aerosols during the midday hours [*Gantt et al.*, 2009]. Therefore, there is quite possibility that there are unknown VOCs emissions exist during PASE periods.

We investigated the meteorological fields simulated by WRF during PASE. As shown in Figure 5.2, there were two strongest shallow convection fluxes just before RF12 and exactly during RF14. Previous studies suggested that shallow convections can be a driven factor to transport ocean emissions from the surface directly up to the free troposphere, and may even be related to long-term transports [*Doherty et al.*, 2005; *Folkins et al.*, 2006; *Hess*, 2005]. *Tegtmeier et al*. [2012] found that strong convective transport contributed high level organic brominated compounds from the west Pacific Ocean into the stratosphere. *Sahu et al*. [2010] found that the mixing ratios of alkenes were particularly elevated during the episodes of cyclones and convective activities in the summer season. Therefore, two shallow convection events that right before two high HO_2/OH episodes during PASE give us high confidence that ocean VOCs emissions could be transported from surface to buffer layer during two HO_2/OH events.

In order to confirm our hypothesis, we used the high values (500 pptv) of glyoxal in the model simulation to demonstrate their impacts on HO_2/OH ratios after convective transport. As shown in Figure 5.3, OH was rapidly consumed after high values of glyoxal, CH_3OH, and CH_3CH_2OH added in the model during RF12 and RF14. Because

extremely low NO levels lead to slow conversion of HO_2 to OH, HO_2 concentrations are also slightly decreased. Finally, the HO_2/OH ratios are significantly raised for both RF12 and RF14, which confirmed our assumption that the increased convection may transport oceanic VOCs into higher altitude, which then rapidly react with OH and finally raise HO_2/OH.

To test the confidence of our assumption, we also calculated the glyoxal column in our model because the major source of glyoxal in the tropical ocean is the reaction of VOCs and OH. We compared model glyoxal column with satellite observation. For normal flights, the glyoxal column is 1.4×10^{13} molecules cm^{-2}, which is much smaller than GOME-2 satellite observed value of around 2.8×10^{14} molecules cm^{-2} [*Lerot et al.*, 2010] and SMAX-DOAS instrument measured value of 2.1×10^{14} molecules cm^{-2} over the ocean [*Sinrench et al.*, 2010]. After we added high values of VOCs in the model, the convective episode simulations produced 1.1×10^{14} molecules cm^{-2} glyoxal column. The updated value is still below the satellite observed value, it suggests VOCs emissions over tropical pacific during summer are underestimated, and there should be other organic gases or radicals we did not take into account.

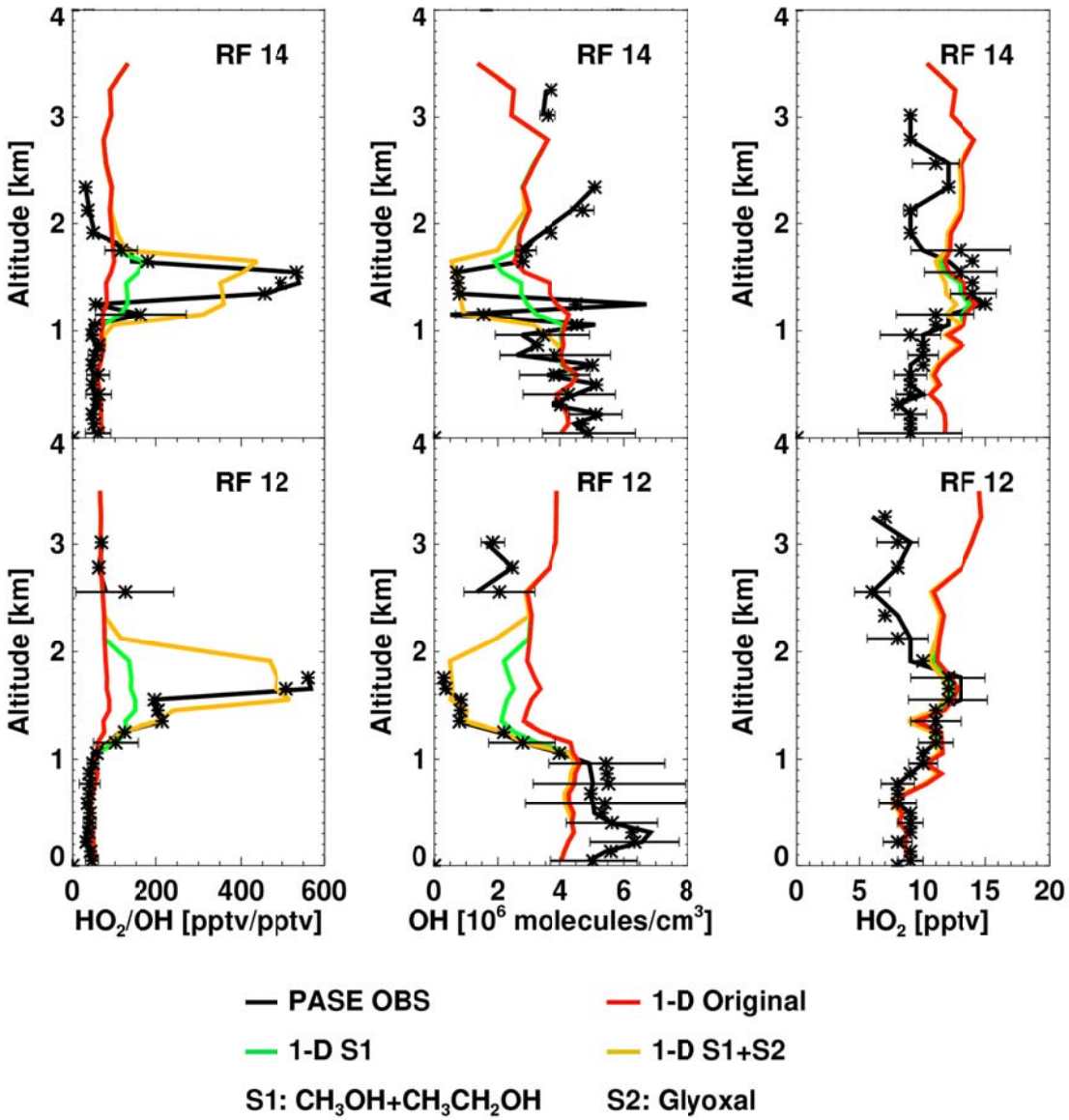

Figure 5.3 Observed and model simulated HO_2/OH, OH and HO_2 with different VOCs scenarios values during RF14 and RF12. Black lines are observation median values, black crosses are observation mean values and standard deviations (±σ) are represented by blanket horizontal lines.

5.4 Conclusions

Based on intensive flight observations during PASE experiments, we analyzed the production and loss cycles of OH over tropical Pacific Oceans by a 1-D model simulation. During the experiment periods, OH production was controlled by the production reaction of $O(^1D)$ and H_2O and the cycling from HO_2 into OH mainly by the reaction of HO_2+O_3, which were impacted by the special characteristics of the remote tropical Pacific Ocean (e.g., strong radiation, high humidity, low NO_x level).

Regarding with the extraordinary high HO_2/OH ratio episodes observed during flight RF12 and RF14, the shallow convective events around the two flights and high organic aerosol mixing ratio in the buffer layer suggests there was potential oceanic VOCs emission transported into buffer layer by convection. By introducing a potential oceanic volatile organic compounds source and convective transport, model well simulated the enhancements of HO_2/OH ratios in buffer layer during experiments. The updated VOCs emissions also improved the glyoxal column in the model compared with satellite observations. The model results confirmed our hypothesis that fast OH-reacting gases likely in form of unknown oceanic volatile organic compounds are injected into the buffer layer by convection, resulting in observed higher HO_2/OH ratios.

CHAPTER 6

CONCLUSIONS AND FUTURE RESEARCH

6.1 Summary of main findings

A 3-D Regional chEmical and trAnsport Model (REAM) simulations are applied to improve the inverse modeling of NO_x emission along with multiple satellite measurements over China. The model is also used to evaluate the uncertainties from photochemical nonlinearity in inverse modeling of NO_x emissions, and examine the regional and seasonal variations in emission trends over China. A 1-D REAM model is applied to examine the potential oceanic volatile organic emissions and their impacts on HO_x cycling over tropic Pacific.

6.1.1 Inverse modeling of NO_x emissions over China

The new daily retrieval-inversion (DRI) method significantly reduces the difference of anthropogenic NO_x emission estimates between GOME-2 and OMI data based inversions to 0.3 Tg N/yr from 1.3 Tg N/yr using the daily inversion (DI) method. The average emission rate of anthropogenic NO_x is 6.9 Tg/yr over China in 2011. We examine the seasonal and weekly anthropogenic NO_x emission variations in China using the DRI emission estimates. Anthropogenic NO_x emissions are lower in spring and (to a lesser degree) in fall than winter and summer. The emission ratio from December and January to April and May is 1.4, while the peak winter and summer month emissions are similar. The weekday to weekend emission ratio tends to increase with NO_x emissions, to the range of 1.3-1.4 in high NO_x emission regions, similar to those previously found in

urban regions of the U.S. and Europe. In low and moderate emission regions (< $8x10^{11}$ molec. cm^{-2} s^{-1}), the weekday to weekend emission ratio is close to 1.

The local derivative ratio is introduced for estimating the local sensitivity of NO_2 vertical column to NO_x emission while explicitly accounting for the uncertainty in the chemical nonlinearity. For both GOME-2 and OMI, the local derivative ratios are smaller (-20~-60%) than the bulk ratios over most high emission regions including east coastal areas and Sichuan Province, while the local derivative ratios are higher (>20%) than bulk ratios over most low emission rural regions. Over most east coastal regions with high emissions, the inversion results with using GOME-2 measurements are higher (>20%) than results with using OMI measurements, while the results are more consistent between using two satellite measurements by using local derivative ratios than by using bulk ratios. The inversion emissions by using joint two satellites method are compared with inversion emissions by using local derivative and bulk ratios. Due to the systematic bias, the results from using the joint two satellites method are always smaller than the a priori emissions, which need to be further investigated.

Our estimation of an annual anthropogenic NO_x emission increase of 4.01±1.39% yr^{-1} is significantly lower than previous estimates of 5.8-10.8% yr^{-1} in China over the period of 1996-2006, suggesting a slowdown of NO_x emissions over China in more recent years. The average NO_x emission trend is larger in cool season (5.03±1.92% yr^{-1}) than in warm season (3.47±1.07% yr^{-1}), reflecting in part potentially more extensive usage of hydropower in warm season. The regional difference is even larger. More economically developed and affluent PRD and YRD regions have lower (than NCP) or negative emission trends. The NO_x emission trends of the 4 largest megacities, Shanghai,

Beijing, Guangzhou, and Shenzhen are -0.76±0.29%, 0.69±0.27%, -4.46±1.22% and -7.18±2.88% yr^{-1}, considerably lower than the trends of 2-7.8% yr^{-1} of the other 8 major cities. The difference is also apparent when comparing urban emission trends to surrounding regions in these cities. The rural regions surrounding the 4 largest megacities show consistently higher emission trends than the cities, while the difference between urban and rural regions are relatively small for the other 8 major cities.

The lower emission increases (and even decreases) in economically developed regions reflect successful implementation of environmental regulations from direct emission control to industry changes. Looking into the future, it is likely that some of these control measures will be gradually implemented in other megacities and economically developed regions (other than PRD and YRD), which will help reduce emissions growth in those cities and broader regions in China. The implementation of these measures will likely be slower over rural and less economically developed regions of China, and the rate of emission increase will likely remain high as economy in those regions continues to develop.

6.1.2 HO_x cycling and volatile organics emissions over tropic Pacific

Based on intensive flight observations during PASE experiments, we analyzed the production and loss cycles of OH over tropical Pacific Oceans by a 1-D model simulation. During the experiment periods, OH production was controlled by the production reaction of $O(^1D)$ and H_2O and the cycling from HO_2 into OH mainly by the reaction of HO_2+O_3, which were impacted by the special characteristics of the remote tropical Pacific Ocean (e.g., strong radiation, high humidity, low NO_x level).

Regarding with the extraordinary high HO_2/OH ratio episodes observed during flight RF12 and RF14, the shallow convective events around the two flights and high organic aerosol mixing ratio in the buffer layer suggests there was potential oceanic VOCs emission transported into buffer layer by convection. By introducing a potential oceanic volatile organic compounds source and convective transport, model well simulated the enhancements of HO_2/OH ratios in buffer layer during experiments. The updated VOCs emissions also improved the glyoxal column in the model compared with satellite observations. The model results confirmed our hypothesis that fast OH-reacting gases likely in form of unknown oceanic volatile organic compounds are injected into the buffer layer by convection, resulting in observed higher HO_2/OH ratios.

6.2 Recommendations for future research

6.2.1 Further analysis on KNMI GOME-2 retrieval

Applying our improved daily retrieval-inversion method, we not only reduced the difference of inversion emission between using GOME-2 and OMI measurements but also improved the NO_2 column retrieval for both instruments. The results suggest that the GOME-2 NO_2 column is overestimated in KNMI product. Since there is no profile data available in KNMI product, we cannot directly compare REAM profiles with TM4 profiles used for KNMI GOME-2 retrieval. We have suggested that KNMI makes an effort to archive TM4 profiles used in GOME-2 retrievals, so we can carry our further analysis.

6.2.2 Uncertainties from transport on inverse modeling

Previous studies suggest that the uncertainties from transport on inverse modeling are relatively small when the model grid size is relatively large. *Zhao and Wang* [2009] estimated that the impact of transport on inversion estimation is relatively small under our 70×70 km^2 REAM grid size. In our study of uncertainties from nonlinear chemical feedbacks on inverse modeling, we modified our inversion process to minimize the impacts from transport. In next step, it would be interesting to evaluate the uncertainties from transport on inverse modeling by using different grid size and distinguish it from other uncertainties.

6.2.3 Further investigation on the oceanic volatile organic emissions

Due to lack of observations, we could not use direct measurements to evaluate our hypothesis of oceanic volatile organic emissions over the tropical Pacific. On the other hand, satellite observations clearly show high glyoxal columns over tropic oceans. Due to the important role of glyoxal in secondary aerosol formation, it would be necessary to investigate the source, the formation and transformation of glyoxal and other possible VOC species over the ocean.

APPENDIX A

AUXILIARY MATERIALS FOR CHAPTER 2

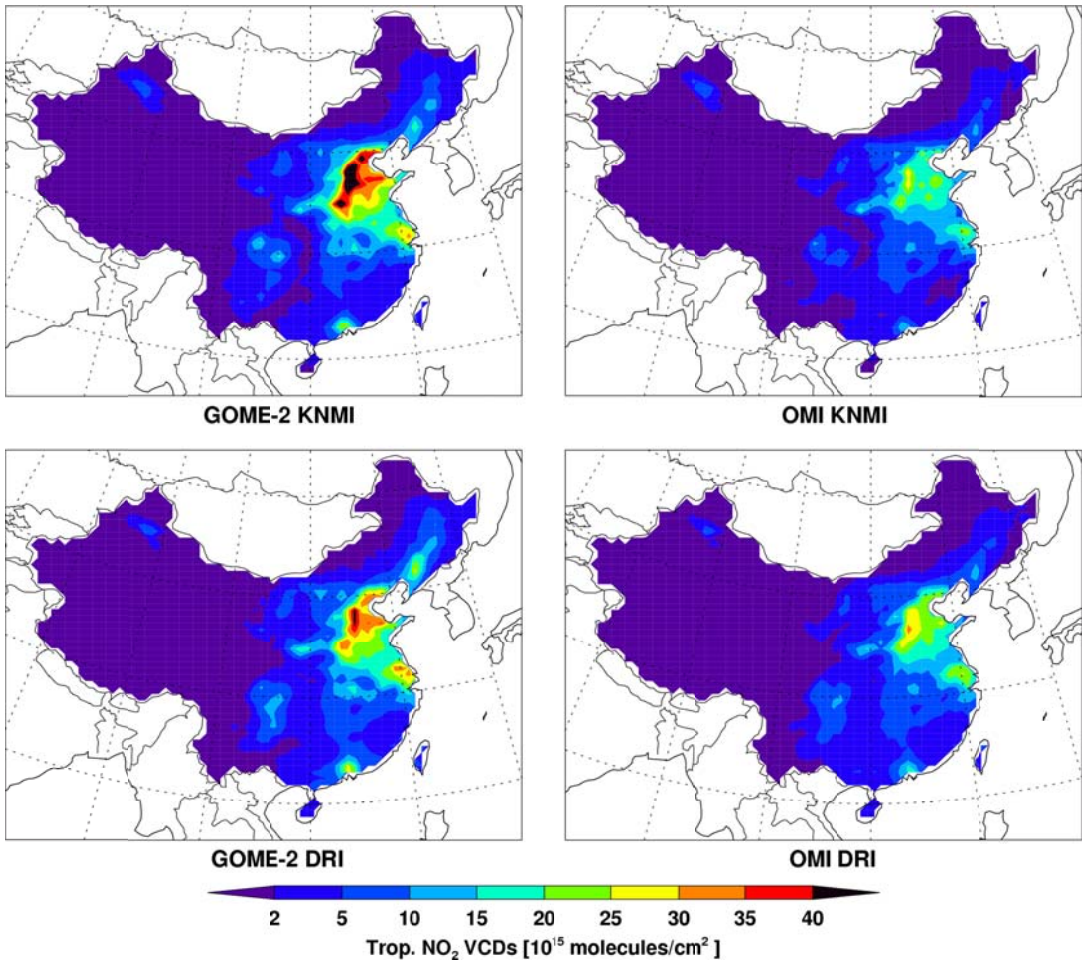

Figure A.1 Annual mean tropospheric NO_2 VCDs from KNMI GOME-2 (TM4NO2A v2.3) and OMI (DOMINO2 v2.0) products (top row), and DRI retrieved GOME-2 and OMI (bottom row) over China in 2011.

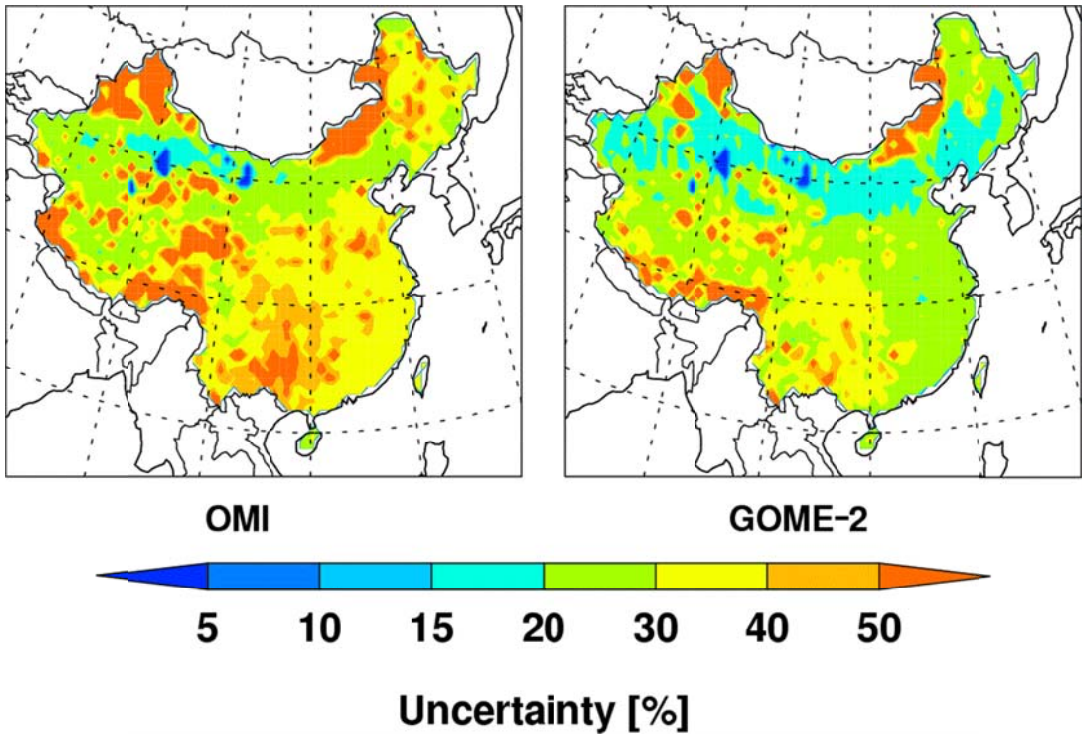

Figure A.2 Annual mean relative a posterior emission uncertainties with the DRI method constrained by OMI and GOME-2 measurements, respectively, over China in 2011.

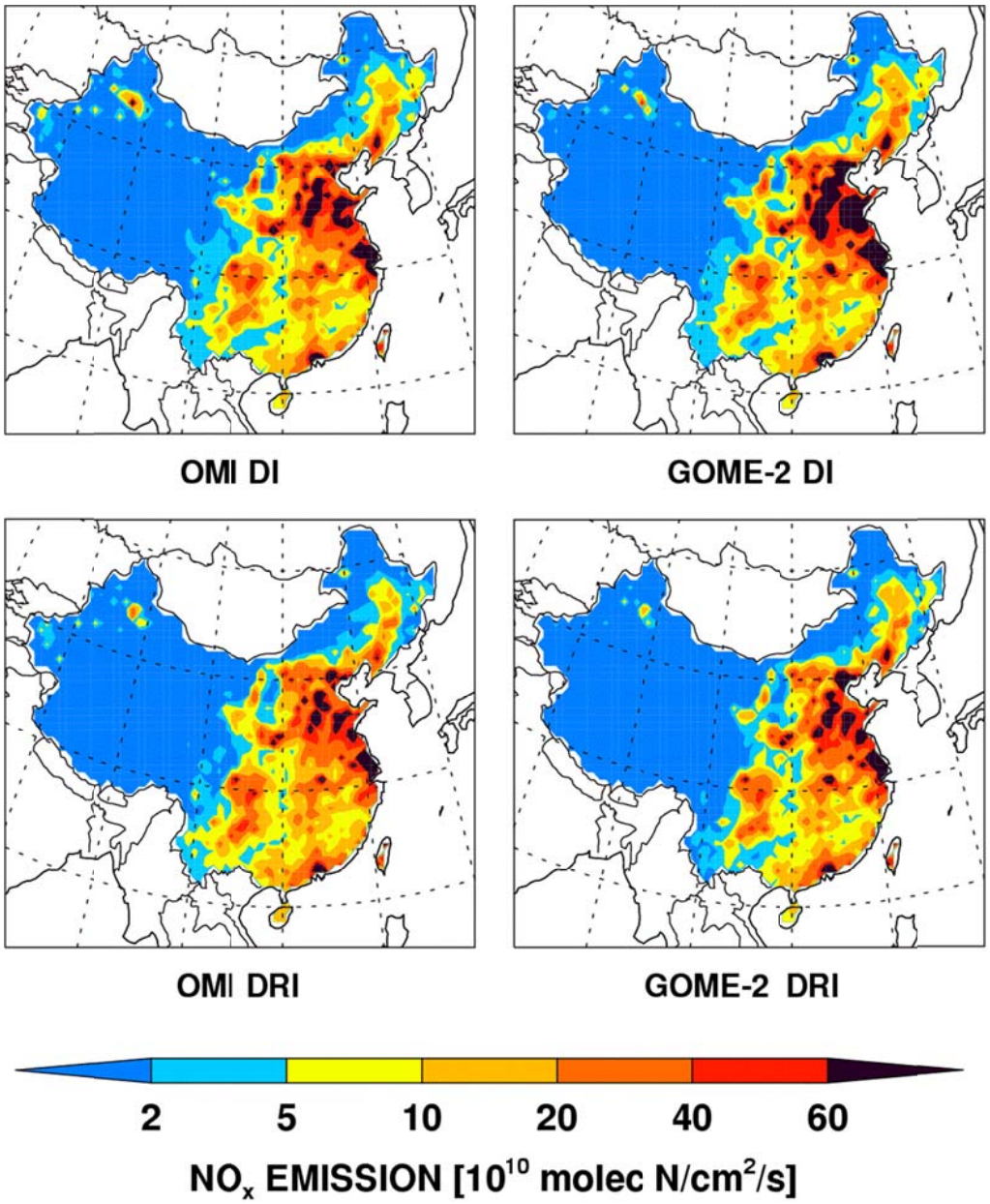

Figure A.3 Annual mean a posteriori NO_x emissions with the DI (top row) and DRI (bottom row) methods constrained by OMI (left column) and GOME-2 (right column) measurements, respectively, over China in 2011.

APPENDIX B

AUXILIARY MATERIALS FOR CHAPTER 3

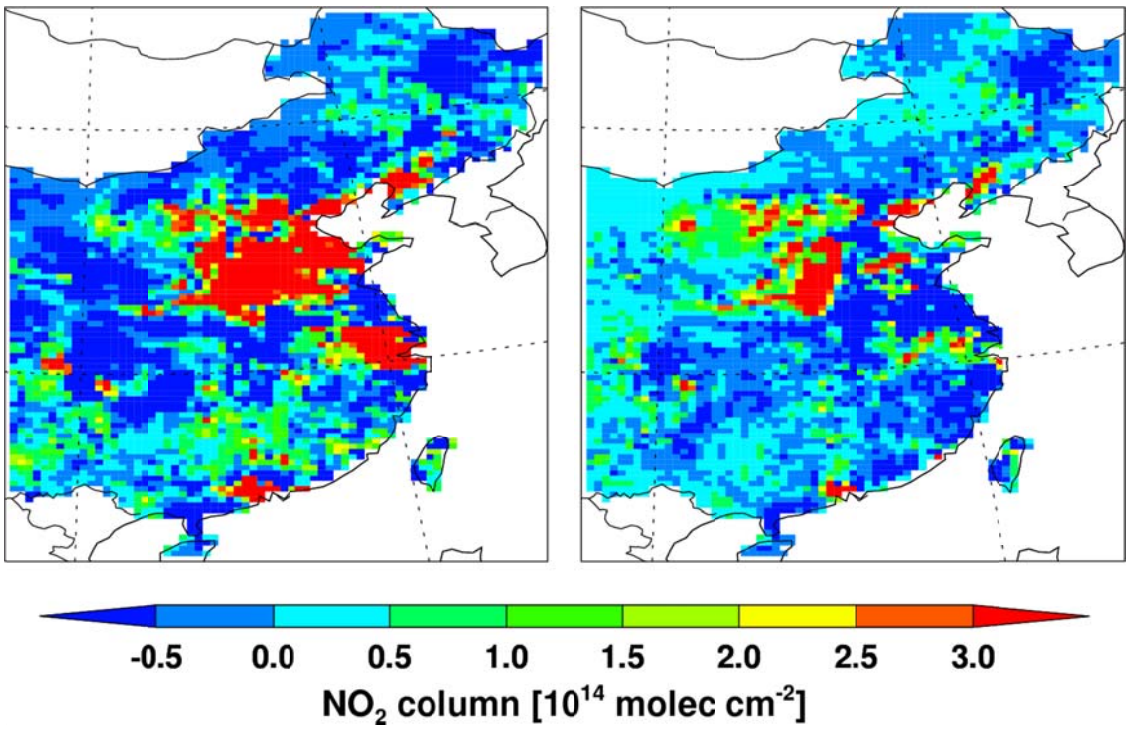

Figure B.1 Difference between satellite observed NO_2 column and model simulated NO_2 column at GOME-2 overpass time (left) and OMI overpass time (right) over China on Aug 2007.

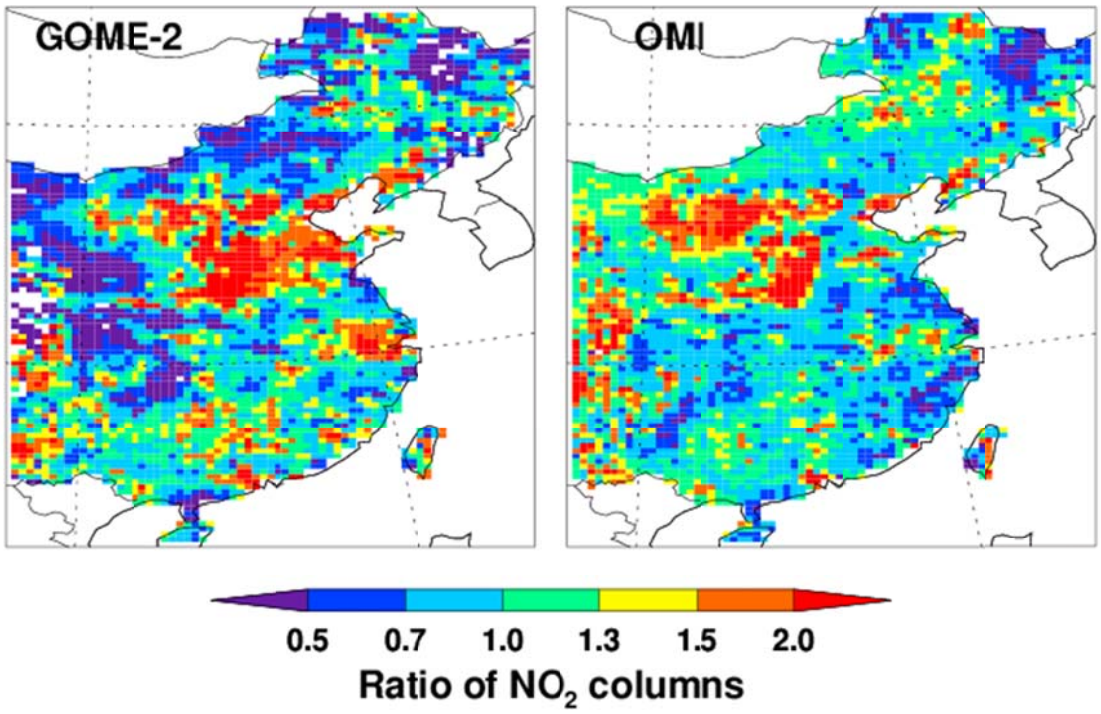

Figure B.2 Ratios of GOME-2 observed NO_2 columns over model simulated NO_2 columns (left), and OMI observed NO_2 columns over model simulated NO_2 columns (right).

APPENDIX C

AUXILIARY MATERIALS FOR CHAPTER 4

The supporting information describes: (1) Summary of NO_2 column trends in previous study results (Table C.1); (2) β value distribution (Figure C.1); (3) Relative emission and VCD trend estimates in this work (Table C.2 and C.3, Figure C.2 and C.3).

C.1 Summary of NO_2 column trends in previous study results

We summarize previous estimates of NO_x emission trends (Table 4.1 in Chapter 4) and NO_2 column trends (Table C.1) over different regions in China. The ranges are 5.8-10.8% yr^{-1} for NO_x emission trends and 7.3-29% yr^{-1} for NO_2 column trends over China.

Table C.1 Top-down estimates of relative annual trends of NO_2 columns over China in previous studies. Note that trends are based on linearized growth rate.

Period (Reference)	Methods	Region	Trend (% yr^{-1})
1996-2006, [*Ghude et al.*, 2009]	GOME & SCIAMACHY	China	11±2.6
1996-2006, [*van der A et al.*, 2008]	GOME & SCIAMACHY	China	Up to 29
		Beijing	11±3
1996-2005, [*van der A et al.*, 2006]	GOME & SCIAMACHY	Beijing	10±4
		Pearl River Delta	9±6
		Jinan	11±2

		Shanghai	20±5
		Shenyang	16±6
		Xian	6±3
		Chengdu	9±2
		Chongqing	12±3
		Harbin	9±4
		Urumqi	11±3
1996-2004, [*Richter et al.*, 2005]	GOME & SCIAMACHY	China	Up to 12
2000-2005, [*He et al.*, 2007]	GOME & SCIAMACHY	Center East China	14.1/20.5 20.1/25.2 (Dec-Feb) 9.9/16.8 (Mar-Nov)
		Beijing	14.3/23.1 21.1/24.2 (DJF) 9.2/22.2 (M-N)
		Yangtze River Delta	17.6/27.5 17.3/25.8 (DJF) 17.7/29.0 (M-N)
		RC	14.5/18.4 22.1/26.0 (DJF) 9.3/13.4 (M-N)
2002-2011, [*Schneider and van der A*, 2012]	SCIAMACHY	China	7.3±3.1
		Beijing	2.48±1.14
		Shanghai	3.26±1.07
		Guangzhou	-1.57±1.22

C.2 β value distribution

Figure C.1 shows the distribution of annual mean β value computed in the REAM model for 2007. The distribution reflects the general anti-correlation between β and NO_x emission. Over East China, the annual mean value of β is in the range of 0.7-0.9, implying that relative anthropogenic emission change is 10-30% lower than column NO_2 change. This result is consistent with the finding by Lu and Streets [2012]. Our results have similar regional patterns as in the earlier study by Lamsal et al. [2011], although our β values over the North China Plain are smaller likely reflecting a larger nonlinear effect of NO_x chemistry due in part to a higher model spatial resolution in this work.

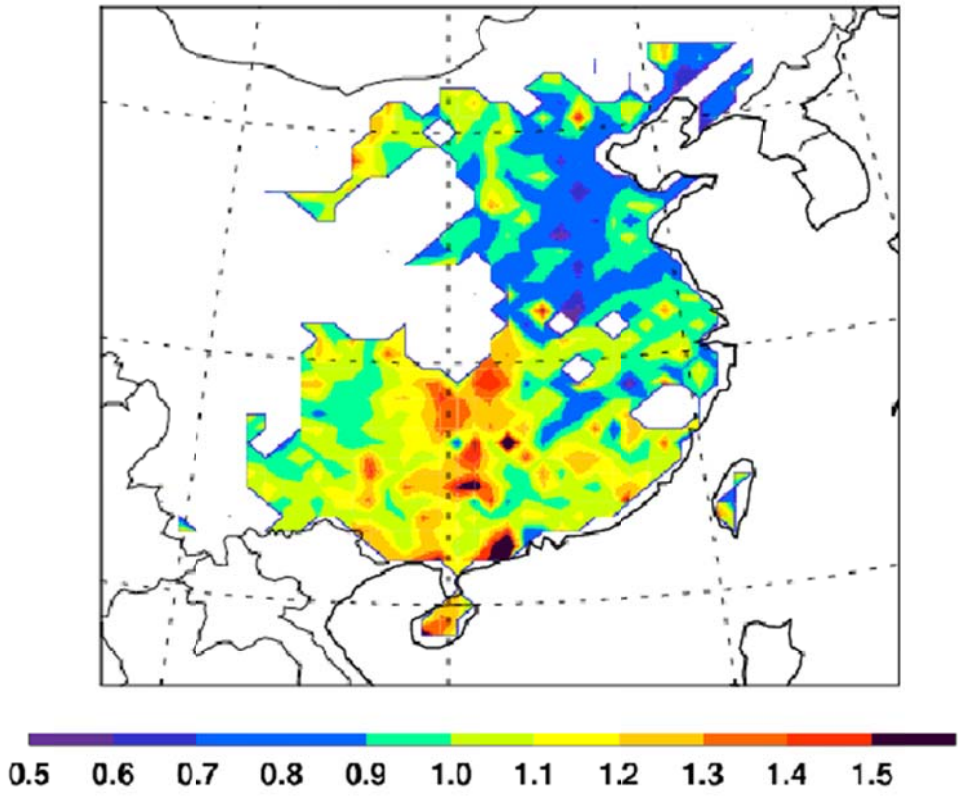

Figure C.1 Distribution of simulated annual mean β value over China for 2007.

C.3 Relative emission and VCD trend estimates in this work

In the analysis of regional NO_x emission and VCD trends, we define 4 regions: Northeast China (NEC), North China Plain (NCP), Yangtze River Delta (YRD) and Pearl River Delta (PRD). Figure S2 shows the regions and compound tropospheric VCD trend distibution.

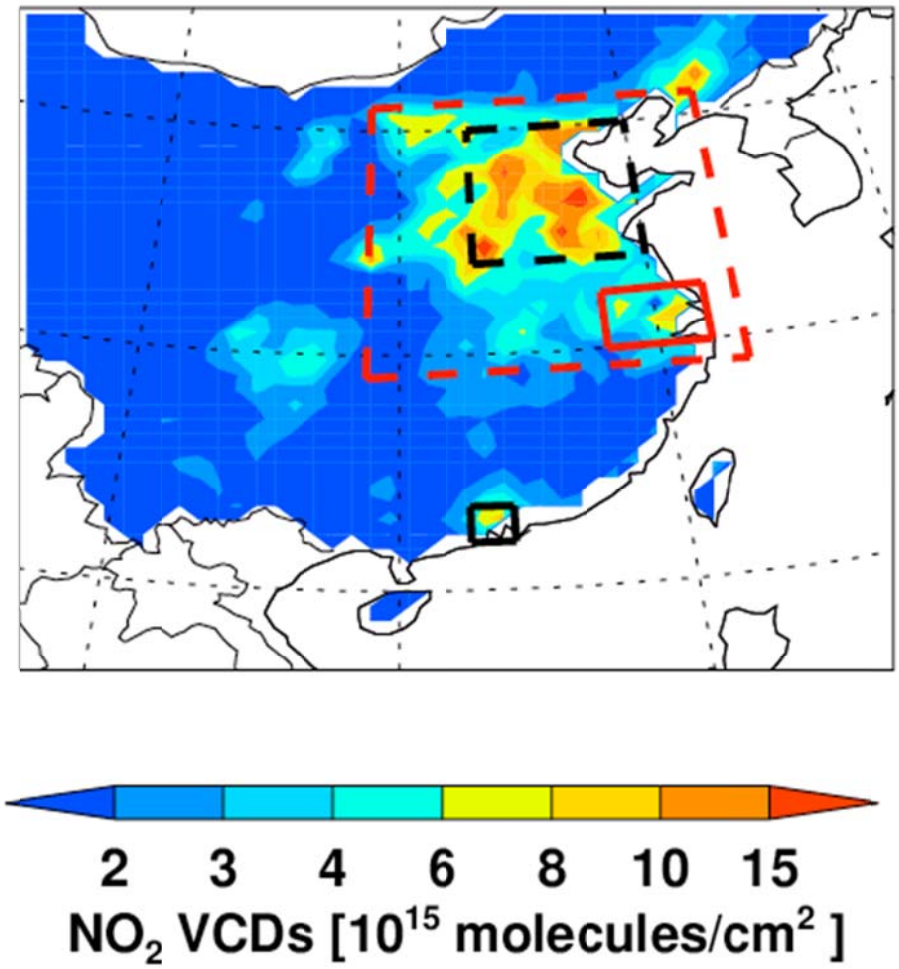

Figure C.2 The locations of NCP (34°-40° N and 113°-120° E), YRD (30°-32.5° N and 118°-122° E) and PRD (22°-23.5° and 112.5°-114° E) are indicated by the black dashed, red solid, and black solid boxes, respectively. NEC (29°-41° N and 108.75°-123.25° E), which includes NCP and YRD is shown by red dashed box.

The seasonal variation of NO_x emission trend is examined by month and VCDs in Figure C.3. While the emission trend is mostly positive generally in a range of 3-5% yr^{-1}, we also find negative emission trend down to -7% yr^{-1} in warm season for high NO_2 VCD regions, indicating potentially significant seasonal variation of NO_x emission trend in high emission regions.

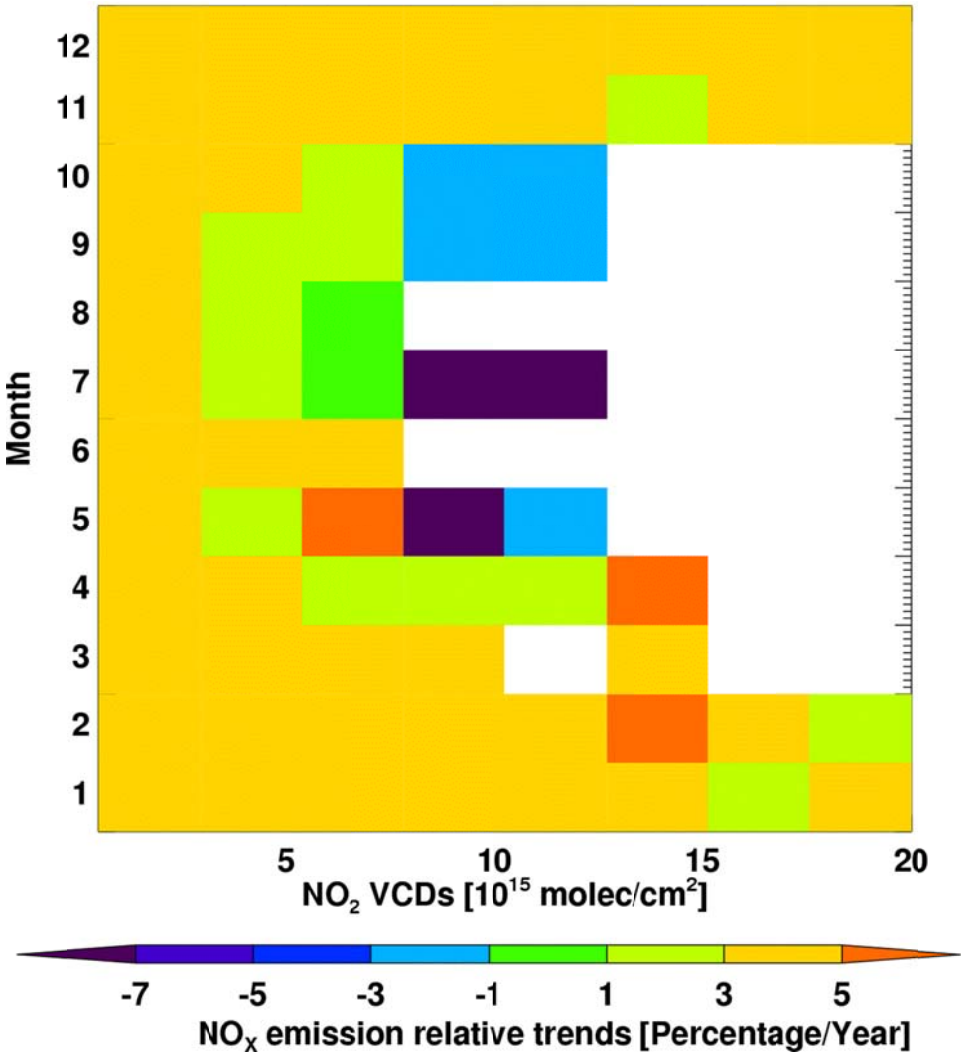

Figure C.3 Relative monthly NO_x emission trend over China as functions of month and NO_2 VCDs during 2005-2010. Emission trends are binned by month and with a tropospheric NO_2 VCD interval of 2.5×10^{15} molec/cm^2.

Compound annual growth rate is calculated and used in this work. Many previous studies computed linearized growth rate, which is normalized by the emission rate in the first year or an average over the study period. We show in Table C.2 a comparison of compound emission growth rate to that linearized to the first year emission. The linear result tends to overestimate the growth rate if emission increases and underestimate the reduction rate if emission decreases.

Table C.2 Compound and linearized NO_x emission trends over different regions in China during 2005-2010

Region	Compound rate (% yr^{-1})	Linear rate (% yr^{-1})
China	4.01±1.39	4.35±1.42
NEC	4.55±1.36	4.98±1.39
NCP	4.76±1.61	5.24±1.63
YRD	3.11±0.98	3.31±1.02
PRD	-4.39±1.81	-4.02±1.87

Table C.3 shows the regional-averaged compound NO_2 VCD trends. Compared to emission trends in Table C.2, the magnitudes of VCD trends are larger reflecting average β values of <1 in high NO_x emission regions. Also listed in the table are the trends of TEMIS DOMINOv1.02 and DOMINOv2 tropospheric VCD products over the perspective regions. The DOMINO product specification document (http://temis.nl/docs/OMI_NO2_HE5_2.0_2011.pdf) indicates that the VCD difference between two versions could come from updated air mass factor (AMF) based on a priori profiles by the TM4 model. However, no information was given in that document on potential impacts of TM4 profile changes on trend analysis.

Table C.3 Comparison among the annual trends of NO_2 VCDs (in % yr^{-1}) in this study, DOMINOv1.02 and DOMINOv2 OMI products during 2005~2010. Data between Aug. 2008 and Jul. 2009 are excluded. Note that trends are based on least-squares linear regression.

Region	NO_2 VCDs in this study	TEMIS DOMINOv1.02	TEMIS DOMINOv2
China	5.30±1.61	3.55±1.32	6.26±1.87
NEC	5.49±1.72	4.36±1.83	8.73±2.58
NCP	5.22±1.58	4.03±1.71	8.99±2.89
YRD	3.84±1.12	3.18±1.02	6.65±1.91
PRD	-6.71±1.95	-7.94±2.17	-4.80±1.53

APPENDIX D

AUXILIARY MATERIALS FOR CHAPTER 5

D.1 Assessment of NO_x concentration and O_3 vertical profile

Due to the lack of NO_x measurement during PASE, O_3 sensitivity on NO_x mixing ratio is tested in order to get suitable NO_x level for advanced HO_x simulations. A typical simulated O_3 vertical profile is compared with O_3 measurements in Figure D.1. The O_3 mixing ratio is sensitive to NO_x concentration, which increases as NO_x concentration increases, and the simulated O_3 matches observed O_3 when NO_x is constrained as 5 pptv. Because 5 pptv NO_x is also within the measurements during PEM- Tropics A and B which were also at similar tropical Pacific Ocean regions, we constrain 5 pptv NO_x in advanced HO_x simulations.

The impacts of vertical mixing process on O_3 vertical distribution are also tested. As Figure D.1 right plot showing, the NO_x mixing ratio do not have much impacts on model simulation of OH. Although HO_2 concentration slightly increases while NO_x increases, HO_2/OH do not have significant change regarding NO_x level.

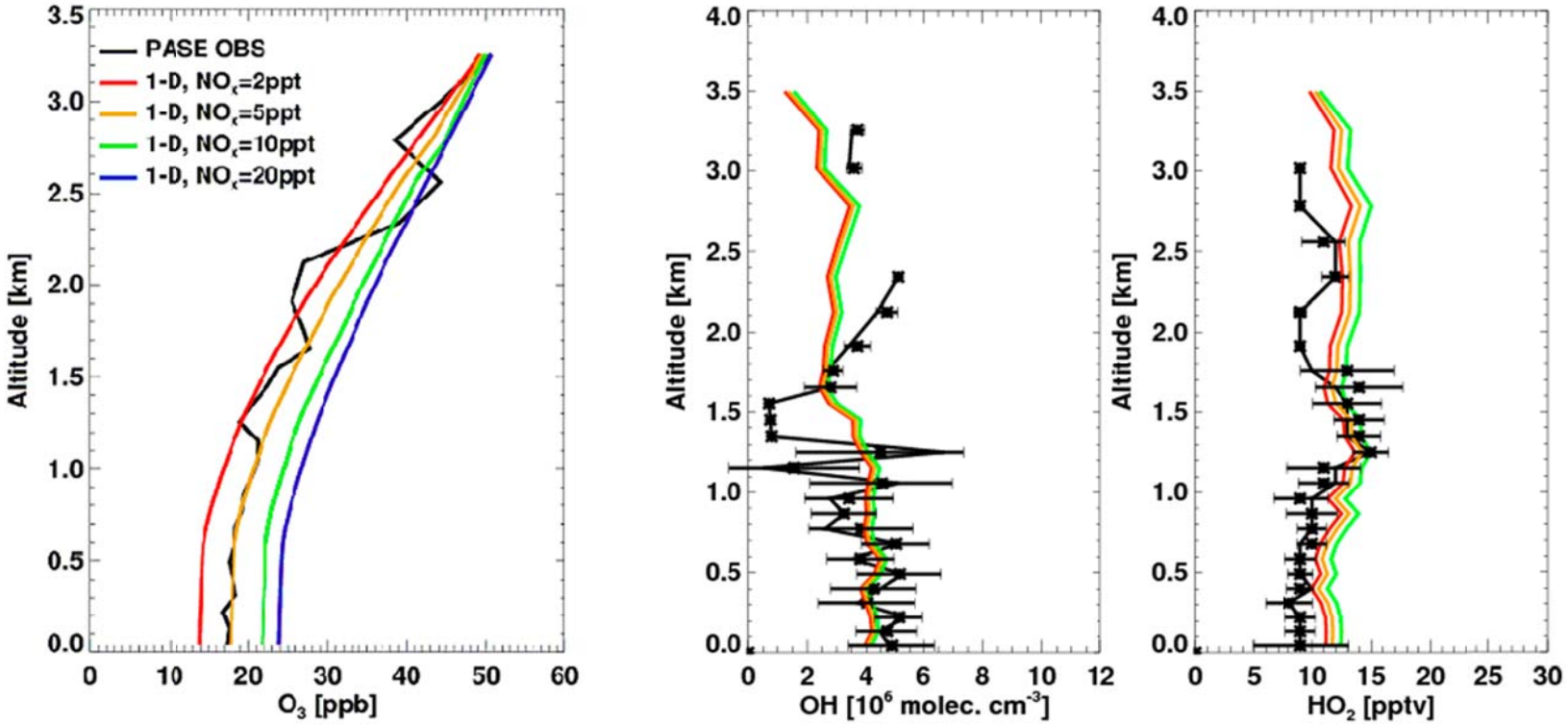

Figure D.1 Sensitivity of ozone on NO_x mixing ratio during normal flights (left). The sensitivity of OH (middle) and HO_2 (right) on NO_x mixing ratio during RF14.

D.2 OH production and loss

According our model simulation results, because of the high humidity and strong radiation over the tropical Pacific during summer, the production of OH is dominated by the reaction of $O(^1D)$ with H_2O, which contributes 39.7% to total OH production and over 50% of OH production under boundary layer. The photolysis of H_2O_2 and CH_3OOH contribute 26.4% and 8.6% to total OH production, respectively, while reactions of HO_2 with O_3 and NO contribute 19.3% and 2.2%, respectively (Figure D.2). Two of the most important sinks of OH are reactions of OH with CO and CH_4, which contribute 47.1% and 31.2% of OH loss, respectively. Reactions of OH with H_2O_2, VOCs, O_3 and HO_2, on the other hand, contribute 7.8%, 6.7%, 4.7% and 2.4%, respectively.

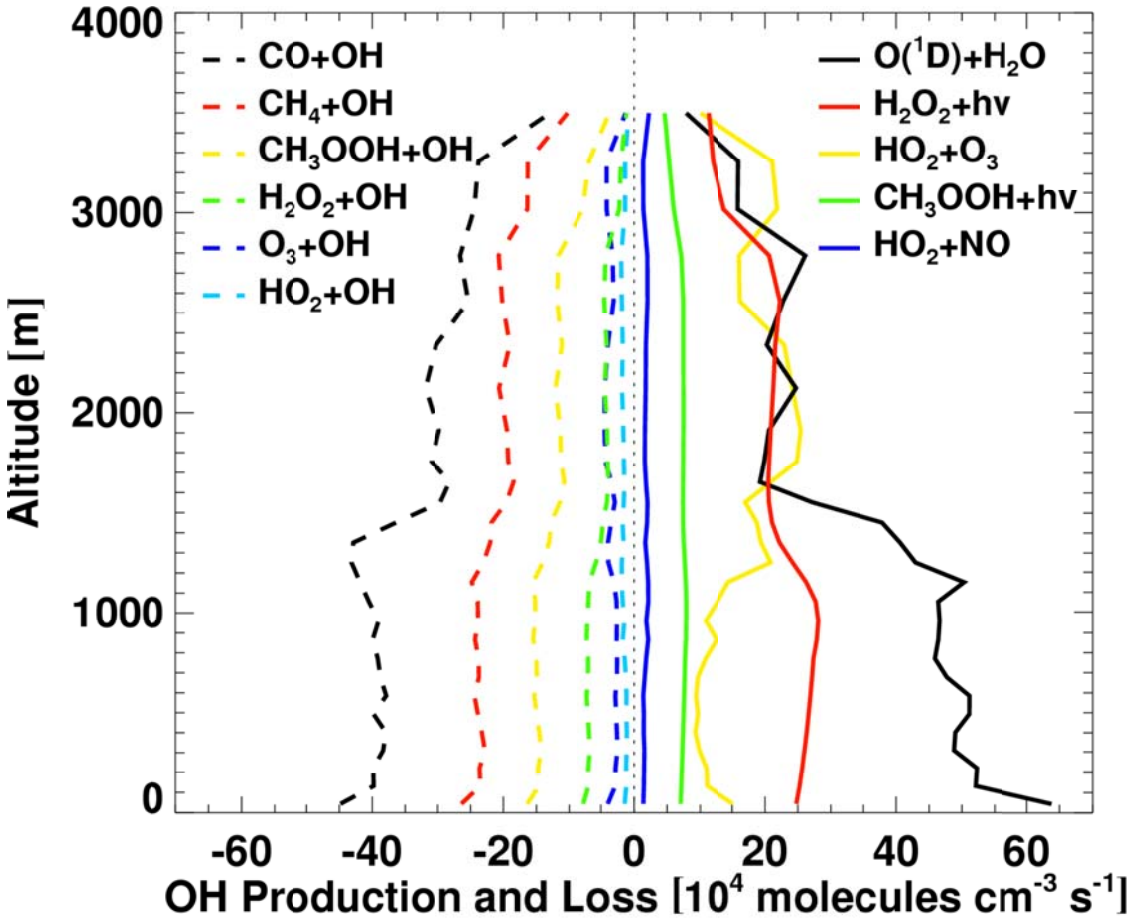

Figure D.2 OH production and loss during normal flights. Left panel shows OH loses in dash lines, and right panel shows OH productions in solid lines.

REFERENCES

Arnold, S. R., et al. (2009), Evaluation of the global oceanic isoprene source and its impacts on marine organic carbon aerosol, Atmospheric Chemistry and Physics, 9(4), 1253-1262.

Beirle, S., U. Platt, M. Wenig, and T. Wagner (2003), Weekly cycle of NO_2 by GOME measurements: a signature of anthropogenic sources, *Atmospheric Chemistry and Physics*, *3*, 2225-2232.

Bey, I., D. J. Jacob, R. M. Yantosca, J. A. Logan, B. D. Field, A. M. Fiore, Q. B. Li, H. G. Y. Liu, L. J. Mickley, and M. G. Schultz (2001), Global modeling of tropospheric chemistry with assimilated meteorology: Model description and evaluation, *Journal of Geophysical Research-Atmospheres*, *106*(D19), 23073-23095.

Boersma, K. F., H. J. Eskes, and E. J. Brinksma (2004), Error analysis for tropospheric NO_2 retrieval from space, *Journal of Geophysical Research-Atmospheres*, *109*(D4), D04311, doi:10.1029/2003JD003962.

Boersma, K. F., D. J. Jacob, M. Trainic, Y. Rudich, I. DeSmedt, R. Dirksen, and H. J. Eskes (2009), Validation of urban NO_2 concentrations and their diurnal and seasonal variations observed from the SCIAMACHY and OMI sensors using in situ surface measurements in Israeli cities, *Atmos. Chem. Phys.*, *9*(12), 3867-3879.

Boersma, K. F., et al. (2007), Near-real time retrieval of tropospheric NO_2 from OMI, *Atmospheric Chemistry and Physics*, *7*(8), 2103-2118.

Boersma, K. F., et al. (2011), An improved tropospheric NO_2 column retrieval algorithm for the Ozone Monitoring Instrument, *Atmospheric Measurement Techniques*, *4*(9), 1905-1928.

Bonsang, B., C. Polle, and G. Lambert (1992), EVIDENCE FOR MARINE PRODUCTION OF ISOPRENE, *Geophysical Research Letters*, *19*(11), 1129-1132.

Broadgate, W. J., G. Malin, F. C. Kupper, A. Thompson, and P. S. Liss (2004), Isoprene and other non-methane hydrocarbons from seaweeds: a source of reactive hydrocarbons to the atmosphere, *Marine Chemistry*, *88*(1-2), 61-73.

Brune, W. H., et al. (1998), Airborne in-situ OH and HO_2 observations in the cloud-free troposphere and lower stratosphere during SUCCESS, *Geophysical Research Letters*, *25*(10), 1701-1704.

Buckley, S. M., and M. J. Mitchell (2011), Improvements in Urban Air Quality: Case Studies from New York State, USA, *Water Air Soil Pollut.*, *214*(1-4), 93-106.

CAEPI (2008), China Development Report on Desulphurization and Denitration Industries in Power Plants in 2007, *China Environmental Protection Industry*, *2008*(6).

CAEPI (2011), China Development Report on Desulfurization and Denitration Industry of Power Plant in 2010, *China Environmental Protection Industry*, *2011*(7).

Carslaw, D. C. (2005), Evidence of an increasing NO_2/NO_x emissions ratio from road traffic emissions, *Atmospheric Environment*, *39*(26), 4793-4802.

Cattani, G., A. D. di Bucchianico, D. Dina, M. Inglessis, C. Notaro, G. Settimo, G. Viviano, and A. Marconi (2010), Evaluation of the temporal variation of air quality in Rome, Italy from 1999 to 2008, *Ann. Ist. Super. Sanita*, *46*(3), 242-253.

Choi, Y., H. Kim, D. Tong, and P. Lee (2012), Summertime weekly cycles of observed and modeled NO_x and O_3 concentrations as a function of satellite-derived ozone production sensitivity and land use types over the Continental United States, *Atmospheric Chemistry and Physics*, *12*(14), 6291-6307.

Choi, Y., Y. H. Wang, T. Zeng, R. V. Martin, T. P. Kurosu, and K. Chance (2005), Evidence of lightning NO_x and convective transport of pollutants in satellite observations over North America, *Geophysical Research Letters*, *32*(2), doi:10.1029/2004GL021436.

Choi, Y., Y. Wang, T. Zeng, D. Cunnold, E. S. Yang, R. Martin, K. Chance, V. Thouret, and E. Edgerton (2008a), Springtime transitions of NO_2, CO, and O_3 over North America: Model evaluation and analysis, *Journal of Geophysical Research-Atmospheres*, *113*(D20), doi:10.1029/2007JD009632.

Choi, Y., Y. H. Wang, Q. Yang, D. Cunnold, T. Zeng, C. Shim, M. Luo, A. Eldering, E. Bucsela, and J. Gleason (2008b), Spring to summer northward migration of high O_3 over the western North Atlantic, *Geophysical Research Letters*, *35*, L04818, doi:10.1029/2007GL032276.

Conley, S. A., I. Faloona, G. H. Miller, D. H. Lenschow, B. Blomquist, and A. Bandy (2009), Closing the dimethyl sulfide budget in the tropical marine boundary layer during the Pacific Atmospheric Sulfur Experiment, *Atmospheric Chemistry and Physics*, *9*(22), 8745-8756.

Cooper, W. J., J. K. Moegling, R. J. Kieber, and J. J. Kiddle (2000), A chemiluminescence method for the analysis of H_2O_2 in natural waters, *Marine Chemistry*, *70*(1-3), 191-200.

Davis, D., et al. (2001), Marine latitude/altitude OH distributions: Comparison of Pacific Ocean observations with models, *Journal of Geophysical Research-Atmospheres*, *106*(D23), 32691-32707.

Doherty, R. M., D. S. Stevenson, W. J. Collins, and M. G. Sanderson (2005), Influence of convective transport on tropospheric ozone and its precursors in a chemistry-climate model, *Atmospheric Chemistry and Physics*, *5*, 3205-3218.

Dong Huang, F. Z., Sheng Wang (2012), Study on the Flue Gas Denitrification Cost Estimation of Coal-fired Power Plant During the "Twelfth Five-Year Plan" Period of China, *Energy Technology and Economics*, *24*(4).

Dorf, M., A. Butz, C. Camy-Peyret, M. P. Chipperfield, L. Kritten, and K. Pfeilsticker (2008), Bromine in the tropical troposphere and stratosphere as derived from balloon-borne BrO observations, *Atmospheric Chemistry and Physics*, *8*(23), 7265-7271.

Faloona, I., S. A. Conley, B. Blomquist, A. D. Clarke, V. Kapustin, S. Howell, D. H. Lenschow, and A. R. Bandy (2009), Sulfur dioxide in the tropical marine boundary layer: dry deposition and heterogeneous oxidation observed during the Pacific Atmospheric Sulfur Experiment, *Journal of Atmospheric Chemistry*, *63*(1), 13-32.

Ferraro, G., and M. Brans (2012), Trade-offs between environmental protection and economic development in China's fisheries policy: A political analysis on the adoption and implementation of the Fisheries Law 2000, *Nat. Resour. Forum*, *36*(1), 38-49.

Folkins, I., P. Bernath, C. Boone, L. J. Donner, A. Eldering, G. Lesins, R. V. Martin, B. M. Sinnhuber, and K. Walker (2006), Testing convective parameterizations with tropical measurements of HNO_3, CO, H_2O, and O_3: Implications for the water vapor budget, *Journal of Geophysical Research-Atmospheres*, *111*(D23).

Fu, T. M., D. J. Jacob, F. Wittrock, J. P. Burrows, M. Vrekoussis, and D. K. Henze (2008), Global budgets of atmospheric glyoxal and methylglyoxal, and implications for formation of secondary organic aerosols, *Journal of Geophysical Research-Atmospheres*, *113*(D15).

Gantt, B., N. Meskhidze, and D. Kamykowski (2009), A new physically-based quantification of marine isoprene and primary organic aerosol emissions, *Atmospheric Chemistry and Physics*, *9*(14), 4915-4927.

GEPA (2008), Report on the Environmental Quality in Guangzhou 2007, Guangzhou Environmental Protection Angency, http://www.gzepb.gov.cn/root43/gov/200810/t20081020_4192.htm.

Ghude, S. D., R. J. Van der A, G. Beig, S. Fadnavis, and S. D. Polade (2009), Satellite derived trends in NO_2 over the major global hotspot regions during the past decade and their inter-comparison, *Environ. Pollut.*, *157*(6), 1873-1878.

Grant, A., E. L. Yates, P. G. Simmonds, R. G. Derwent, A. J. Manning, D. Young, D. E. Shallcross, and S. O'Doherty (2011), A five year record of high-frequency in situ measurements of non-methane hydrocarbons at Mace Head, Ireland, *Atmospheric Measurement Techniques*, *4*(5), 955-964.

Gray, B. A., Y. H. Wang, D. S. Gu, A. Bandy, L. Mauldin, A. Clarke, B. Alexander, and D. D. Davis (2011), Sources, transport, and sinks of SO_2 over the equatorial Pacific during the Pacific Atmospheric Sulfur Experiment, *Journal of Atmospheric Chemistry*, *68*(1), 27-53.

Gu, D., Y. Wang, C. Smeltzer, and Z. Liu (2013), Reduction in NO_x Emission Trends over China: Regional and Seasonal Variations, *Environ. Sci. Technol.*, *47*(22), 12912-12919.

Hains, J. C., et al. (2010), Testing and improving OMI DOMINO tropospheric NO_2 using observations from the DANDELIONS and INTEX-B validation campaigns, *Journal of Geophysical Research: Atmospheres*, *115*(D5), D05301, doi: 10.1029/2009JD012399.

Han, K. M., C. H. Song, H. J. Ahn, R. S. Park, J. H. Woo, C. K. Lee, A. Richter, J. P. Burrows, J. Y. Kim, and J. H. Hong (2009), Investigation of NO_x emissions and NO_x- related chemistry in East Asia using CMAQ-predicted and GOME-derived NO_2 columns, *Atmospheric Chemistry and Physics*, *9*(3), 1017-1036.

Hayn, M., S. Beirle, F. A. Hamprecht, U. Platt, B. H. Menze, and T. Wagner (2009), Analysing spatio-temporal patterns of the global NO_2-distribution retrieved from GOME satellite observations using a generalized additive model, *Atmospheric Chemistry and Physics*, *9*(17), 6459-6477.

He, Y., I. Uno, Z. Wang, T. Ohara, N. Sugirnoto, A. Shimizu, A. Richter, and J. P. Burrows (2007), Variations of the increasing trend of tropospheric NO_2 over central east China during the past decade, *Atmospheric Environment*, *41*(23), 4865-4876.

Heckel, A., S. W. Kim, G. J. Frost, A. Richter, M. Trainer, and J. P. Burrows (2011), Influence of low spatial resolution a priori data on tropospheric NO_2 satellite retrievals, *Atmospheric Measurement Techniques*, *4*(9), 1805-1820.

Hess, P. G. (2005), A comparison of two paradigms: The relative global roles of moist convective versus nonconvective transport, *Journal of Geophysical Research-Atmospheres*, *110*(D20).

Hilboll, A., A. Richter, and J. P. Burrows (2012), Long-term changes of tropospheric NO2 over megacities derived from multiple satellite instruments, *Atmos. Chem. Phys. Discuss.*, *12*(12), 31767-31828.

Huang, H., and Y. H. D. Wei (2011), SPATIAL-TEMPORAL PATTERNS AND DETERMINANTS OF FOREIGN DIRECT INVESTMENT IN CHINA, *Erdkunde*, *65*(1), 7-23.

Irie, H., K. F. Boersma, Y. Kanaya, H. Takashima, X. Pan, and Z. F. Wang (2012), Quantitative bias estimates for tropospheric NO_2 columns retrieved from SCIAMACHY, OMI, and GOME-2 using a common standard for East Asia, *Atmospheric Measurement Techniques*, *5*(10), 2403-2411.

Jacob, D. J., J. H. Crawford, M. M. Kleb, V. S. Connors, R. J. Bendura, J. L. Raper, G. W. Sachse, J. C. Gille, L. Emmons, and C. L. Heald (2003), Transport and Chemical Evolution over the Pacific (TRACE-P) aircraft mission: Design, execution, and first results, *Journal of Geophysical Research-Atmospheres*, *108*(D20), 1-19.

Jaegle, L., D. J. Jacob, W. H. Brune, and P. O. Wennberg (2001), Chemistry of HO_x radicals in the upper troposphere, *Atmospheric Environment*, *35*(3), 469-489.

Jaegle, L., L. Steinberger, R. V. Martin, and K. Chance (2005), Global partitioning of NOx sources using satellite observations: Relative roles of fossil fuel combustion, biomass burning and soil emissions, *Faraday Discussions*, *130*, 407-423.

Jing, P., D. Cunnold, Y. Choi, and Y. Wang (2006), Summertime tropospheric ozone columns from Aura OMI/MLS measurements versus regional model results over the United States, *Geophysical Research Letters*, *33*(17), L17817, doi:10.1029/2006GL026473.

Kain, J. S. (2004), The Kain-Fritsch convective parameterization: An update, *Journal of Applied Meteorology*, *43*(1), 170-181.

Kanaya, Y., R. Q. Cao, H. Akimoto, M. Fukuda, Y. Komazaki, Y. Yokouchi, M. Koike, H. Tanimoto, N. Takegawa, and Y. Kondo (2007), Urban photochemistry in central Tokyo: 1. Observed and modeled OH and HO_2 radical concentrations during the winter and summer of 2004, *Journal of Geophysical Research-Atmospheres*, *112*(D21), 20.

Kanaya, Y. G., R. Q. Cao, S. G. Kato, Y. K. Miyakawa, Y. Kajii, H. Tanimoto, Y. Yokouchi, M. Mochida, K. Kawamura, and H. Akimoto (2007), Chemistry of OH and HO_2 radicals observed at Rishiri Island, Japan, in September 2003: Missing daytime sink of HO_2 and positive nighttime correlations with monoterpenes, *Journal of Geophysical Research-Atmospheres*, *112*(D11), 17.

Kaynak, B., Y. Hu, R. V. Martin, C. E. Sioris, and A. G. Russell (2009), Comparison of weekly cycle of NO_2 satellite retrievals and NO_x emission inventories for the continental United States, *Journal of Geophysical Research-Atmospheres*, *114*.

Keene, W. C., et al. (2007), Chemical and physical characteristics of nascent aerosols produced by bursting bubbles at a model air-sea interface, *J. Geophys. Res.*, *112*(D21), D21202.

King, D. W., W. J. Cooper, S. A. Rusak, B. M. Peake, J. J. Kiddle, D. W. O'Sullivan, M. L. Melamed, C. R. Morgan, and S. M. Theberge (2007), Flow injection analysis of H_2O_2 in natural waters using acridinium ester chemiluminescence: Method development and optimization using a kinetic model, *Analytical Chemistry*, *79*(11), 4169-4176.

Kunhikrishnan, T., M. G. Lawrence, R. von Kuhlmann, A. Richter, A. Ladstatter-Weissenmayer, and J. P. Burrows (2004), Analysis of tropospheric NO_x over Asia using the model of atmospheric transport and chemistry (MATCH-MPIC) and GOME-satellite observations, *Atmospheric Environment*, *38*(4), 581-596.

Kurokawa, J., K. Yumimoto, I. Uno, and T. Ohara (2009), Adjoint inverse modeling of NO_x emissions over eastern China using satellite observations of NO_2 vertical column densities, *Atmospheric Environment*, *43*(11), 1878-1887.

Lamsal, L. N., R. V. Martin, A. van Donkelaar, M. Steinbacher, E. A. Celarier, E. Bucsela, E. J. Dunlea, and J. P. Pinto (2008), Ground-level nitrogen dioxide concentrations inferred from the satellite-borne Ozone Monitoring Instrument, *Journal of Geophysical Research-Atmospheres*, *113*(D16).

Lamsal, L. N., R. V. Martin, A. Padmanabhan, A. van Donkelaar, Q. Zhang, C. E. Sioris, K. Chance, T. P. Kurosu, and M. J. Newchurch (2011), Application of satellite observations for timely updates to global anthropogenic NO_x emission inventories, *Geophysical Research Letters*, *38*(5), L05810.

Lanzendorf, E. J., T. F. Hanisco, P. O. Wennberg, R. C. Cohen, R. M. Stimpfle, and J. G. Anderson (2001a), Comparing atmospheric $[HO_2]/[OH]$ to modeled $[HO_2]/[OH]$: Identifying discrepancies with reaction rates, *Geophysical Research Letters*, *28*(6), 967-970.

Lanzendorf, E. J., T. F. Hanisco, P. O. Wennberg, R. C. Cohen, R. M. Stimpfle, J. G. Anderson, R. S. Gao, J. J. Margitan, and T. P. Bui (2001b), Establishing the dependence of [HO2]/[OH] on temperature, halogen loading, O_3, and NO_x based on in situ measurements from the NASA ER-2, *Journal of Physical Chemistry A*, *105*(9), 1535-1542.

Lee, J. D., et al. (2010), Reactive Halogens in the Marine Boundary Layer (RHaMBLe): the tropical North Atlantic experiments, *Atmospheric Chemistry and Physics*, *10*(3), 1031-1055.

Lee, M., D. O'Sullivan, K. Noone, and B. Heikes (1995), HPLC method for the determination of H_2O_2 , C1 and C2 hydroperoxides in the atmosphere, *J. Atmos. Oceanic Tech.*, *12*.

Lei, X. M. (2005), *Market design and operational experience with generation and transmission of the Three-Gorges hydroelectric power station*, 31-35 pp., Ieee, New York.

Levelt, P. F., E. Hilsenrath, G. W. Leppelmeier, G. H. J. van den Oord, P. K. Bhartia, J. Tamminen, J. F. de Haan, and J. P. Veefkind (2006), Science objectives of the Ozone Monitoring Instrument, *Ieee Transactions on Geoscience and Remote* Sensing, 44(5), 1199-1208.

Lerot, C., T. Stavrakou, I. De Smedt, J. F. Müller, and M. Van Roozendael (2010), Glyoxal vertical columns from GOME-2 backscattered light measurements and comparisons with a global model, Atmos. Chem. Phys., 10(24), 12059-12072.

Li, C., Q. Zhang, N. A. Krotkov, D. G. Streets, K. B. He, S. C. Tsay, and J. F. Gleason (2010), Recent large reduction in sulfur dioxide emissions from Chinese power plants observed by the Ozone Monitoring Instrument, *Geophysical Research Letters*, *37*.

Liang, Z. Y., X. Q. Ma, H. Lin, and Y. T. Tang (2011), The energy consumption and environmental impacts of SCR technology in China, *Appl. Energy*, *88*(4), 1120-1129.

Lin, J., C. P. Nielsen, Y. Zhao, Y. Lei, Y. Liu, and M. B. McElroy (2010a), Recent Changes in Particulate Air Pollution over China Observed from Space and the Ground: Effectiveness of Emission Control, *Environ. Sci. Technol.*, *44*(20), 7771-7776.

Lin, J. T., M. B. McElroy, and K. F. Boersma (2010b), Constraint of anthropogenic NO_x emissions in China from different sectors: a new methodology using multiple satellite retrievals, *Atmospheric Chemistry and Physics*, *10*(1), 63-78.

Lin, J. T., Z. Liu, Q. Zhang, H. Liu, J. Mao, and G. Zhuang (2012), Modeling uncertainties for tropospheric nitrogen dioxide columns affecting satellite-based inverse modeling of nitrogen oxides emissions, *Atmospheric Chemistry and Physics*, *12*(24), 12255-12275.

Liu, Z., et al. (2012a), Exploring the missing source of glyoxal (CHOCHO) over China, *Geophysical Research Letters*, *39*, L10812, doi:10.1029/2012GL051645.

Liu, Z., et al. (2010), Evidence of Reactive Aromatics As a Major Source of Peroxy Acetyl Nitrate over China, *Environ. Sci. Technol.*, *44*(18), 7017-7022.

Liu, Z., et al. (2012b), Summertime photochemistry during CAREBeijing-2007: RO_x budgets and O_3 formation, *Atmospheric Chemistry and Physics*, *12*(16), 7737-7752.

Lu, Z., and D. G. Streets (2012), Increase in NO_x Emissions from Indian Thermal Power Plants during 1996–2010: Unit-Based Inventories and Multisatellite Observations, *Environ. Sci. Technol.*

Ma, J. Z., A. Richter, J. P. Burrows, H. Nuss, and J. A. van Aardenne (2006), Comparison of model-simulated tropospheric NO_2 over China with GOME-satellite data, *Atmospheric Environment*, *40*(4), 593-604.

MCC (2011), Brief Statistics on China's Import & Export, MINISTRY OF COMMERCE, CHINA, http://english.mofcom.gov.cn/statistic/statistic.html.

Mao, J., et al. (2009), Airborne measurement of OH reactivity during INTEX-B, *Atmospheric Chemistry and Physics*, *9*(1), 163-173.

Marandino, C. A., W. J. De Bruyn, S. D. Miller, M. J. Prather, and E. S. Saltzman (2006), Oceanic uptake and the global atmospheric acetone budget (vol 32, art no L15806, 2006), *Geophysical Research Letters*, *33*(24).

Martin, R. V., D. J. Jacob, K. Chance, T. P. Kurosu, P. I. Palmer, and M. J. Evans (2003), Global inventory of nitrogen oxide emissions constrained by space-based observations of NO_2 columns, *Journal of Geophysical Research-Atmospheres*, *108*(D17), 4537, doi:10.1029/2003JD003453.

Matsunaga, S., M. Mochida, T. Saito, and K. Kawamura (2002), In situ measurement of isoprene in the marine air and surface seawater from the western North Pacific, *Atmospheric Environment*, *36*(39-40), 6051-6057.

Mauldin, R. L., E. Kosciuch, B. Henry, F. L. Eisele, R. Shetter, B. Lefer, G. Chen, D. Davis, G. Huey, and D. Tanner (2004), Measurements of OH, HO_2+RO_2, H_2SO_4, and MSA at the south pole during ISCAT 2000, *Atmospheric Environment*, *38*(32), 5423-5437.

McCormack, G. (2001), Water margins - Competing paradigms in China, *Crit. Asian Stud*, *33*(1), 5-30.

Melamed, M. L., N. P. Bizier, S. B. Lovitz, S. M. Theberge, and D. W. King (2000), Investigation of the chemiluminescence reaction dynamics of H_2O_2 and acridinium esters for optimization of fia for natural H_2O_2 samples, *Abstracts of Papers of the American Chemical Society*, *219*, 224-CHED.

Miyazaki, K., H. J. Eskes, and K. Sudo (2012), Global NO_x emission estimates derived from an assimilation of OMI tropospheric NO_2 columns, *Atmospheric Chemistry and Physics*, *12*(5), 2263-2288.

Moore, R. M., and L. Wang (2006), The influence of iron fertilization on the fluxes of methyl halides and isoprene from ocean to atmosphere in the SERIES experiment, *Deep-Sea Research Part Ii-Topical Studies in Oceanography*, *53*(20-22), 2398-2409.

Myriokefalitakis, S., M. Vrekoussis, K. Tsigaridis, F. Wittrock, A. Richter, C. Bruhl, R. Volkamer, J. P. Burrows, and M. Kanakidou (2008), The influence of natural and anthropogenic secondary sources on the glyoxal global distribution, *Atmospheric Chemistry and Physics*, *8*(16), 4965-4981.

Ohara, T., H. Akimoto, J. Kurokawa, N. Horii, K. Yamaji, X. Yan, and T. Hayasaka (2007), An Asian emission inventory of anthropogenic emission sources for the period 1980-2020, *Atmospheric Chemistry and Physics*, *7*(16), 4419-4444.

Osullivan, D. W., M. Y. Lee, B. C. Noone, and B. G. Heikes (1996), Henry's law constant determinations for hydrogen peroxide, methyl hydroperoxide, hydroxymethyl hydroperoxide, ethyl hydroperoxide, and peroxyacetic acid, *Journal of Physical Chemistry*, *100*(8), 3241-3247.

Read, K. A., et al. (2008), Extensive halogen-mediated ozone destruction over the tropical Atlantic Ocean, *Nature*, *453*(7199), 1232-1235.

Ren, X. R., et al. (2008), HO_x chemistry during INTEX-A 2004: Observation, model calculation, and comparison with previous studies, *Journal of Geophysical Research-Atmospheres*, *113*(D5).

Richter, A., J. P. Burrows, H. Nuss, C. Granier, and U. Niemeier (2005), Increase in tropospheric nitrogen dioxide over China observed from space, *Nature*, 437(7055), 129-132.

Richter, A., V. Eyring, J. P. Burrows, H. Bovensmann, A. Lauer, B. Sierk, and P. J. Crutzen (2004), Satellite measurements of NO_2 from international shipping emissions, Geophysical Research Letters, 31(23), L23110, doi:10.1029/ 2004GL020822.

Russell, A. R., L. C. Valin, and R. C. Cohen (2012), Trends in OMI NO_2 observations over the United States: effects of emission control technology and the economic recession, *Atmospheric Chemistry and Physics*, *12*(24), 12197-12209.

Saikawa, E., J. Kurokawa, M. Takigawa, J. Borken-Kleefeld, D. L. Mauzerall, L. W. Horowitz, and T. Ohara (2011), The impact of China's vehicle emissions on regional air quality in 2000 and 2020: a scenario analysis, *Atmospheric Chemistry and Physics*, *11*(18), 9465-9484.

Saiz-Lopez, A., et al. (2012), Estimating the climate significance of halogen-driven ozone loss in the tropical marine troposphere, *Atmospheric Chemistry and Physics*, *12*(9), 3939-3949.

Sander, S. P., Abbate, J., Barker, J. R., Burkholder, J. B., Friedl, R. R., Golden, D. M., Huie, R. E., Kolb, C. E., Kurylo, M. J., Moortgat, G. K., Orkin, V. L., and Wine, P. H. (2011), Chemical Kinetics and Photochemical Data for Use in Atmospheric Studies, Evaluation No 17. J. P., 10-6,, edited, JPL, Pasadena, CA.

Sandu, A., and R. Sander (2006), Technical note: Simulating chemical systems in Fortran90 and Matlab with the Kinetic PreProcessor KPP-2.1, *Atmospheric Chemistry and Physics*, *6*, 187-195.

Schneider, P., and R. J. van der A (2012), A global single-sensor analysis of 2002-2011 tropospheric nitrogen dioxide trends observed from space, *J. Geophys. Res.*, *117*(D16), D16309.

SERCC (2011), Report on energy saving and emission reduction of electric power Industry during 2010 and the 11th Five-Year Plan, http://www.serc.gov.cn/jggg/201208/W020111026348300590384.doc.

Shaw, S. L., S. W. Chisholm, and R. G. Prinn (2003), Isoprene production by Prochlorococcus, a marine cyanobacterium, and other phytoplankton, *Marine Chemistry*, *80*(4), 227-245.

Shen, M. D., K. L. Lu, and N. Soc Francaise Energie (1996), Development of nuclear power in Guangdong Province, People's Republic of China, *Topnux '96: Economic Nuclear Power for the 21st Century, Vols 1 and 2: Economic Nuclear Power for the 21st Century: Towards the New Generation of Reactors*, 67-78.

Shi, C. N., H. J. S. Fernando, Z. F. Wang, X. Q. An, and Q. Z. Wu (2008), Tropospheric NO_2 columns over East Central China: Comparisons between SCIAMACHY measurements and nested CMAQ simulations, *Atmospheric Environment*, *42*(30), 7165-7173.

Shon, Z. H., K. H. Kim, and S. K. Song (2011), Long-term trend in NO_2 and NO_x levels and their emission ratio in relation to road traffic activities in East Asia, *Atmospheric Environment*, *45*(18), 3120-3131.

Sicard, P., L. Dalstein-Richier, and N. Vas (2011), Annual and seasonal trends of ambient ozone concentration and its impact on forest vegetation in Mercantour National Park (South-eastern France) over the 2000-2008 period, *Environ. Pollut.*, *159*(2), 351-362.

Sicard, P., A. Mangin, P. Hebel, and P. Mallea (2010), Detection and estimation trends linked to air quality and mortality on French Riviera over the 1990-2005 period, *Sci. Total Environ.*, *408*(8), 1943-1950.

Singh, H. B., et al. (2004), Analysis of the atmospheric distribution, sources, and sinks of oxygenated volatile organic chemicals based on measurements over the Pacific during TRACE-P, *Journal of Geophysical Research-Atmospheres*, *109*(D15), 20.

Sinreich, R., S. Coburn, B. Dix, and R. Volkamer (2010), Ship-based detection of glyoxal over the remote tropical Pacific Ocean, *Atmospheric Chemistry and Physics*, *10*(23), 11359-11371.

Statistics, C. N. B. o. (2010), *China Statistical Yearbook 2010*, China Statistics Press.

Stavrakou, T., J. F. Muller, K. F. Boersma, I. De Smedt, and R. J. van der A (2008), Assessing the distribution and growth rates of NO_x emission sources by inverting a 10-year record of NO_2 satellite columns, *Geophysical Research Letters*, *35*(10), doi: 10.1029/2008GL033521.

Stevens, P. S., et al. (1997), HO_2/OH and RO_2/HO_2 ratios during the Tropospheric OH Photochemistry Experiment: Measurement and theory, Journal of Geophysical Research-Atmospheres, 102(D5), 6379-6391.

Streets, D. G., et al. (2003), An inventory of gaseous and primary aerosol emissions in Asia in the year 2000, Journal of Geophysical Research-Atmospheres, 108(D21), 8809, doi: 10.1029/2002JD003093.

Tang, S. Y., C. W. H. Lo, and G. E. Fryxell (2010), Governance reform, external support, and environmental regulation enforcement in rural China: The case of Guangdong province, *J. Environ. Manage.*, *91*(10), 2008-2018.

Uno, I., et al. (2007), Systematic analysis of interannual and seasonal variations of model-simulated tropospheric NO_2 in Asia and comparison with GOME-satellite data, *Atmospheric Chemistry and Physics*, *7*(6), 1671-1681.

van der A, R. J., D. Peters, H. Eskes, K. F. Boersma, M. Van Roozendael, I. De Smedt, and H. M. Kelder (2006), Detection of the trend and seasonal variation in tropospheric NO_2 over China, *Journal of Geophysical Research-Atmospheres*, *111*(D12), D12317, doi:10.1029/2005JD006594.

van der A, R. J., H. J. Eskes, K. F. Boersma, T. P. C. van Noije, M. Van Roozendael, I. De Smedt, D. Peters, and E. W. Meijer (2008), Trends, seasonal variability and dominant NO_x source derived from a ten year record of NO_2 measured from space, *Journal of Geophysical Research-Atmospheres*, *113*(D4), 12.

Vinken, G. C. M., K. F. Boersma, A. van Donkelaar, and L. Zhang (2014), Constraints on ship NO_x emissions in Europe using GEOS-Chem and OMI satellite NO_2 observations, *Atmos. Chem. Phys.*, *14*(3), 1353-1369.

Vrekoussis, M., F. Wittrock, A. Richter, and J. P. Burrows (2009), Temporal and spatial variability of glyoxal as observed from space, *Atmospheric Chemistry and Physics*, *9*(13), 4485-4504.

Walker, T. W., et al. (2010), Trans-Pacific transport of reactive nitrogen and ozone to Canada during spring, *Atmospheric Chemistry and Physics*, *10*(17), 8353-8372.

Wang, H. K., L. X. Fu, Y. Zhou, X. Du, and W. H. Ge (2010), Trends in vehicular emissions in China's mega cities from 1995 to 2005, *Environ. Pollut.*, *158*(2), 394-400.

Wang, S., and J. Hao (2012), Air quality management in China: Issues, challenges, and options, *Journal of Environmental Sciences*, *24*(1), 2-13.

Wang, S. W., Q. Zhang, D. G. Streets, K. B. He, R. V. Martin, L. N. Lamsal, D. Chen, Y. Lei, and Z. Lu (2012), Growth in NO_x emissions from power plants in China: bottom-up estimates and satellite observations, *Atmospheric Chemistry and Physics*, *12*(10), 4429-4447.

Wang, Y. (2000), Global Tropospheric OH: Observational Constraints and Model Simulations, *IGBP Newsletter*, *43*.

Wang, Y., and D. J. Jacob (1998), Anthropogenic forcing on tropospheric ozone and OH since preindustrial times, *Journal of Geophysical Research: Atmospheres*, *103*(D23), 31123-31135.

Wang, Y., Y. Choi, T. Zeng, D. Davis, M. Buhr, L. G. Huey, and W. Neff (2007), Assessing the photochemical impact of snow NO_x emissions over Antarctica during ANTCI 2003, *Atmospheric Environment*, *41*(19), 3944-3958.

Wang, Y. H., S. C. Liu, H. B. Yu, S. T. Sandholm, T. Y. Chen, and D. R. Blake (2000), Influence of convection and biomass burning outflow on tropospheric chemistry over the tropical Pacific, *Journal of Geophysical Research-Atmospheres*, *105*(D7), 9321-9333.

Wang, Y. H., Y. S. Choi, T. Zeng, B. Ridley, N. Blake, D. Blake, and F. Flocke (2006), Late-spring increase of trans-Pacific pollution transport in the upper troposphere, *Geophysical Research Letters*, *33*(1).

Wang, Y. H., et al. (2001), Factors controlling tropospheric O_3, OH, NO_x and SO_2 over the tropical Pacific during PEM-Tropics B, *Journal of Geophysical Research-Atmospheres*, *106*(D23), 32733-32747.

Wang, Y. X., M. B. McElroy, R. V. Martin, D. G. Streets, Q. Zhang, and T. M. Fu (2007), Seasonal variability of NO_x emissions over east China constrained by satellite observations: Implications for combustion and microbial sources, *Journal of Geophysical Research-Atmospheres*, *112*(D6), 19.

Witte, J. C., M. R. Schoeberl, A. R. Douglass, J. F. Gleason, N. A. Krotkov, J. C. Gille, K. E. Pickering, and N. Livesey (2009), Satellite observations of changes in air

quality during the 2008 Beijing Olympics and Paralympics, *Geophysical Research Letters*, *36*.

Wu, Y., R. J. Wang, Y. Zhou, B. H. Lin, L. X. Fu, K. B. He, and J. M. Hao (2011), On-Road Vehicle Emission Control in Beijing: Past, Present, and Future, *Environ. Sci. Technol.*, *45*(1), 147-153.

Wu, Z. X., and T. A. Siddiqi (1995), THE ROLE OF NUCLEAR-ENERGY IN REDUCING THE ENVIRONMENTAL IMPACTS OF CHINA ENERGY USE, *Energy*, *20*(8), 777-783.

Xie, J. A. (2010), *Researches on Application Conditions of Grads Theory and Industrial Transfer in the Eastern Developed Provinces*, 303-310 pp., M D Forum, Allawah Nsw.

Yang, Q., Y. Wang, C. Zhao, Z. Liu, W. I. Gustafson, and M. Shao (2011), NO_x Emission Reduction and its Effects on Ozone during the 2008 Olympic Games, *Environ. Sci. Technol.*, *45*(15), 6404-6410.

Yang, W. J., Z. J. Zhou, J. H. Zhou, L. V. Hongkun, J. Z. Liu, and K. F. Cen (2009), Application of Hybrid Coal Reburning/SNCR Processes for NO_x Reduction in a Coal-Fired Boiler, *Environ. Eng. Sci.*, *26*(2), 311-317.

Yang, Y. Q., and H. S. Yu (2010), *The Empirical Study on the Environmental Impact of Two Typical Trade Growth Pattern: Comparison Based on 1992-2008 Emissions Data of Zhejiang and Guangdong Provinces*, 849-856 pp., Aussino Acad Publ House, Marrickville.

Yassaa, N., I. Peeken, E. Zollner, K. Bluhm, S. Arnold, D. Spracklen, and J. Williams (2008), Evidence for marine production of monoterpenes, *Environ. Chem.*, *5*(6), 391-401.

Yu, X., and H. Qu (2013), The role of China's renewable powers against climate change during the 12th Five-Year and until 2020, *Renewable and Sustainable Energy Reviews*, *22*(0), 401-409.

Zeng, T., Y. H. Wang, K. Chance, E. V. Browell, B. A. Ridley, and E. L. Atlas (2003), Widespread persistent near-surface ozone depletion at northern high latitudes in spring, *Geophysical Research Letters*, *30*(24), 2298, 10.1029/2003GL018587.

Zeng, T., Y. Wang, K. Chance, N. Blake, D. Blake, and B. Ridley (2006), Halogen-driven low-altitude O_3 and hydrocarbon losses in spring at northern high latitudes, *Journal of Geophysical Research-Atmospheres*, *111*(D17), D17313, doi:10.1029/2005JD006706.

Zhang, L.-j. (2010), Energy Optimization of SCR Coal-Fired Power Plant, *SHANXI ENERGY AND CONSERVATION*, *3*, 3.

Zhang, Q., D. G. Streets, and K. B. He (2009a), Satellite observations of recent power plant construction in Inner Mongolia, China, *Geophysical Research Letters*, *36*, 5.

Zhang, Q., G. N. Geng, S. W. Wang, A. Richter, and K. B. He (2012), Satellite remote sensing of changes in NO_x emissions over China during 1996-2010, *Chin. Sci. Bull.*, *57*(22), 2857-2864.

Zhang, Q., et al. (2007), NO_x emission trends for China, 1995-2004: The view from the ground and the view from space, *Journal of Geophysical Research-Atmospheres*, *112*(D22), D22306, doi:10.1029/2007JD008684.

Zhang, Q., et al. (2009b), Asian emissions in 2006 for the NASA INTEX-B mission, *Atmospheric Chemistry and Physics*, *9*(14), 5131-5153.

Zhao, B., S. X. Wang, J. Y. Xu, K. Fu, Z. Klimont, J. M. Hao, K. B. He, J. Cofala, and M. Amann (2013), NO_x emissions in China: historical trends and future perspectives, *Atmos. Chem. Phys. Discuss.*, *13*(6), 16047-16112.

Zhao, C., and Y. Wang (2009), Assimilated inversion of NO_x emissions over east Asia using OMI NO_2 column measurements, *Geophysical Research Letters*, *36*(6), L06805, doi:10.1029/2008GL037123.

Zhao, C., Y. H. Wang, and T. Zeng (2009a), East China Plains: A "Basin" of Ozone Pollution, *Environ. Sci. Technol.*, *43*(6), 1911-1915.

Zhao, C., Y. Wang, Y. Choi, and T. Zeng (2009b), Summertime impact of convective transport and lightning NO_x production over North America: modeling dependence on meteorological simulations, *Atmos. Chem. Phys.*, *9*(13), 4315–4327.

Zhao, C., Y. Wang, Q. Yang, R. Fu, D. Cunnold, and Y. Choi (2010), Impact of East Asian summer monsoon on the air quality over China: View from space, *Journal of Geophysical Research: Atmospheres*, *115*(D9), D09301, doi:10.1029/2009JD012745.

Zhao, Y., J. Zhang, and C. P. Nielsen (2013), The effects of recent control policies on trends in emissions of anthropogenic atmospheric pollutants and CO_2 in China, *Atmospheric Chemistry and Physics*, *13*(2), 487-508.

Zheng, F. H., and S. C. Qin (2009), *Environmental Pollution, Environmental Performance of Government and Public Satisfaction: An Empirical Study on Guangdong Province in 2007*, 394-397 pp., Intellectual Property Publ House, Haidian District.

VITA

DASA GU

Dasa Gu was born in Nanjing, China. He received a B.S. in Chemistry from Nanjing University, Jiangsu, China in 2004 and a M.S. in Environmental Sciences from Peking University, Beijing, China in 2007 before coming to Georgia Tech to pursue a doctorate in Atmospheric Science. When he is not working on his research, Mr. Gu enjoys regular workouts and watching various sports.